

## Durham E-Theses

---

### *Electron spin resonance studies of doped alumina and aluminium nitride*

Mushait, Al-Naief

#### How to cite:

---

Mushait, Al-Naief (1988) *Electron spin resonance studies of doped alumina and aluminium nitride*, Durham theses, Durham University. Available at Durham E-Theses Online:  
<http://etheses.dur.ac.uk/6605/>

#### Use policy

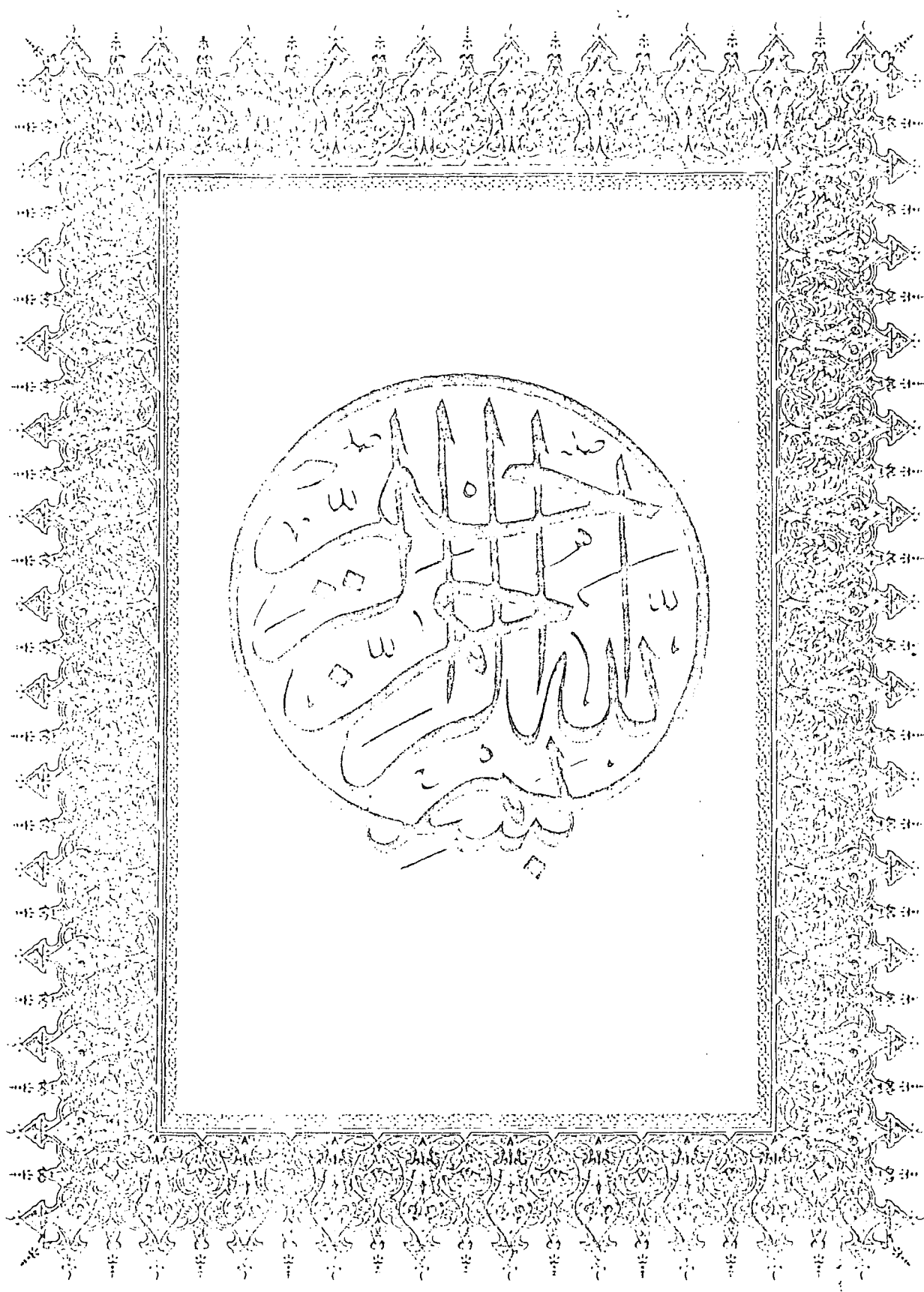
---

The full-text may be used and/or reproduced, and given to third parties in any format or medium, without prior permission or charge, for personal research or study, educational, or not-for-profit purposes provided that:

- a full bibliographic reference is made to the original source
- a [link](#) is made to the metadata record in Durham E-Theses
- the full-text is not changed in any way

The full-text must not be sold in any format or medium without the formal permission of the copyright holders.

Please consult the [full Durham E-Theses policy](#) for further details.



ELECTRON SPIN RESONANCE STUDIES

of

DOPED ALUMINA and ALUMINIUM NITRIDE

by

Al-Naief Mushait, B.Sc. (King Saud University)

M.Sc. (Idaho State University)

Graduate Society

A thesis submitted to the University of Durham

in candidature of the degree of

Doctor of Philosophy

April, 1988

The copyright of this thesis rests with the author.  
No quotation from it should be published without  
his prior written consent and information derived  
from it should be acknowledged.



19 SEP 1988

## CONTENTS

PAGE

ACKNOWLEDGEMENTS	i
ABSTRACT	ii
CHAPTER ONE : Introduction	1
References	6

### PART I

## Electron Paramagnetic Resonance Studies of Doped Alumina

CHAPTER TWO : The interpretation of E.P.R. spectral linewidth and linshape	8
2.1 Introduction.	8
2.2 The determination of the lineshape and linewidth - a review	10
2.3 Spin-Spin Interaction.	14
2.3.1 Van Vleck's theory.	16
2.3.2 Kittel and Abrahams' extension.	22

2.3.3 de Biasi and Fernandes' model.	25
References	30
CHAPTER THREE: E.P.R. Studies of Gadolinium Doped Alumina	32
3.1 Introduction.	32
3.2 Experimental results.	34
3.3 Theoretical linewidths.	36
3.3.1 Introduction.	36
3.3.2 Results I: The Van Vleck model.	36
3.3.3 Results II: Kittel and Abrahams' model.	36
3.4 Discussion.	42
References	44
CHAPTER FOUR: E.P.R. Investigations of Chromium Doped Aluminium	46
Oxide Single Crystals and Powders	46

4.1 Introduction.	46
4.2 Single crystals experimental results.	48
4.3 Theoretical calculation for single crystal linewidth.	50
4.3.1 Van Vleck (dipolar broadening theory).	50
4.3.2 Kittel and Abrahams' model.	51
4.3.3 de Biasi and Fernandes' model.	52
4.4 Discussion of the single crystal results.	53
4.5 Characterisation of the E.P.R. spectra of the chromium doped alumina powdered samples.	54
4.6 Computer simulations of powder spectra.	55
4.7 Theory and discussion of the powder linewidth.	58
4.7.1 Van Vleck Linewidth.	58
4.7.2 Kittel and Abrahams' linewidth.	58

4.7.3 de Biasi and Fernandes' model. 59

References 61

## CHAPTER FIVE: E.P.R. Studies of Iron Doped Aluminium Oxide Single Crystal

and Powder 63

5.1 Introduction 63

5.2 Experimental results. 64

5.3 Theoretical calculation for iron doped alumina single crystal. 65

5.3.1 Van Vleck's dipole theory. 65

5.3.2 Kittel and Abrahams' model. 66

5.4 Discussion of single crystal results. 67

5.5 Characterisation of E.P.R. spectrum of iron doped alumina  
powder sample. 68

References 71

## PART II

### Electron Spin Resonance and Related Studies

on

### Aluminium Nitride

CHAPTER SIX: Experimental Techniques	73
6.1 X-ray techniques.	73
6.2 S.E.M. and E.D.A.X. techniques.	74
6.3 Electron Spin Resonance.	74
6.4 Gouy Balance technique.	76
6.5 Dielectric measurement techniques.	77
6.6 The samples examined.	80
References	82
CHAPTER SEVEN: Experimental Results	83
7.1 Structural characterisation.	83
7.1.1 Diffraction, X-ray fluorescent analysis and E.D.A.X.	83

7.1.2 Electron Spin Resonance results.	85
7.1.3 Curie temperature determination.	86
7.2 Dielectric properties.	87
References	88
CHAPTER EIGHT: Discussion and Conclusions	89
8.1 Features revealed by X-ray and E.D.A.X. studies.	89
8.2 Features revealed by magnetic measurements.	90
8.3 Features revealed by dielectric measurements.	93
References	96

## ACKNOWLEDGEMENTS

I would like to extend my grateful thanks to the following:

... Professor P.Mars and Professor J.Woods for the use of the facilities of the School of Engineering and Applied Science.

... the Applied Physics and Electronics Subject Group of S.E.A.S. at the University of Durham and all the other members of the Group.

...the King Saud University for their financial support.

...all my friends, who, in various ways, have contributed to the success of this thesis, and with them, Mrs.Ann Turnbull for typing this thesis.

I would especially like to express my gratitude to my Supervisor, Dr. J.S. Thorp for his enthusiastic guidance, advice and every possible help throughout the work and the preparation of this thesis, he has made this very pleasant. To him, I owe special thanks and outstanding appreciation.

Finally,much appreciation is due to my mother, brothers, sisters, Homode, Abraham, Rana, Nada, Ream and Homode's mother.

## ABSTRACT

In the first part of this thesis, Electron Paramagnetic Resonance (E.P.R.) techniques have been used to study the behaviour of gadolinium, chromium and iron in aluminium oxide single crystals and powders. E.P.R. single crystal spectra were recorded at room temperature for all three systems (with the dopant at various concentrations for the chromium case). The linewidth data extracted from these spectra of the single crystals showed good agreement with previously published results. The single crystal Spin-Hamiltonian parameters were used in computer simulations developed to predict the powder spectra for the chromium/aluminium oxide and iron/aluminium oxide systems and this allowed a comparison with the corresponding experimentally observed powder spectra due to  $Cr^{3+}$  and  $Fe^{3+}$  to be made. The experimental linewidths have been interpreted in terms of dipolar and exchange broadening theories in order to show which mechanisms apply to different dopants. In all the three systems, the main effect is dipolar broadening and exchange interactions are very small at the dopant concentration levels examined. For both forms of specimen (i.e. single crystal or powder) the Kittel-Abrahams' theory gave the best agreement with experiment.

The second part of the thesis was concerned with the elucidation of the structural and electrical nature of aluminium nitride using Electron Spin Resonance at

room and low temperatures with related techniques including dielectric measurements. The results have been reported and discussed. It is shown that for the purer grade aluminium nitride both the permittivity and the dielectric loss are very nearly independent of frequency suggesting that the material behaves as a hopping conductor with electrical properties very similar to those of aluminium oxide, which is widely accepted as a useful substrate material in very large scale integration high performance packaging. In the less pure forms of aluminium nitride the major impurity was identified as iron whose presence was shown to be consistent with the higher values of permittivity observed.

Finally, as part of a general survey of the dielectric behaviour of oxide and nitrogen ceramics, a comparison was drawn between the aluminium oxide-aluminium nitride ceramic systems.

## CHAPTER ONE

### INTRODUCTION

The first part of this thesis describes EPR measurements on three types of doped alumina, namely gadolinium doped aluminium oxide,  $Gd^{3+}/Al_2O_3$ , chromium doped aluminium oxide,  $Cr^{3+}/Al_2O_3$  and iron doped aluminium oxide,  $Fe^{3+}/Al_2O_3$ . Aluminium oxide is an important material with many applications. For example, it is a very good dielectric and this property enables it to be widely used as an insulator in electronics. It is also, as is well known, a useful host lattice in the production of single crystal laser materials, of which the best known is perhaps ruby,  $Cr^{3+}/Al_2O_3$ .

Because of these uses, alumina, or rather various doped aluminas, have been fairly extensively examined in the past. Here the concern has been with the nature of the magnetic interactions between dopant atoms in magnetically dilute alumina systems, an area which is suitable for examination by EPR methods.

Consequently a major theme in the present work is to compare experimental and theoretical data which involved calculating the resonance linewidth in detail. This work can be discussed, somewhat arbitrarily, in four steps.

- 1) The single crystal spectra of gadolinium doped aluminium oxide,  $Gd^{3+}/Al_2O_3$ , chromium doped aluminium oxide,  $Cr^{3+}/Al_2O_3$  and iron doped aluminium oxide,



$Fe^{3+}/Al_2O_3$  have been obtained and their linewidths have been measured.

- 2) Three different theoretical models, Van Vleck's dipolar theory [1.1], Kittel and Abrahams' model [1.2] and de Biasi and Fernandes theory [1.3] have been applied to calculate the linewidth for comparison with our single crystal experimental data.
- 3) The experimental characterization of the powder spectra of  $Cr^{3+}/Al_2O_3$  and  $Fe^{3+}/Al_2O_3$  and their linewidths has been completed and the theoretical linewidths for  $Cr^{3+}$  and  $Fe^{3+}$  in the  $Al_2O_3$  lattice have been calculated using the three models previously mentioned.
- 4) The Spin Hamiltonians have been solved for  $Cr^{3+}/Al_2O_3$  and  $Fe^{3+}/Al_2O_3$  single crystals and computer programmes have been developed to produce the E.P.R. powder spectra simulations, the results of which have been recorded and compared with the experimental powder spectra.

The application of Kittel and Abrahams' model and the writing of the computer programmes for powder simulations have led to lengthy analytical procedures.

Chapter 2 discusses in general terms the theory and interpretation of E.P.R. spectra, linewidths and lineshapes and outlines the currently accepted models. Each of the following three Chapters is devoted to a particular material. Thus Chapter 3 considers gadolinium doped aluminium oxide. Here the experimental and theoretic-

cal results are dealt with in the single crystal only, because supplies of this rather unique material were limited. The theoretical part includes Van Vleck's dipolar theory and Kittel and Abrahams' model, both of which are applicable to single crystals. Chapter 4 covers the experimental results and their theoretical interpretation for  $Cr^{3+}/Al_2O_3$  in both forms of single crystal and powder for different ranges of concentration and includes the results of the powder simulation. Chapter 5 reports the experimental results of  $Fe^{3+}/Al_2O_3$  of both single crystal and powder forms and their theoretical interpretation, together with the representation of the powder simulation.

The respective results are discussed and interpreted in the later sections of each Chapter. Taken as a whole, the work described in Part I extends and complements previous studies made by Kirkby [1.4] and by Buckley [1.5] on neodymium and gadolinium doped calcium tungstate; by Inglis [1.6] on iron doped magnesium oxide single crystals; by Skinner [1.7] on both single crystal and powder magnesium oxide doped with chromium or manganese and most recently by Williams [1.8] on magnesian-iron ferrites and fine superparamagnetic precipitates. Most of the earlier work had been concerned with single crystal data and theory. One of the principal aims of the electron paramagnetic resonance studies undertaken here was to broaden the base for the use and interpretation of E.P.R spectra obtained from powders. At the present stage of technological advances this is of particular importance since

many of the materials arousing exceptional interest, e.g. the new classes of high transition temperature oxide superconductors (Bednorz and Muller [1.9] and Finnemore [1.10] are being made as powders and used in sintered polycrystalline form rather than as single crystals.

The second part of the Thesis refers to Aluminium Nitride (AlN). This work relates to the need to provide insulating substrates for high performance Very Large Scale Integration (VLSI) packaging. At present the most widely used materials are alumina ( $Al_2O_3$ , both single crystal and polycrystalline) and cordierite glass ceramics, (crystallised  $MgO - Al_2O_3, -SiO_2$ ). While these materials have very good electrical and dielectric properties, their suitability for high power devices is limited because they both have low values of thermal conductivity. On the other hand aluminium nitride is known to have a high thermal conductivity (up to one hundred times that of aluminium oxide) and it is thought to have adequate dielectric properties. However, it is a relatively new material. Its fabrication methods have not yet been finalised (for example, there is at present no manufacturer of AlN in this country) and the properties of the available commercial material have not yet been well established. For these reasons a study of four types of AlN has been made with the aim of establishing the extent to which either inherent impurities or defects introduced during manufacture affect the dielectric behaviour of the resulting material. This study involved some E.S.R. appraisal but also several other complementary

techniques.

Chapter 6 outlines the experimental methods which comprised X-ray techniques, Scanning Electron Microscope (S.E.M.) and Energy Dispersive Analysis by X-ray (E.D.A.X.), Electron Spin Resonance (E.S.R.), the Gouy balance technique for Curie temperature and susceptibility measurements and dielectric measurements techniques. Chapter 7 lists the experimental results obtained under each heading and discusses the main features of each separately. In the final Chapter, (Chapter 8), all the results of Part II are discussed collectively and conclusions drawn regarding the potential of aluminium nitride as a substrate material. Some comments are also made on the more general question of the comparison of the permittivities of the oxides and nitrides of aluminium (studied here), silicon and magnesium all of which are also of interest in relation to their potential applications as refractory insulators.

## REFERENCES

- 1.1 J.H. Van Vleck, *Phys. Rev.* 74, 1168 (1948).
- 1.2 C.Kittel and E. Abrahams, *Phys. Rev.* 90, 238 (1953)
- 1.3 R.S. de Biasi and A.A.R. Fernandes, *J. Phys. C*.16, 548 (1983).
- 1.4 C.J. Kirkby, "*E.P.R. Line Shape in Maser Materials*". Ph.D. thesis, Durham University (1967).
- 1.5 H.P. Buckley, "*Properties of Impurity Ions in Some Single Crystals*". Pd.D. thesis, Durham University (1973).
- 1.6 A.D. Inglis, "*Clustering in Iron-doped Magnesium Oxide*". Ph.D. thesis, Durham University (1981).
- 1.7 A.R. Skinner, "*Electron Paramagnetic Resonance of Some 3d Ions in Magnesium Oxide*". Ph.D. thesis, Durham University (1986).
- 1.8 C.D. Williams, "*Some Magnetic Effects of Clustering in Iron Doped Magnesium Oxide*", Ph.D. thesis, Durham University (1987).
- 1.9 J.G. Bednorz and K.A. Muller, *Z. Phys*, B64, 189, (1986).

1.10 D.K. Finnemore, R.N. Shelton, J.R. Etem, R.W. McCallum, H.C. Ku, R.E. McCarley, S.C. Chen, P. Klavins and V. Kogan, *Phys. Rev.* B35, 5319 (1987).

PART I

Electron Paramagnetic Resonance Studies

on

Doped Alumina

## CHAPTER TWO

# THE INTERPRETATION OF E.P.R. SPECTRAL LINEWIDTH AND LINESHAPE

### 2.1 Introduction

There are two important broadening mechanisms influencing the E.P.R. linewidth and lineshape. The first is the homogeneous mechanism, for example dipolar interaction, exchange interaction, and the spin-lattice relaxation. The second is any inhomogeneous mechanism such as the axial misorientation and strain at paramagnetic sites. The homogeneous broadening mechanism extends the response of every individual spin and broadens the response of the system as a whole by increasing the coupling between different spins. Each individual spin in a magnetic system is subjected not only to any externally applied magnetic field, but also to the local fields of neighbouring magnetic dipoles. The necessity of magnetic dilution to reduce spin-spin effects can be readily appreciated, as the resultant field at the site of any spin is the sum of the effects of its neighbours.

With exchange interaction, paramagnetic spins may in some cases be located relative to one another so that powerful short-range exchange forces become effective. The interaction may be written in the form  $J(S_1, S_2)$ , and is said to be isotropic if its

value depends solely on the scalar product, and hence on the relative orientation of  $S_1$  and  $S_2$ . In practice only  $s$ -orbitals exhibit isotropic charge densities and consequently anisotropic exchange might generally be expected. Depending on the relative strength of the dipolar interaction, exchange may influence the shape of E.P.R. absorptions.

When we come to spin-lattice relaxation the uncertainty principle predicts that there must be an uncertainty in its energy, if the lifetime of a quantum state is finite and known. The lifetime  $T_1$  of a spin in an excited quantum state is the spin-lattice relaxation time, and the lower limit of linewidth is governed by the equation (2.1) Poole and Farach [2.1].

$$\Delta f > \frac{1}{T_1} \tag{2.1}$$

where  $f$  is the width of the line in frequency units. In many laser materials, the relaxation time is sufficiently long for this mechanism to be relatively negligible, Buckley, Thorp and Kirkby [2.2, 2.3, 2.4] We will be discussing in this Chapter the nature of homogeneous broadening mechanisms especially dipolar and exchange interaction (spin-spin interaction) and giving experimental evidence which suggests that the dipolar mechanism largely determines the linewidths and lineshape of E.P.R. spectra of  $Gd^{+3}$ ,  $Cr^{+3}$  and  $Fe^{+3}$  in  $Al_2O_3$ . The experimental characteristics of E.P.R.

lineshape and linewidth and their dependence on the doping concentration are large compared with the theoretical broadening due to the spin-lattice relaxation which is negligible in the present context. Other sources of E.P.R. broadening, such as interaction between ions and nuclei of surrounding diamagnetic ions, and inhomogeneous effects are not as important as the homogeneous mechanism; therefore, these effects are not discussed. Details of mechanisms which give rise to these sources of broadening and the effects that they have upon linewidth and lineshape are given in the standard text Abraham, Poole and Wertz [2.5, 2.6, 2.7].

## 2.2 The Determination of Lineshape and Linewidth - A Review

It is usual to consider the moments of the line, particularly the second and the fourth moment and describe the shape of an individual resonance peak in terms of them. The  $n$ th moment of a line can be written as (Al'tshuler and Kozyrev) [2.8].

$$M_n = \int_0^\infty f(\nu - \nu_0) f(\nu) d\nu \quad 2.2$$

where  $\nu_0$  is the frequency at the point of maximum absorption of the resonance line and  $f(\nu)$  is the lineshape function which is normalised so that

$$\int_0^{\infty} f(\nu) d\nu = 1 \quad 2.3$$

We can define  $M_n$  as

$$M_n = \int_{-\nu_0}^{\infty} u^n f(u) du \quad 2.4$$

Where  $u = \nu - \nu_0$  and

$$f(\nu) = f(\nu_0 + u) = f(u) \quad 2.5$$

and for narrow lines this becomes

$$M_n = \int_{-\infty}^{\infty} u^n f(u) du \quad 2.6$$

The odd moments vanish for all the symmetric lines. There are two alternative line functions which are usually used to describe the experimental lineshape; these are the Lorentzian and Gaussian approximations.

The Lorentzian curve is given by

$$f(u) = \frac{\Delta}{2\pi} \left( \frac{1}{u^2 + \frac{\Delta^2}{4}} \right) \quad 2.7a$$

While the Gaussian curve is

$$f(u) = \frac{1}{\sigma\sqrt{2\pi}} e^{-u^2/2\sigma^2} \quad 2.7b$$

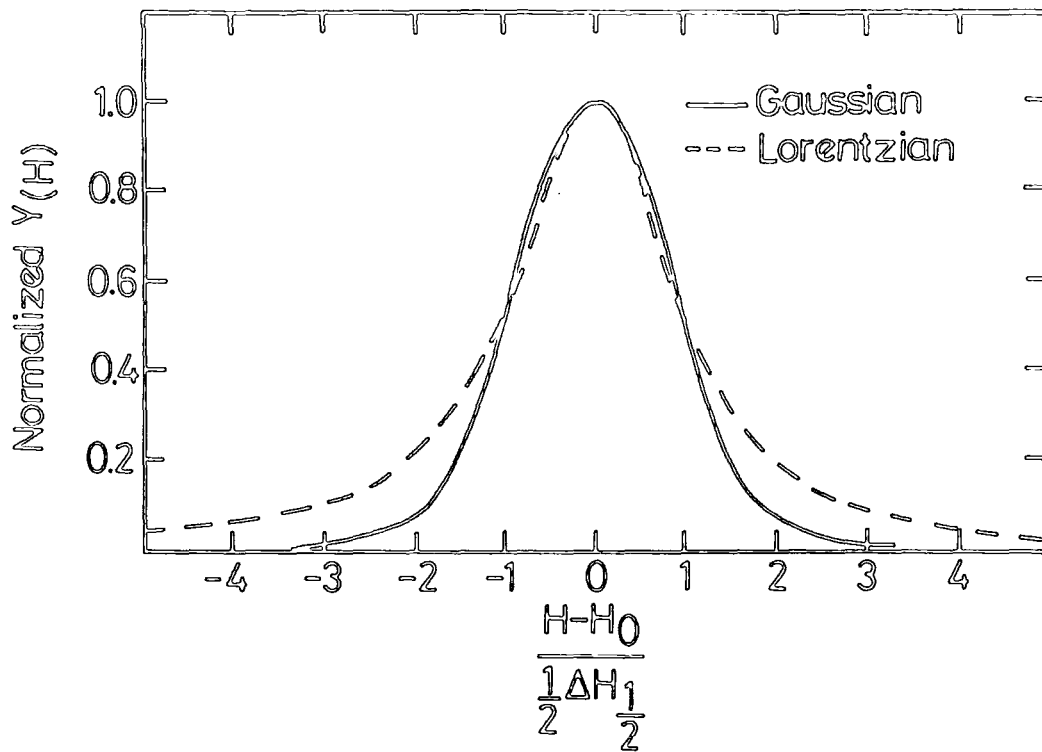
These two lineshapes are shown in Fig (2.1) and  $\sigma$  and  $\Delta$  are defined below. The linewidth  $\Delta\nu$  is calculated according to the equation

$$f\left(u = \frac{\Delta\nu}{2}\right) = \frac{1}{2}f(0) \quad 2.8$$

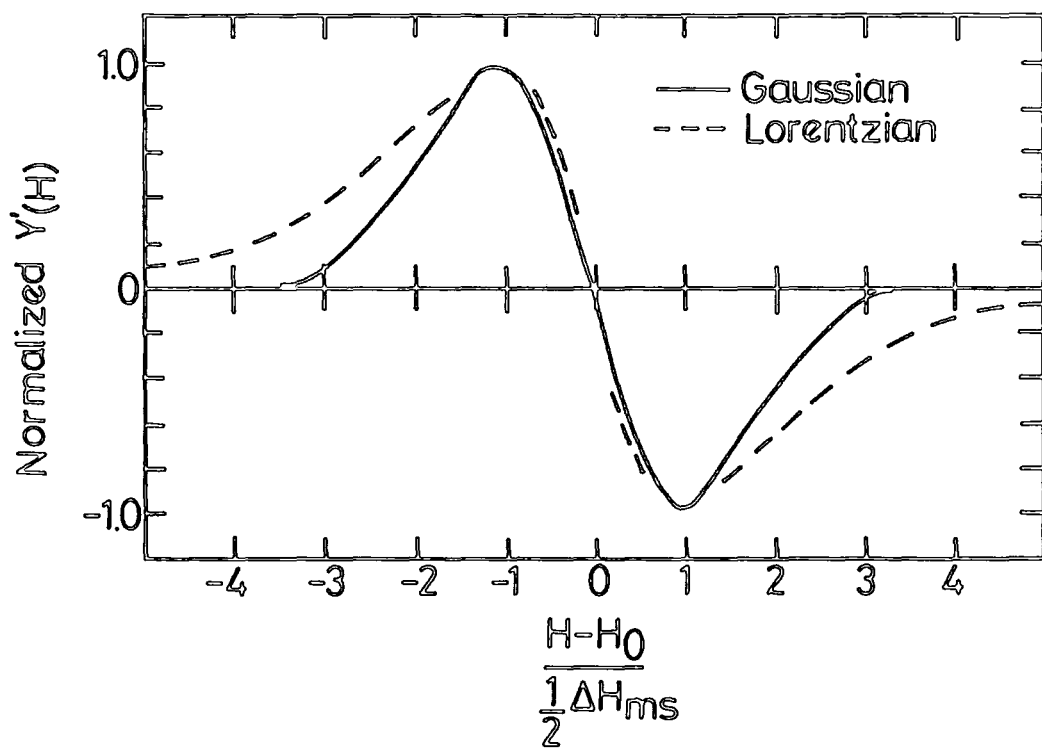
and is given by

$$\begin{aligned} \Delta\nu &= 2\sigma\sqrt{2\ln 2} \\ &= 2.35\sigma \end{aligned} \quad 2.9$$

for Gaussian lineshape and



(a)



(b)

Fig. (2.1) a) Lorentzian and Gaussian absorption curves with the same half amplitude linewidth  
 b) Lorentzian and Gaussian absorption first derivative curves with the same peak-to-peak linewidth

$$\Delta\nu = \Delta \quad 2.10$$

for Lorentzian lineshape. For Gaussian lineshapes the even moments are

$$\begin{aligned} M_2 &= \sigma^2 \\ M_4 &= 3\sigma^4 \\ M_{2n} &= 1, 3, 5 \dots (2n-1)\sigma^{2n} \end{aligned} \quad 2.11$$

For a Lorentzian Curve the cut-off frequency is

$$\nu_c = \alpha$$

and

$$\alpha \gg \nu_0$$

and the even moments are

$$\begin{aligned} M_2 &= \frac{\alpha\Delta}{\pi} \\ M_4 &= \frac{\alpha^3\Delta}{3\pi} \\ M_n &= \frac{\Delta}{\pi} \cdot \frac{\alpha^{n-1}}{n-1} \end{aligned} \quad 2.12$$

The Gaussian and Lorentzian curves are symmetrical with respect to  $\nu_0$ , therefore the odd moments vanish. To examine the similarity between a given shape function and the Gaussian or Lorentzian Curve, we calculate the ratio  $M_4/M_2^2$ . In doing this we may note that for the Gaussian curve

$$M_4/M_2^2 = 3 \tag{2.13}$$

and for the Lorentzian Curve

$$M_4/M_2^2 = \frac{\alpha\pi}{3\Delta} \gg 1 \tag{2.14}$$

### 2.3 Spin-Spin Interaction

The interactions between neighbouring paramagnetic ions are known as Spin-Spin interactions and these are responsible for both dipolar and exchange effects; Anderson and Scientific staff [2.9, 2.10]. The dipolar interaction leads to a broadening of the resonance line, whereas the exchange interactions narrow the line. Dipolar broadening arises from the fact that each paramagnetic particle is subjected to the action of external magnetic fields. With  $H_0 = H + H_{loc}$  the resonance conditions will be fulfilled for different values of  $H_0$  depending on  $H_{loc}$ . The order of magnitude

of  $H_{loc} = \beta/r^3$  where  $r$  is the separation of the particle, so

$$\Delta\nu \sim \beta^2/hr^3$$

The spins may be coupled together by both dipolar and exchange interactions. In such systems, the second moment is unaltered by the present exchange, being dependent upon dipolar interactions alone, but because of the exchange terms in the fourth moment equation the fourth moment becomes larger than it would be in the absence of exchange. Thus, if both spin-spin interactions are important in a material, the ratio  $M_4/M_2^2$  is larger than it is in materials where the spin-spin interactions are purely dipolar in origin. From equations (2.13) and (2.14) we may conclude that exchange forces alter the dipolar lineshape in such a way that as they increase in strength the lineshape moves away from Gaussian towards Lorentzian i.e. the resonance peak is sharpened, the line becoming narrower at the centre and dropping off more rapidly in the wings as shown in Fig. (2.2). The second moment may no longer be used to calculate the linewidth in the manner described when the broadening is due to dipolar interactions alone since such a calculation assumes that the lineshape is Gaussian. However, Anderson and Weiss [2.11] showed that if both exchange and dipolar forces are important, the half width,  $\Delta\nu$ , is given by

$$\Delta\nu = \frac{M_2}{(J^W/h)} \tag{2.15}$$

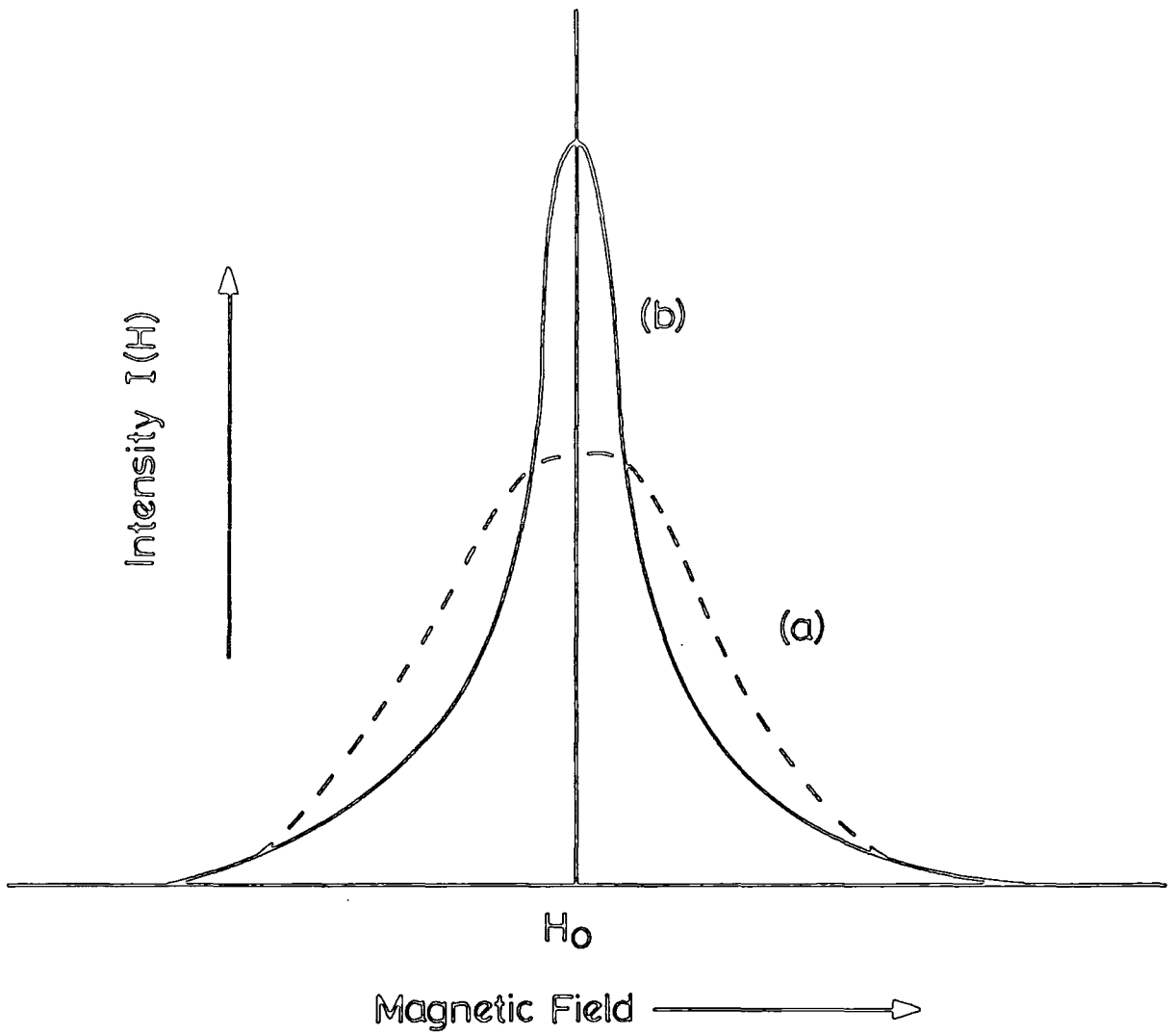


Fig. (2.2) Absorption Lineshape a) Without  
b) With exchange interaction (Van Vleck [2.13]).

where  $M_2$  is the second moment due to dipolar broadening, and  $(J^{\text{ex}}/h)$  is the exchange energy in frequency units. The overall effect of exchange forces, therefore, is to reduce the linewidth. In systems where the spin-spin interactions are purely dipolar in nature, the exchange terms in the fourth moment equation disappear and evaluation of the ratio  $M_4/M_2^2$  shows that the lineshape is Gaussian. The value of the second moment may be used to calculate a theoretical value for the linewidth,  $\Delta\nu$ , since equations (2.8) and (2.11) show that for a Gaussian line

$$\Delta\nu = 2.35\sqrt{M_2}$$

### 2.3.1 Van Vleck's theory

The first rigorous mathematical description of dipolar broadening was given by Van Vleck [2.12], who derived expressions for the second and fourth moments of absorption lines under certain limitations. Van Vleck concluded that the discrepancies between theory and experiment could be explained by assuming that considerable exchange interactions occurred. It must be remembered that his model only applied to materials such as those listed in Table (2.1), in which the linewidths calculated using the dipolar broadening theory were much larger than those observed. Van Vleck considered the dipole-dipole interaction in a crystal with one type of paramagnetic centre. He used a Hamiltonian of the form

Substance	experimental linewidth, Gauss	Calculated linewidth, Gauss	$M_4/M_2^2$
<i>MnCl<sub>2</sub>4H<sub>2</sub>O</i>	1.410	1.530	2.28
<i>MnCl<sub>2</sub></i>	750	2.950	3.84
<i>MnSO<sub>4</sub>4H<sub>2</sub>O</i>	1.150	1.560	2.69
<i>MnSO<sub>4</sub>H<sub>2</sub>O</i>	320	2.870	4.54
<i>MnSO<sub>4</sub></i>	665	3.520	3.33
<i>MnNO<sub>6</sub>H<sub>2</sub>O</i>	1.210	1.003	2.92
<i>MnF<sub>2</sub></i>	470	7.020	3.73

Table 2.1 : Some of Valu Vleck's dipolar line broadening data. [2.13]

$$\mathcal{H} = Hg\beta \sum S_{izj} + \sum_{k>j} A_{ik} S_j S_k + g^2 \beta^2 \sum_{k>j} [r_{jk}^{-3} (S_j \cdot S_k) - 3r_{jk}^{-5} (S_j \cdot r_{jk})(r_{jk} \cdot S_k)] \quad 2.16$$

where the first, second and third terms represent the Zeemann, exchange and dipolar energies respectively;  $A_j$  is related to the normal exchange integral by

$$A_{jk} = 2/J_{jk}$$

He found that only dipolar interaction contributes towards the second moment whereas the fourth moment equation contains terms due to both dipolar and the exchange interaction. He made the following assumptions in order to arrive at his formula:

- 1) The paramagnetic center is purely spin in nature so that both initial splittings and anisotropy of g-value are absent.
- 2) The Zeemann energy is larger than dipole-dipole interaction.
- 3) The temperature is high so that the population of the Zeemann levels can be regarded as identical.

Van Vleck's second moment theory concerns two different types of dipolar interac-

tion, firstly interaction between atoms having the same  $g$  factor and the same spin quantum number  $S$  and secondly the interaction between atoms of different  $g$  and  $S$ , where the resonances of the two atoms do not overlap. If we assume that the magnetic moment in all cases is characterized by  $g\sqrt{[S(S+1)]}$  where  $g = 2.0023$  we can write explicit equations for the second moments in the two cases. For like atoms

$$\langle \Delta\nu^2 \rangle = \frac{3}{4}S(S+1)\left(\frac{g^2\beta^2}{h}\right)^2 \sum_{jk} r^{-6}(3\cos^2\theta_{jk} - 1)^2 \quad 2.17$$

where  $\langle \Delta\nu^2 \rangle$  is the second moment of the line, being measured in radians per second;  $g$  is the  $g$  factor of the atom;  $\beta$  is the Bohr magneton;  $r_{jk}$  is the radius vector from the reference atom  $j$  to all the neighbouring atoms labelled over  $k$ ;  $\theta_{jk}$  is the angle between the radius vector and a crystallographic reference axis. For unlike atoms

$$\langle \Delta\nu^2 \rangle = \frac{1}{3}S(S+1)\left(\frac{gg^a\beta^2}{h}\right)^2 \sum_{jk} r^{-6}(3\cos^2\theta_{jk} - 1)^2 \quad 2.18$$

where  $g$  refers to the reference atom;  $g^a$  refers to the surrounding atoms. The numerical factor  $\frac{3}{4}$  in the equation for like atoms, and  $\frac{1}{3}$  in the equation for unlike atoms shows that like atoms produce a mean square broadening which is  $\frac{9}{4}$  times

greater than that produced by unlike atoms. The reason for this is that the resonances of like atoms do overlap and thus enhance the mutual coupling, Van Vleck and Bleaney [2.13, 2.14].

Equations (2.17) and (2.18) can each be split into two parts, the first relating only to the atomic parameters, the second describing the particular crystal system being investigated. Van Vleck evaluated the  $(3\cos^2\theta_{jk} - 1)^2$  term by using direction cosines but we shall use associated Legendre polynomials (spherical harmonics). In this way, we can write

$$\begin{aligned} (3\cos^2\theta - 1)^2 = \frac{4}{5} + \frac{32\pi}{21} \sum_m Y_{2,m}^*(\theta_H, \phi_H) \cdot Y_{2,m}(\theta_k, \phi_k) \\ + \frac{32\pi}{35} \cdot \sum_m Y_{4,m}^*(\theta_H, \phi_H) \cdot Y_{4,m}(\theta_k, \phi_k) \end{aligned} \quad 2.19$$

$\theta_H$  and  $\phi_H$  refer the static magnetic field to the crystal axes, while  $\theta_K$  and  $\phi_K$  refer the radius vector to the same axes. For a crystal with the trigonal symmetry, the only possible values of  $m$  are 0 and  $\pm 4$  [2.14]. Combining these with the standard equation

$$(-1)^m Y_{l,m}^* = Y_{l,-m} \quad 2.20$$

and substituting in equation (2.19) we have

$$\begin{aligned}
(3\cos^2\theta - 1)^2 &= \frac{4}{5} + \frac{32\pi}{21}[Y_{2,0}^*(\theta_H, \phi_H) \cdot Y_{2,0}(\theta_k, \phi_k)] \\
&+ [\frac{32\pi}{35}Y_{4,0}^*(\theta_H, \phi_H) \cdot Y_{4,0}(\theta_k, \phi_k)] \\
&+ [\frac{64\pi}{35}Y_{4,3}^*(\theta_H, \phi_H) \cdot Y_{4,-3}(\theta_k, \phi_k)] \qquad 2.21
\end{aligned}$$

Thus in order to evaluate the basic term  $(r^{-6})(3\cos^2\theta - 1)^2$  we need to index all the active sites within a given radius of our reference site, and calculate  $r, \theta, \phi$  for each one before performing the summations required. Our final equations become

a) for like atoms

$$\begin{aligned}
\langle \Delta\nu^2 \rangle &= \frac{3}{4}S(S+1)\left(\frac{g^2\beta^2}{\hbar}\right)^2 \frac{4}{5} \sum_k r_{jk}^{-6} \\
&+ \frac{32\pi}{21}[Y_{2,0}^*(\theta_H, \phi_H) \sum_k r_{jk}^{-6} Y_{2,0}(\theta_k, \phi_k)] \\
&+ \frac{32\pi}{21}[Y_{4,0}^*(\theta_H, \phi_H) \sum_k r_{jk}^{-6} Y_{4,0}(\theta_k, \phi_k)] \\
&+ \frac{64\pi}{35}[Y_{4,3}^*(\theta_H, \phi_H) \sum_k r_{jk}^{-6} Y_{4,-3}(\theta_k, \phi_k)] \qquad 2.22
\end{aligned}$$

b) for unlike atoms

$$\begin{aligned}
\langle \Delta\nu^2 \rangle = & \frac{1}{3}S(S+1)\left(\frac{gg^{\lambda}\beta^2}{\hbar}\right)^2 \cdot \frac{4}{5} \sum_k r_{jk}^{-6} \\
& + \frac{32\pi}{21} Y_{2,0}^*(\theta_H, \phi_H) \sum_k r_{jk}^{-6} Y_{2,0}(\theta_k, \phi_k) \\
& + \frac{32\pi}{21} [Y_{4,0}^*(\theta_H, \phi_H) \sum_k \tilde{r}_{jk}^{-6} Y_{4,0}(\theta_k, \phi_k)] \\
& + \frac{64\pi}{35} [Y_{4,3}^*(\theta_H, \phi_H) \sum_k \tilde{r}_{jk}^{-6} Y_{4,-3}(\theta_k, \phi_k)] \quad 2.23
\end{aligned}$$

The standard forms of the spherical harmonics are well known, Mallis [2.15] and are specified completely by  $\theta$  and  $\phi$ . The mean square width of the line, as given by equations (2.32) and 2.33) must be converted into the derivative peak-to-peak width, for comparison with experimental results. The peak-to-peak linewidth  $\Delta H_{ms}$  in Hertz is given by

$$\Delta H_{ms} = \frac{\sqrt{\langle \Delta\nu^2 \rangle}}{\pi} \text{ Hz} \quad 2.24$$

To convert this frequency width into a magnetic field width the  $\partial\nu/\partial H$  parameter must be calculated from the experimental evaluation of  $g$  as a function of polar angle. Then

$$\Delta H_{ms} = \frac{\sqrt{\langle \Delta\nu^2 \rangle}}{\pi} \frac{\partial H}{\partial \nu} \text{ tesla} \quad 2.25$$

We shall concentrate first upon the crystal system and, having extracted  $r, \theta, \phi$  for substitution in the preceding equations, we shall then consider the specific values of  $S$  and  $g$  to be used for the particular dipolar interactions, Grant and Strandberg [2.16].

### 2.3.2 Kittel and Abrahams' Extension [2.17]

Kittel and Abrahams extended the theory of Van Vleck to cover a magnetically dilute system, and by assuming the absence of exchange, showed that a paramagnetic concentration below 0.01% the dipolar line would be Lorentzian in shape, having a width proportional to the paramagnetic concentration, whereas in the region above 0.1% the line would become Gaussian, with a width proportional to the square root of the concentration. If  $f$  is the probability that a lattice site is occupied by a magnetic system, Kittel and Abrahams found that the second moment, in frequency units, is given by

$$\langle \Delta\nu^2 \rangle = \left[ \frac{S(S+1)}{3\hbar^2} \right] f \sum_k \beta_{jk}^2 \quad 2.26$$

with

$$\beta_{jk}^2 = \left(\frac{3}{2}g^2\beta^2r_{jk}^{-3}\right)^2[(1 - 3\cos^2\theta_{jk})]^2 \quad 2.27$$

and the fourth moment can be written in the form [2.8]

$$\begin{aligned} h^2 \langle \Delta\nu^2 \rangle = & f^2 \left[ 3\left(\sum_k \beta_{jk}^2\right)^2 - \frac{1}{3} \sum_{j=k=l} \beta_{jk}^2(\beta_{jl} - \beta_{kl}) \right. \\ & \left. + \dots + f\left(1.4 - \frac{0.3}{S(S+1)\sum_k \beta_{jk}^2}\right) \left[\frac{1}{3}S(S+1)\right]^2 \right] \quad 2.28 \end{aligned}$$

where  $r_{jk}$  is the distance between the  $j$ th and  $k$ th atom, and  $\theta_{jk}$  is the angle between  $r_{jk}$  and the applied magnetic field and the sum  $\sum_{jk}$  is taken over all occupied sites. Equation (2.28) is simply equivalent to  $M_2 f$  where  $M_2$  is the value of the second moment predicted by Van Vleck's dipolar broadening theory. If ( $f \ll 0.01$ ), the term proportional to  $f$  can be neglected, then:

$$\frac{\langle \Delta\nu^4 \rangle}{\langle \Delta\nu^2 \rangle} = \frac{1}{f} \frac{\sum_k \beta_{jk}^4}{(\sum_k \beta_{jk}^2)^2} \quad 2.29$$

If all the sites are occupied ( $f=1$ ), then equation (2.28) is equal to Van Vleck's equation (2.24). For the value of  $f \approx 0.1$ , the lineshape is approximately Gaussian. If  $f > 0.01$  the deviation from Gaussian shape becomes very marked and equation (2.29) can be compared with equation (2.13) and (2.14) which shows that the lineshape

may be described by a cut-off Lorentzian line. For the doped  $Al_2O_3$  sample examined in this work, equations (2.12) and (2.29) are applied and the second and fourth moments were derived. For the cut-off Lorentzian curve, we may find that

$$\begin{aligned}\Delta &= \frac{\pi}{\sqrt{3}} \frac{M_2^{3/2}}{M_4^{1/2}} \\ &= \frac{\pi}{3} f \frac{(\sum_k \beta_{jk}^2)^{3/2}}{\hbar(\sum_k \beta_{jk}^{1/2})} \left[ \frac{S(S+1)}{1.4 - \frac{0.3}{S(S+1)}} \right]^{-1/2}\end{aligned}\quad 2.30$$

where  $\sum_k \beta_{jk}^4$  includes a  $(3\cos^2\theta_{jk} - 1)^4$  term, which can be evaluated using Legendre polynomials (spherical harmonics). In this way, we can write

$$(3\cos^2\theta_{jk} - 1)^4 = \frac{48}{35} + \frac{320}{77}p_2(\cos\theta) + \frac{1296}{495}p_4(\cos\theta)\quad 2.31$$

Therefore Kittel and Abrahams model of a dipolar broadening in dilute magnetic materials predicts for a single crystal that the peak-to-peak linewidth  $\Delta H_{ms}$ , is given by

$$\begin{aligned}\Delta H_{ms} &= f \frac{\Delta}{\sqrt{3}} \\ &= \frac{\pi}{(3)^{3/2}} f \frac{(\sum_k \beta_{jk}^2)^{3/2}}{(\sum_k \beta_{jk}^4)^{1/2}} \left[ \frac{S(S+1)}{1.4 - \frac{0.3}{S(S+1)}} \right]^{-1/2}\end{aligned}\quad 2.32$$

For the powder form, we obtain

$$\Delta H_{ms} = 0.96f \frac{(\sum_k r_{jk}^{-6})^{3/2}}{(\sum_k r_{jk}^{-12})^{1/2}} \left( \frac{g^2 \beta^2}{\hbar} \right) \left[ \frac{S(S+1)}{1.4 - \frac{0.3}{S(S+1)}} \right]^{-1/2} \quad 2.33$$

taking into account that

$$(1 - 3\cos^2\theta)^2 = \frac{4}{5}$$

it is also found that

$$(1 - 3\cos^2\theta)^4 = \frac{48}{35}$$

### 2.3.3 de Biasi and Fernandes' model [2.18]

The de Biasi and Fernandes' model is an extension of the theory of Kittel and Abrahams, by including the effect of exchange interaction in their model. Their model for the concentration dependence of the linewidth in dilute solid solution indicates that the probability of several ions being coupled together by exchange forces is very low. The aim of de Biasi and Fernandes' approach is to quantify the number of exchange coupled pairs in a dilute solid solution and to exclude the ions \(\backslash\) cou-

pled together from the summate terms in the expressions for the dipolar linewidth cut-off field of the truncated Lorentzian lineshape.

de Biasi and Fernandes suggested that the linewidth can be written as

$$\Delta H_{ms} = \left(\frac{\pi}{2\sqrt{3}}\right)A(S)fS_1^{3/2}(\theta)S_2^{-1/2}(\theta) \quad 2.34$$

where  $f$  is the impurity concentration and  $S$  is the spin of the paramagnetic impurity and in this expression

$$A(S) = (\mu_0 g \beta / 4\pi a^3) \left[ \frac{S(S+1)}{1.4 + 0.3(S^2 + S)^{-1}} \right]^{\frac{1}{2}} \quad 2.35a$$

$$S_1(\theta) = a^6 \sum_{r_{jk} > r_c} r_{jk}^{-6} (1 - 3\cos^2\theta_{jk})^2 \quad 2.35b$$

$$S_2(\theta) = a^{12} \sum_{r_{jk} > r_c} r_{jk}^{-12} (1 - 3\cos^2\theta_{jk})^4 \quad 2.35c$$

$$f_c = f(1 - f)^{Z(r_c)} \quad 2.35d$$

where  $a$  is the nearest neighbour distance in the host lattice,  $r_{jk}$  is the distance between  $j$  and  $k$  lattice sites and  $\theta_{jk}$  is the angle between  $r_{jk}$  and the magnetic field direction;  $f_c$  is the concentration of substitutional ions not coupled by the exchange interaction,  $r_c$  is the effective range of the exchange interaction and  $Z(r_c)$  is the number of cationic sites included in a sphere of radius  $r_c$ . The cut-off field is given by

$$H_c = H_0 \pm 3B(S)(S_{2\theta}(\theta)/S_{1\theta}(\theta))^{1/2} \quad 2.36$$

where

$$B(S) = (\mu_0 g \beta / 4\pi a^3)[0.3 + 1.4S(S + 1)]^{1/2} \quad 2.37$$

and

$$H_0 = h\nu/g\beta \quad 2.38$$

$A(s)$  and  $B(s)$  are constants which depend upon the parameters characterizing the paramagnetic ion and the host lattice, i.e. for the powdered form, the direction cosines in equation (2.35b) and (2.35c) can be replaced by their average over a

sphere, when the peak-to-peak linewidth and the cut-off fields can then be given by

$$\Delta H_{ms} = C_1 A(S) \quad 2.39$$

and

$$H = H_c + C_2 B(S) \quad 2.40$$

where

$$C_1 = \frac{\pi}{\sqrt{\pi/15}} f_c [S_1(r_c)]^{3/2} [S_2(r_c)]^{-1/2} \quad 2.41a$$

$$C_2 = (3\sqrt{21/7}) [S_2(r_c)] / [S_1(r_c)]^{1/2} \quad 2.41b$$

$$S_1(r_c) = a^6 \sum_{r_{jk} > r_c} r_{jk}^{-6} \quad 2.41c$$

$$S_2(r_c) = a^{12} \sum_{r_{jk} > r_c} r_{jk}^{-12} \quad 2.41d$$

It should be noted here that  $C_1$  is a function of the total concentration of the paramagnetic ion, the range of the exchange and the lattice geometry. Furthermore,  $C_2$  depends only on the lattice geometry and the range of the exchange interaction. The values of both coefficients  $C_1$  and  $C_2$  are independent of the parameters of the paramagnetic ion and the host lattice. The sums  $\sum_{r_{jk} < r_c} r_{jk}^{-6}$  and  $\sum_{r_{jk} < r_c} r_{jk}^{-12}$  have been calculated for different values of  $r_c$  and the results are shown in Table (2.2), where  $n$  is the number of the order of each coordinate,  $r = r_{jk}/a$  is the radius of the corresponding sphere and  $N$  is the number of cationic sites on the surface of the  $n$ th coordination sphere. The values of  $C_1$  and  $C_2$  were subsequently calculated, with the aid of Table (2.2). Specific detailed calculations were made using Van Vleck's dipolar theory. Similar calculations were made using Kittel and Abrahams' theory. The results for both sets of calculation are to be found in subsequent Chapters. The most recent (de Biasi and Fernandes) theory has been examined for the  $Cr^{3+}/Al_2O_3$  system in two forms, i.e. for single crystal and powder, and its applicability is discussed in Chapter 4.

n	r	N	$Nr^{-6} \times 10^{46}$	$Nr^{-12} \times 10^{95}$	$S_1(r_e)$	$S_2(r_e)$
1	2.730	1	2.4150	58.350	28.315	802.27
2	2.809	3	6.1068	12.430	71.607	170.90
3	3.187	3	2.8634	27.32	33.575	375.633
4	3.504	1	3.2417	17.51	38.0115	240.75
5	4.77	1	0.0848	0.07110	0.9943	0.9775
6	4.76	6	0.515	0.440	6.0383	6.049

Table 2.2 : Calculated values of  $S_1(r_e)$  and  $S_2(r_e)$  or the  $Al_2O_3$  lattice.

## References

- 2.1 C.P. Poole and H.A. Farach "*Relaxation in Magnetic Resonance*" Academic press, N.Y (1971).
- 2.2 H.P. Buckley, "*Property of Impurity Ions in Some Single Crystals*". Thesis, Durham University (1973).
- 2.3 J.S. Thorp, Sampson, D.F., and J.H. Pace, *Brit. J. Appl. Phys.* 12.705 (1961).
- 2.4 C.J. Kirkby, "*E.S.R. Lineshapes in Maser Materials*". Thesis, Durham University (1967).
- 2.5 A. Abraham and B. Bleaney, "*Paramagnetic Resonance of Transition Ions*". Clarendon press, Oxford (1970)
- 2.6 C.P. Poole, "*A Comprehensive Treatise on Experimental Techniques*", John Wiley and Sons, New York, London, Sydney (1967)
- 2.7 J.E. Wertz and J.R. Bolton, "*Electron Spin Resonance*" - *Elementary Theory and Application*. New York, Chapman and Hall 1986.
- 2.8 S.A. Al'tshuler and B.M. Kozyrev, "*Electron Paramagnetic Resonance in Compounds of Transition Elements*". 2nd Ed , U.K. Distributors, J. Wiley and Sons, Chichester (1974)
- 2.9 P.W. Anderson, *Phys. Rev.* 79, 350 (1950).

- 2.10 "An Elementary Discussion of Theory and Experiments in Electron Paramagnetic Resonance" by Members of the Scientific Staff of Alpha Scientific Laboratories, Berkeley, California (196 )
- 2.11 P.W. Anderson and P.R. Weiss, *Rev. Modern Phys.* 25, 269(1953).
- 2.12 J.H. Van Vleck, *Phs. Rev.* 74, 1168 (1948).
- 2.13 J.H. Van Vleck, *Nuovo Cimenta Supp.* 6, 993 (1956).
- 2.14 B. Bleaney and K.W.H. Stevens, *Reports Progr. Phys.* 16, 108 (1963)
- 2.15 D.C. Mallis, "The Theory of Magnetism" Harper and Row, New rk, York(1963).
- 2.16 W.J.C. Grant and M.W.P. Strandberg, *Phys. Rev.* 135 A727 (1964)
- 2.17 C. Kittel and E. Abrahams, *Phys. Rev.* 90, 238 (1953).
- 2.18 R.S. de Biasi and A.A.R. Fernandes, *J. Phys. C.* 16, 5481 (1983).

## CHAPTER THREE

### E.P.R. STUDIES OF GADOLINIUM DOPED ALUMINA

#### 3.1 Introduction

Rare earth-doped scheelites have been extensively studied and there has been some investigation into the actual linewidths. An example of this is in a series of papers by Russian workers, Vinokurov and Stephanov [3.1] in which gadolinium has been used to dope a number of different scheelites. Gadolinium, in particular, is a monitor ion in connection with studies in nucleation and crystallization in glasses, Hunt and Taylor [3.2]. The trivalent gadolinium ion has seven unpaired electrons in the  $4f^7$  unfilled shell which make it half-filled and gives rise to a ground state  $4f^7, 8S_{7/2}$ . The spin Hamiltonian for  $Gd^{3+}$  in aluminium oxide has been written, Geschwind and Remeika [3.3]

$$\mathcal{H} = g\beta H.S + B_2^0 O_2^0 + B_4^0 O_4^0 + B_6^0 O_6^0 + B_4^3 O_4^3 + B_6^3 O_6^3 + B_6^6 O_6^6 \quad 3.1$$

The coefficients  $B_n^m$  are parameters determined by experiment and are related to the more well known D and E term of the Spin Hamiltonian. They are defined by the relations

$$b_2^0 = 3B_2^0 \quad b_4^6 = 60B_4^6 \quad b_6^6 = 1260B_6^6$$

$$b_4^3 = 3B_4^3 \quad b_6^3 = 36B_6^3 \quad b_6^6 = 1260B_6^6$$

For a polar angle of  $\theta = 0$ , we can determine  $b_2^0, b_4^0, b_6^0$ , with the relative signs as the following

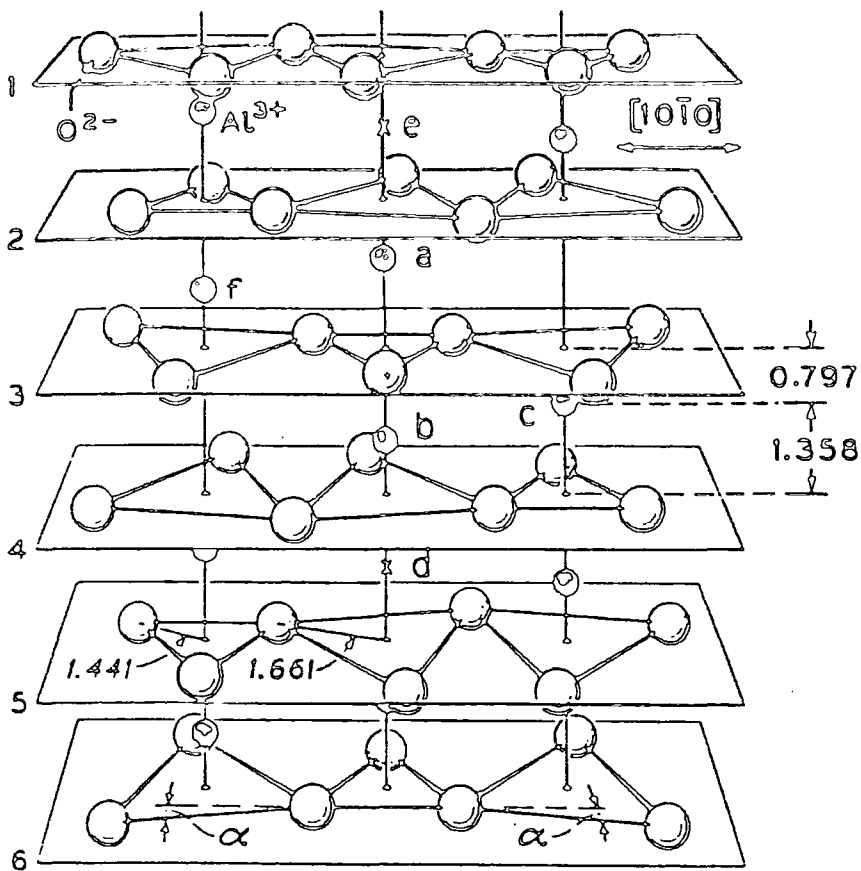
$$b_2^0 = 1032.9 \pm 2.0 \quad |b_4^3| = 18.3 \pm 1.0$$

$$b_4^0 = 26 \pm 0.5 \quad |b_6^6| = 5.0 \pm 0.5$$

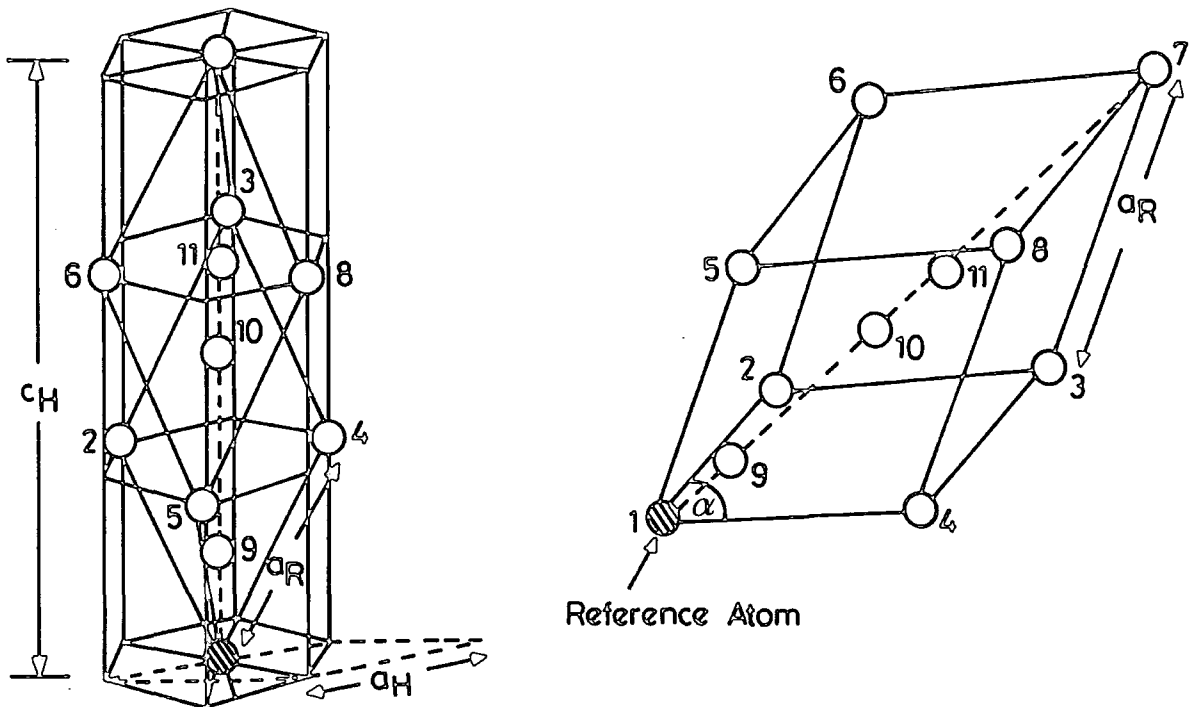
$$b_6^0 = +26.0 \pm 0.5 \quad |b_6^3| = < 1.0$$

The spin function operators  $O_n^m$  have the same transformation properties as the corresponding spherical harmonics  $Y_n^m$  and are fully described in papers, Baker, Bleaney and Hayes [3.4] and Judd [3.5]. Geschwind and Remeika [3.3] reported that the g value was equal to  $(1.9912 \pm 0.0005)$ .

The ionic radius of Gd in octahedral coordination is  $0.938\text{\AA}$  [3.3]. The Gd-Gd distance ranges around  $2.6\text{\AA}$  in a variety of compounds, Geller [3.6], while the Al-O distances in  $Al_2O_3$  are  $1.988\text{\AA}$  and  $1.845\text{\AA}$ . The cubic crystal field component of the ground state is approximately  $0.0621\text{cm}^{-1}$ . The unit cell of  $\alpha - Al_2O_3$  is rhombohedral, Fig. (3.1a), having three equal edges ( $a_R = 5.1374\text{\AA}$ ) and three equal



a)



b)

c)

Fig. (3.1) a) portion of the  $\text{Al}_2\text{O}_3$ . The  $\text{Al}^{3+}$  or  $\text{Gd}^{3+}$  are found between equally spaced planes of oxygen  
 b) Referred to the hexagonal lattice  
 c) Rhombohedral unit cell

interaxial angles ( $\alpha = 55^{\circ}17'$ ) Wyckoff [3.7]. However, it is more convenient to refer the unit cell to the hexagonal system with  $a_H = 4.7664\text{\AA}$  and  $c_H = 13.014\text{\AA}$ , Bragg and Bragg [3.8] as indicated in Figure (3.1b). There are two types of A1 sites which are physically equivalent and the  $Gd^{3+}$  entered selectively into one of these. The  $r, \theta, \phi$  values for all the sites are given in the reference, Thorp and Buckley [3.9]. It has been found that the aluminium sites lie on the surfaces of fifteen spheres. The first sphere corresponds to nearest neighbours, the next to the next nearest neighbours and so on; after the fifteenth sphere the interaction becomes negligible. It has been suggested that the ionic radius of  $Gd^{3+}$  is generally regarded as being twice that of  $Al^{3+}$ , yet at low levels of doping the  $Gd^{3+}$  can enter the lattice without disrupting its overall structure [3.3]. This means that at a concentration of 100 ppm, other rare-earth ions whose ionic radii are smaller than that of gadolinium could be incorporated into the  $Al_2O_3$  lattice.

In this Chapter the experimental and theoretical examination of the 9.5 GHz electron paramagnetic resonance spectrum of  $Gd^{3+}$  in single crystal alumina ( $Al_2O_3$ ) at room temperature will be discussed.

### 3.2 Experimental results

The E.P.R. spectra of  $Gd^{3+}/Al_2O_3$  single crystal was recorded on the Varian V4205-15 spectrometer at room temperature with the magnetic field perpendicular to

the  $\mathcal{C}$ -axis. More details of the technique can be found in several E.S.R. text books, an example of which is "A Comprehensive Treatise on E.S.R. Experimental Technique" by Poole [3.10]. The sample used for linewidth measurements was grown by Czochralski methods, and the gadolinium concentration was given as 100 ppm. The specimen was cut to suit the spectrometer cavity requirement. The recording shown in Figure (3.2) was made to establish the form of the first derivative spectrum. Only one line was observed where the seven transitions coincide at  $h\nu = g\beta H$ . The spectrum at  $\theta = 0$  (where the polar angle,  $\theta$ , is defined as the angle between the  $\mathcal{C}$ -axis and the magnetic field) shows a  $(1/2 \leftrightarrow -1/2)$  line, centred at about  $g = 1.993$ . This spectrum is due to  $Gd^{3+}$  ions occupying octahedral symmetry sites. It was first reported by Geschwind and Remeika [3.3]. Measurement of the  $(1/2 \leftrightarrow -1/2)$  peak to peak linewidths ( $\Delta H_{ms}$ ) were made as a function of polar angle, and the form of the variation can be seen in Fig. (3.3). This figure shows that the linewidth varies only slightly with polar angle; at  $\theta = 0^\circ$ ,  $\Delta H_{ms} = 0.9mT$  and there is a shallow maximum near  $\theta = 45^\circ$  at which  $\Delta H_{ms} = 1.2mT$ . The field values at which the transition occurred were also recorded as a function of polar angle Figure (3.4), and the plot showed that the  $(1/2 \leftrightarrow -1/2)$  transition was markedly anisotropic. These values were compared with the values reported by Geschwind et.al.[3.3] and showed close agreement. We estimated that the measurements obtained are accurate to about 10%. The angular positions, from which polar angles were derived, could be measured with precision from the large graduated turntable on which the magnet

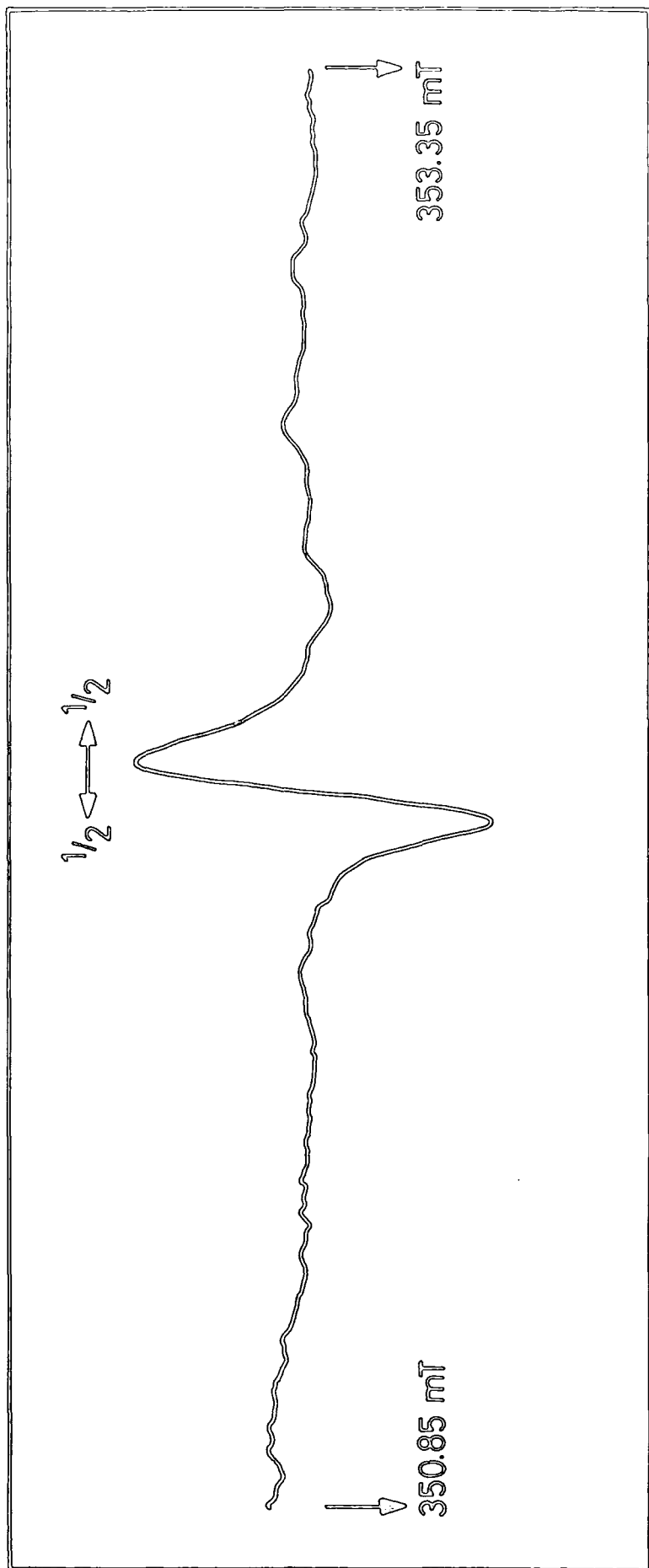


Fig. (3. 2) E.P.R. spectrum of single crystal  $Gd^{3+}/Al_2O_3$ ; 200 p.p.m. Gd, 293K,  $\theta_H = 0^\circ$ , 9.501GHz

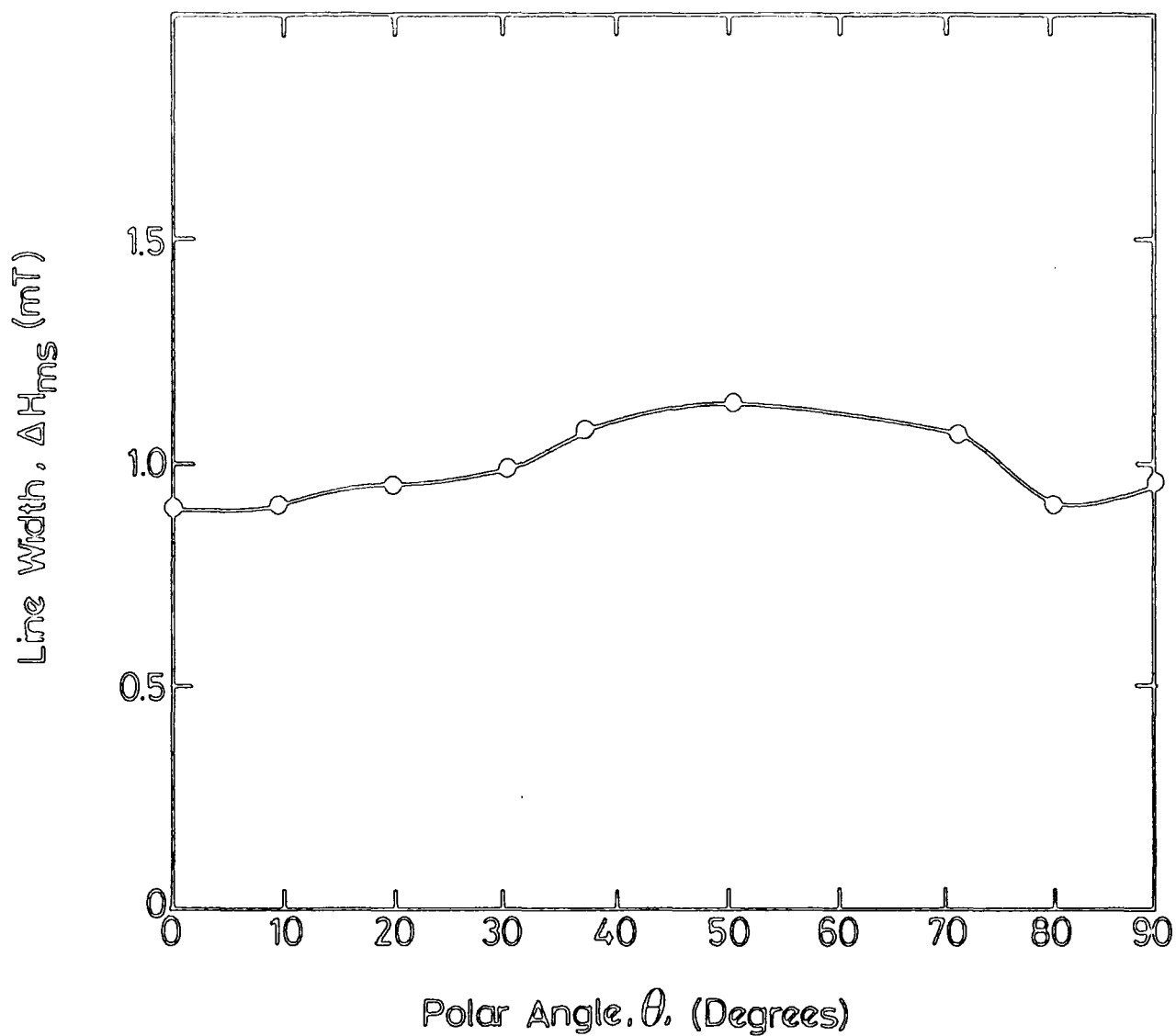


Fig. (3.3) Experimental-determination angular variation of linewidth

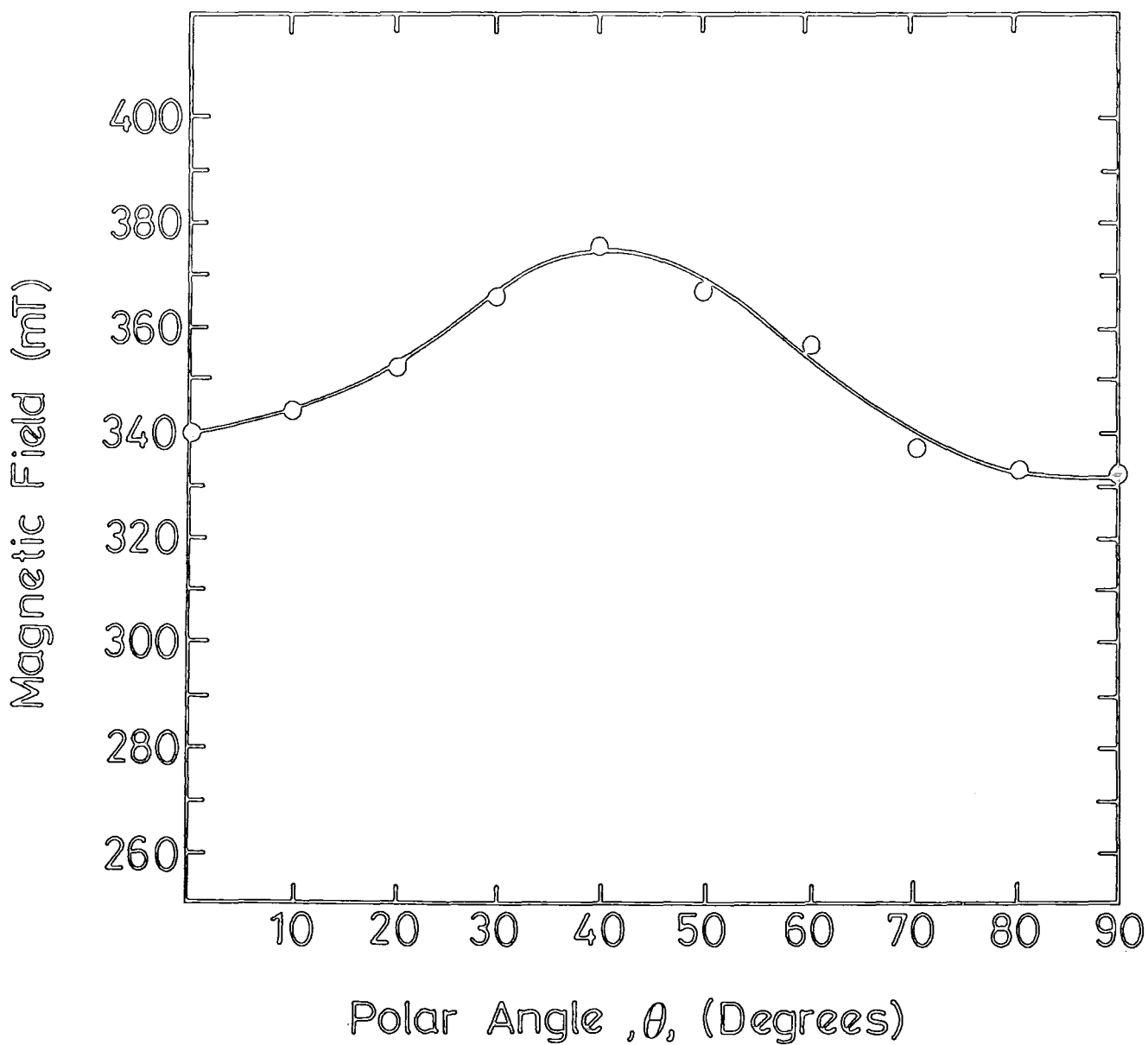


Fig. (3. 4) Variation of Resonance field of ( $\frac{1}{2} \longleftrightarrow -\frac{1}{2}$ ) transition with polar angle crystal  $Gd^{3+}/Al_2O_3$ , 200 p.p.m. Gd, 293K 9.502 GHz

was mounted; the major errors arose from the magnetic field calibrations and the difficulty in estimating the exact positions of the peaks on the spectrum.

### 3.3 Theoretical Linewidth

#### 3.3.1 Introduction

The calculation of dipolar broadening of the electron paramagnetic resonance lines of  $Gd^{3+}/Al_2O_3$  will follow the scheme previously described in Chapter 2. It is assumed that the principal homogeneous broadening mechanism is dipole-dipole interaction, and the magnitude of the homogeneous broadening is calculated using Van Vleck's second moment theory [3.11] and its extension by Kittel and Abrahams [3.12]. The steps in the calculation have been described in detail in Chapter 2, and only the basic outline and results will be presented here.

#### 3.3.2 Results I: The Van Vleck Model

In  $Gd^{3+}/Al_2O_3$  the dominant factor governing the dipolar linewidth will be the Gd-Gd interaction. However, there is the possibility of a smaller contribution from the Gd-Al interaction and this has been separately evaluated.

##### a) The Gadolinium - Gadolinium Interaction.

The second moment  $\langle \Delta\nu^2 \rangle$  of the linewidth caused by dipolar interaction for like

atoms in aluminium oxide has been shown in Chapter 2, (equation 2.22) and can be rewritten

$$\begin{aligned}
 \langle \Delta\nu^2 \rangle = & \frac{3}{4}S(S+1)\left(\frac{g^2\beta^2}{\hbar}\right)^2 .n \left\{ 0.8\sum_k r_{jk}^{-6} \right. \\
 & +4.787[Y_{2,0}^*(\theta_H, \phi_H)\sum_k r_{jk}^{-6} Y_{2,0}(\theta_k, \phi_k)] \\
 & +2.872[Y_{4,0}^*(\theta_H, \phi_H)\sum_k r_{jk}^{-6} Y_{4,0}(\theta_k, \phi_k)] \\
 & +2.872[Y_{4,3}^*(\theta_H, \phi_H)\sum_k r_{jk}^{-6} Y_{4,3}(\theta_k, \phi_k)] \\
 & \left. +2.872[Y_{4,-3}^*(\theta_H, \phi_H)\sum_k r_{jk}^{-6} Y_{4,-3}(\theta_k, \phi_k)] \right\} \quad 3.2
 \end{aligned}$$

The above equation is best described in two parts, the "atomic" part outside the curly brackets and the "geometric" part inside the curly brackets. Evaluation of the "atomic" part only required the knowledge of  $g$  and  $S$  for the gadolinium ion. It is worth emphasising the point that equation (3.2) is valid only for those atoms whose magnetic moment is given by  $g\sqrt{[S(S+1)]}$ . Gadolinium has a spectroscopic state  $8S_{7/2}$ , is an S-state ion, and has a magnetic moment given by the above formula with  $g=2$  and  $S=7/2$ . Therefore equation (3.2) is directly applicable. This atomic part can now be evaluated, giving

$$\frac{3}{4}S(S+1)\left(\frac{g^2\beta^2}{\hbar}\right)^2 .n = 1.256n \times 10^{-24}(\text{rad.}\text{sec}^{-1})\text{cm}^{-6}$$

where  $n$  is defined as the fraction of aluminium sites occupied by  $\text{Gd}$  ions. This is related  $x$ , the concentration in ppm, by the relation, Thorp et.al[3.9]

$$n = \frac{x}{x + 100}$$

Using Table (II) from reference [3.9], the "geometric" part of equation (3.2) can be partially evaluated, leading to the final equation.

$$\begin{aligned} \langle \Delta\nu^2 \rangle = & \frac{3}{4}S(S+1)\left(\frac{g^2\beta^2}{\hbar}\right)^2.n \times 20^{45} \left[ 12.847 \right. \\ & + 0.185Y_{2,0}^*(\theta_H, \phi_H) + 4.878Y_{4,0}^*(\theta_H, \phi_H) \\ & \left. - 4.025Y_{4,3}^*(\theta_H, \phi_H) + 4.025Y_{4,-3}^*(\theta_H, \phi_H) \right] \quad 3.3 \end{aligned}$$

We know from equation (2.20) that  $Y_{4,-3} = -Y_{4,3}^*$ ,  $Y_{2,0}^* = Y_{2,0}$ , and  $Y_{4,0}^* = Y_{4,0}$ . These give a difference in sign but in this case one also has a term  $\exp(i3\phi)$  which is always found to have the value zero, (given the same value for  $Y_{4,3}$ ); since the imaginary terms are always zero  $Y_{4,-3} = -Y_{4,3}$ . By taking  $\phi = 0$ , and substituting the values of  $n$  and  $g$  corresponding to the values used experimentally, curves of dipolar broadening as a function of polar angle,  $\theta$ , can be derived. Using the transformation equation

$$\Delta H_{ms} = \frac{\sqrt{\langle \Delta\nu^2 \rangle}}{\pi} \frac{\partial\nu}{\partial H} \times 10^3 mT \quad 3.4$$

$\Delta H_{ms}$  can be calculated and compared with the experimental values,(c.f.Chapter 2). The general theoretical curve is given in Figure (3.5). The linewidth is about 16mT at  $\theta = 0^0$ , falling to about 10 mT near  $\theta = 45^0$  and rising again to 19mT at  $\theta = 90^0$ .

### b) The Gadolinium-Aluminium Interaction

For estimating the Gd-Al interaction, equation (2.23) in Chapter 2 can be rewritten giving the following form:

$$\begin{aligned} \langle \Delta\nu^2 \rangle = & \frac{1}{3}S(S+L)\left(\frac{gg'\beta^2}{\hbar}\right)^2 .n \left\{ 0.8 \sum_k r_{jk}^{-6} \right. \\ & +4.787[Y_{2,0}^*(\theta_H, \phi_H) \sum_k r_{jk}^{-6} Y_{2,0}(\theta_k \phi_k)] \\ & +2.872[Y_{4,0}^*(\theta_H, \phi_H) \sum_k r_{jk}^{-6} Y_{4,0}(\theta_k \phi_k)] \\ & +2.872[Y_{4,3}^*(\theta_H, \phi_H) \sum_k r_{jk}^{-6} Y_{4,3}(\theta_k \phi_k)] \\ & \left. +2.872[Y_{4,-3}^*(\theta_H, \phi_H) \sum_k r_{jk}^{-6} Y_{4,-3}(\theta_k \phi_k)] \right\} \quad 3.5 \end{aligned}$$

However, in this interaction, the gadolinium is interacting with the nuclear spin of  $Al^{3+}$  whereas in that between Gd - Gd there is an electronic interaction. From

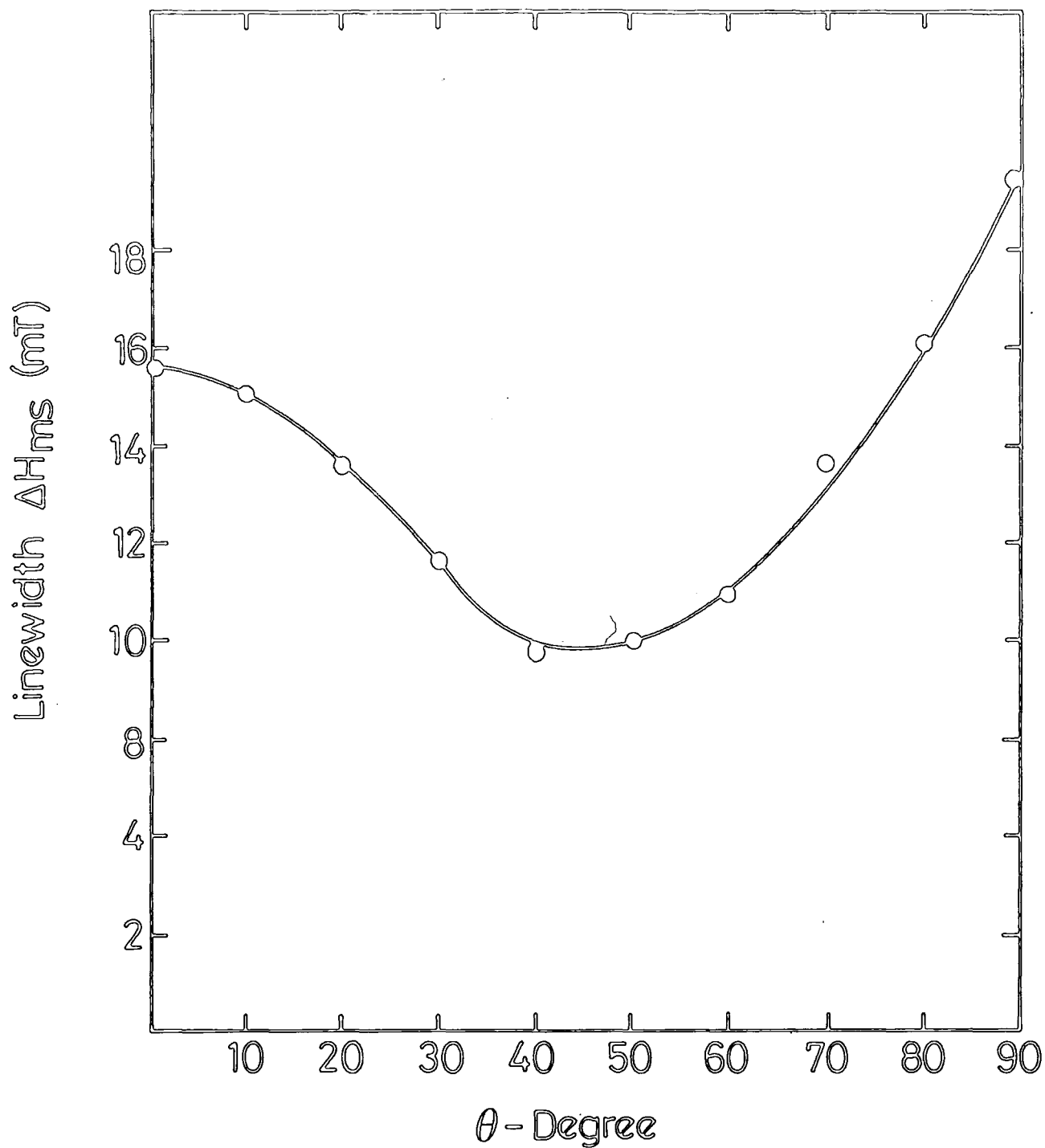


Fig. (3.5) Theoretical angular variation of linewidth.

n.m.r. tables, the nuclear  $g$  is 1.455 but for inclusion in the equation it must be multiplied by the ratio of the nuclear magneton to the Bohr magneton, i.e. giving  $g^{\text{N}} = 1.455/1836$ . Evaluation of equation 3.5 gives a linewidth due to the Gd-Al interaction of only about 0.04 mT.

The theoretical linewidths for the Gd - Gd interaction are all greater than the experimental values, for example, at  $\theta = 0^\circ$  by approximately a factor of sixteen. This is neglecting the effect of the Gd - Al interactions, which would have increased the total theoretical width by about 3%.

### 3.3.3 Results II: The Kittel and Abrahams' Model

The calculation of the dipolar linewidth based on Kittel and Abrahams' extension of Van Vleck's theory, (section 2.3.2, Chapter 2) gave the following

$$\sum_k \beta_{jk}^2 = \left(\frac{3}{2}g^2\beta^2\right)^2 \sum_k r_{jk}^{-6} (3\cos^2\theta - 1)^2 \quad 3.6$$

and also

$$\sum_k \beta_{jk}^4 = \left(\frac{3}{2}g^2\beta^2\right)^4 \sum_k r_{jk}^{-12} (3\cos^2\theta - 1)^4 \quad 3.7$$

The values of  $\sum r_{jk}^{-6}$  are given in Table (II) of reference [3.9] and those of  $\sum r_{jk}^{-12}$

have been calculated from data given in the same Table. To facilitate calculation equations (3.6) and (3.7) can be written in terms of spherical harmonics as

$$\begin{aligned} \sum_k \beta_{jk}^2 &= \left(\frac{3}{2}g^2\beta^2\right)^2 \times 10^{45} [12.847 \\ &\quad + 0.185Y_{2,0}^*(\theta_H, \phi_H) + 40878Y_{4,0}^*(\theta_H, \phi_H) \\ &\quad - 4.075Y_{4,3}^*(\theta_H, \phi_H) + 4.025Y_{4,-3}^*(\theta_H, \phi_H)] \quad 3.8 \end{aligned}$$

it is also found that

$$\begin{aligned} \sum_k \beta_{jk}^4 &= \left(\frac{3}{2}g^2\beta^2\right)^4 \times 10^{90} [31.4373 \\ &\quad + 0.5573Y_{2,0}^*(\theta_H, \phi_H) + 17.144Y_{4,0}^*(\theta_H, \phi_H) \\ &\quad - 14.339Y_{4,3}^*(\theta_H, \phi_H) + 14.339Y_{4,-3}^*(\theta_H, \phi_H)] \quad 3.9 \end{aligned}$$

The geometric part of the above equation can be evaluated and it is relatively simple to evaluate the atomic part of the expression given the  $g$  value. Equation (2.32) is used and the linewidth is given as

$$\Delta H_{ms} = 0.0193f \text{ mT}$$

For the concentration of 100 ppm

$$\Delta H_{ms} = 0.193 \text{ mT}$$

Thus the Kittel and Abrahams' model predicts a linewidth which is much less than that predicted by the simple Van Vleck model.

### 3.4 Discussion

Looking at previous results, Figure (3.4), represents the situation where the magnetic field is rotated in the  $(10\bar{1}0)$  plane. The angular variation of  $(1/2 \leftrightarrow -1/2)$  transition shown in Figure (3.5) is comparable with the plot in Figure (3.3). The predicted linewidths (Van Vleck) are about sixteen times greater than the observed linewidths. Similar comparisons have been made. For example, in *Na/CaWO<sub>4</sub> crystals*, Brown et.al.[3.13] found that the predicted widths agreed closely with those observed. In double doped alumina *Cr/Ti/Al<sub>2</sub>O<sub>3</sub>* Thorp.et.al [3.9] found that the predicted widths were seven times larger than those observed and in gadolinium doped calcium tungstate, Thorp.et.al [3.14] found a similar factor. In these examples there was reasonably good correlation between the forms of the predicted and observed angular variations of the linewidths and also between the linewidth versus concentration variation. With the present data, only the form of the angular variation of the linewidth corresponds.

The experimental observation of  $Gd^{3+}$  in the substitutional site indicates that in the

substitution of  $Gd^{3+}$  for  $Al^{3+}$  (whose ionic radius is half as large) at level less than 0.2%, matching of ionic radii is not an all important criterion for incorporation into the lattice. In most rare earths, the screened position of the  $4f$  electrons makes exchange interaction unlikely. However, gadolinium is one of the few rare earths to give an E.P.R. spectrum at room temperature which makes it different. In addition, below 289K, gadolinium metal is ferromagnetic and it is possible that there is some exchange interaction.

At the low level of Gd concentration (i.e. 100 ppm) used, the Gd-Gd spacings are large because the Gd atoms are separated by many unit cells. Under these conditions, however, exchange interactions could hardly have any appreciable effect on the absorption linewidth (exchange interactions usually occur over distances of not more than a few unit cell parameters). Consequently, exchange effects at such a low Gd concentration can be neglected.

## REFERENCES

- 3.1 V.M. Vonokurov and V.G. Stephanov. *Sov. Phy. Sol. Stat.* 9 844 (1967).
- 3.2 R.P. Hunt and K.N.R. Taylor. *J. Mater. Sci.* 8, 203 (1973).
- 3.3 S. Geschwind and J.P. Remeika. *Phys. Rev.* 122, No3 (1961).
- 3.4 J.M. Baker, B. Bleaney and Hayes. *Proc. Roy. Soc. ,London*, A247, 141 (1958).
- 3.5 B.R. Judd. *Proc. Roy. Soc. ,London*, A227, 522 (1955).
- 3.6 S Geller. *Acta Cryst.* 10, 27 (1957).
- 3.7 R.W.G. Wyckoff. "*Crystal Structure*" Interscience, New York, (1957).
- 3.8 W.H. Bragg and W.L. Bragg. "*X-rays and Crystal Structure*", Bell and Sons London (1924).
- 3.9 J.S. Thorp, H.P. Buckley. *J. Mater, Sci.* 9, 1499 (1974).
- 3.10 C.P. Poole. "*A Comprehensive Treatise on E.S.R. Experimental Technique*". Inter Science, N.Y. (1967).
- 3.11 J.H. Van Vleck, *Phys, Rev.* 74, 1168 (1948).
- 3.12 C. Kittel and E. Abrahams. *Phys. Rev.* 90, 238 (1953).

3.13 G. Brown, C.J. Kirkby and J.S. Thorp. *J. Mater. Sci.* 9, 65 (1974).

3.14 J.S. Thorp, G. Brown and H.P. Buckley. *J. Mater Sci.* 9, 1337 (1970).

## CHAPTER FOUR

### E.P.R. INVESTIGATIONS OF CHROMIUM IN ALUMINIUM OXIDE SINGLE CRYSTALS AND POWDERS

#### 4.1 INTRODUCTION

Ruby is important as a laser material, having been among the first few single crystal solid state materials in which laser action was reported, Maiman [4.1]. Aluminium oxide is trigonal with lattice parameters  $a = 4.758\text{\AA}$ ,  $c = 12.991\text{\AA}$  [4.2], which are substantially unaffected by the addition of small doping levels of chromium. In ruby the aluminium atoms are found between the planes of oxygen in equivalent sites. The octohedral co-ordination is severely distorted and  $C_{3v}$  is the only site symmetry. The electron configuration for the free Cr ion is  $3d^3$ , with a 4f ground state. The crystal field in  $Al_2O_3$  at the Cr site is trigonal ( $C_{3v}$ ) and is the same for all Cr ions. The splitting of the ground state levels for all levels as a function of magnetic field together with the observable transitions at 9.56 Hz are shown in Fig [4.1]. Detailed discussion of the energy levels of  $Cr^{3+}$  in  $Al_2O_3$  can be found in the review papers by Sugano and Tanabe [4.3] and by Tsujikawa [4.4].

Ruby crystal has high chemical stability, a low dielectric loss and good thermal properties. In the ruby lattice different ion groups can be incorporated, e.g.  $Cr^{3+}$ ,  $Fe^{3+}$

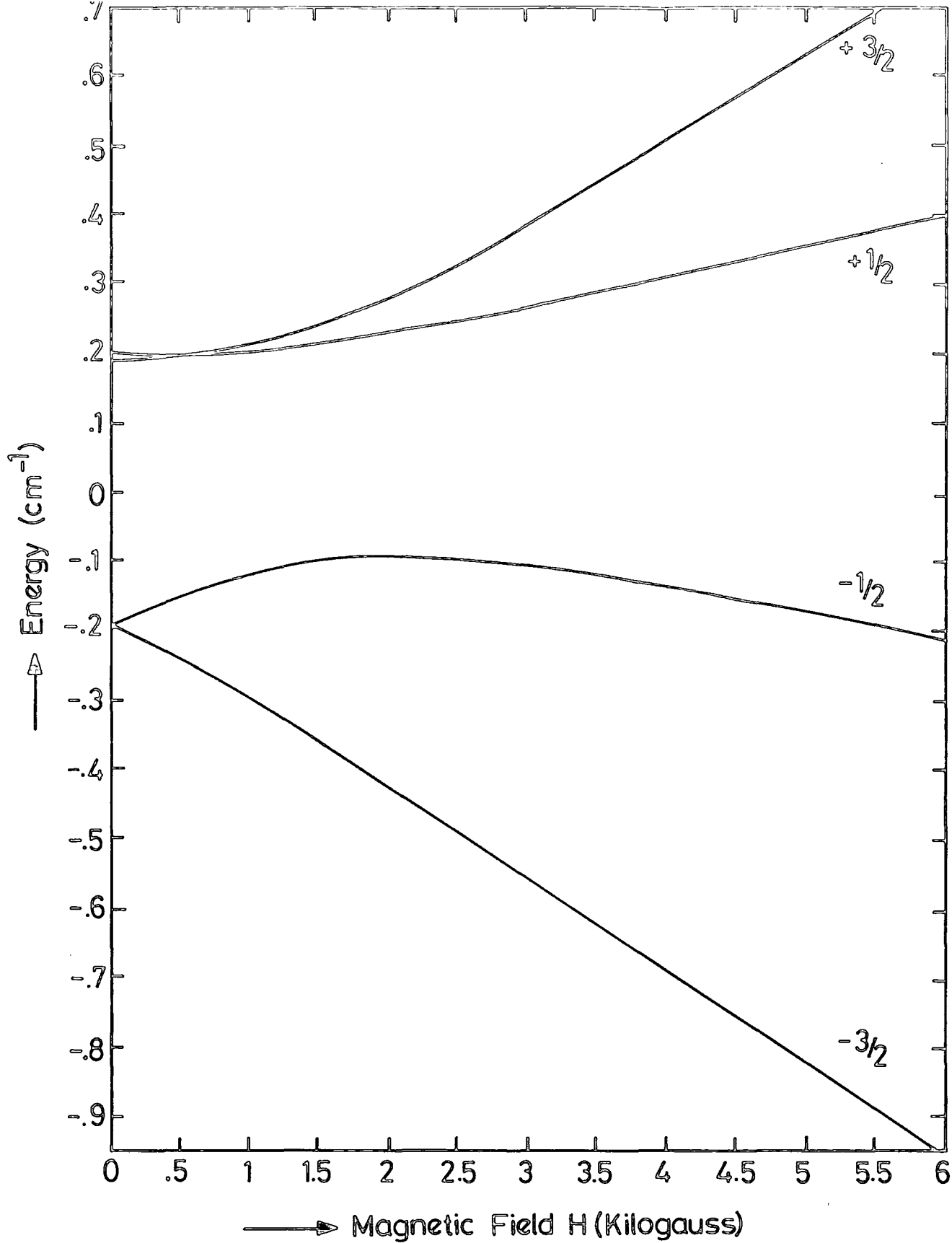


Fig. (4.1) Energy level diagram of Cr<sup>3+</sup> in Al<sub>2</sub>O<sub>3</sub> (Howarth [4.2]) with the magnetic field perpendicular to the C-axis

and  $Cu^{3+}$ . Their early E.S.R. properties have been studied by Howarth [4.5], [4.6] and Low [4.7]. respectively. Paramagnetic resonance for  $Cr^{3+}/Al_2O_3$  as a single crystal has been reported in the literature [4.8, 4.9, 4.10]. Unfortunately there is not much information about the powder form. One of the first detailed investigations of ruby doped with chromium at room temperature was reported by Howarth [4.8] and Grant [4.9]. The E.S.R. spectrum is described by the Spin Hamiltonian which takes the form, ( Howarth, 1958)

$$\mathcal{H} = \beta g_{\perp} H_x S_x + \beta g_{\parallel} (H_y S_y + D(S_z^2 - \frac{1}{3}S(S+1))) \quad 4.1$$

with  $S = 3/2$ .

Howarth reported that the g values were equal to ( $g_{\perp} = 2.00 \pm 0.002, g_{\parallel} = 2.003 \pm 0.006$ ) and Manenkov and Prokhorov remeasured them, reporting similar g values of  $g_{\perp} = 1.9894$  and  $g_{\parallel} = 1.9867$ . The crystal field parameter D has the value 5.75 kKHz [4.4]. The energy levels and transition probabilities derived from the Spin Hamiltonian have been worked out in detail by Davis and Strandberg [4.10] and by Schulz- Dubois [4.11] The hyperfine interaction with the  $Cr_{53}$  nucleus (10% natural abundance) certainly exists and was observed first by Manenkov and Prokhorov [4.11]. The hyperfine separation has been measured for atomic aluminium [4.13] and is 1450MHz.

In this Chapter the experimental and theoretical examination of the 9.5 GHz electron spin resonance of  $Cr^{3+}$  in both single crystal and powder forms of alumina ( $Al_2O_3$ ) will be studied; all the data refers to room temperature but a limited range of chromium concentration was examined.

#### 4.2 Experimental results of $Cr^{3+}/Al_2O_3$ single crystals

The E.P.R. spectra of  $Cr^{3+}/Al_2O_3$  were recorded on the Varian V4205-12 Spectrometer at room temperature, with the magnetic field perpendicular to the  $c$ -axis. In all, five samples were examined, in which the concentration of the chromium dopant ranged from 150 ppm to 2000 ppm; these concentrations were determined using X-ray fluorescence techniques. The complete list of chromium concentrations can be seen in Table (4.1).

Several recordings of the first derivative spectra were obtained for each of the specimens examined. The particular spectrum illustrated in Fig (4.2a) was obtained from a sample with a chromium concentration of 530 ppm. The spectrum in Fig(4.2b) at  $\theta = 0^\circ$  (where  $\theta$  is the angle between the magnetic field's direction and the crystallographic  $c$ -axis) shows several lines of which the central line is at approximately  $g = 1.987$ . A similar value observed for  $Cr^{3+}/Al_2O_3$  has been reported [4.7] and [4.8].

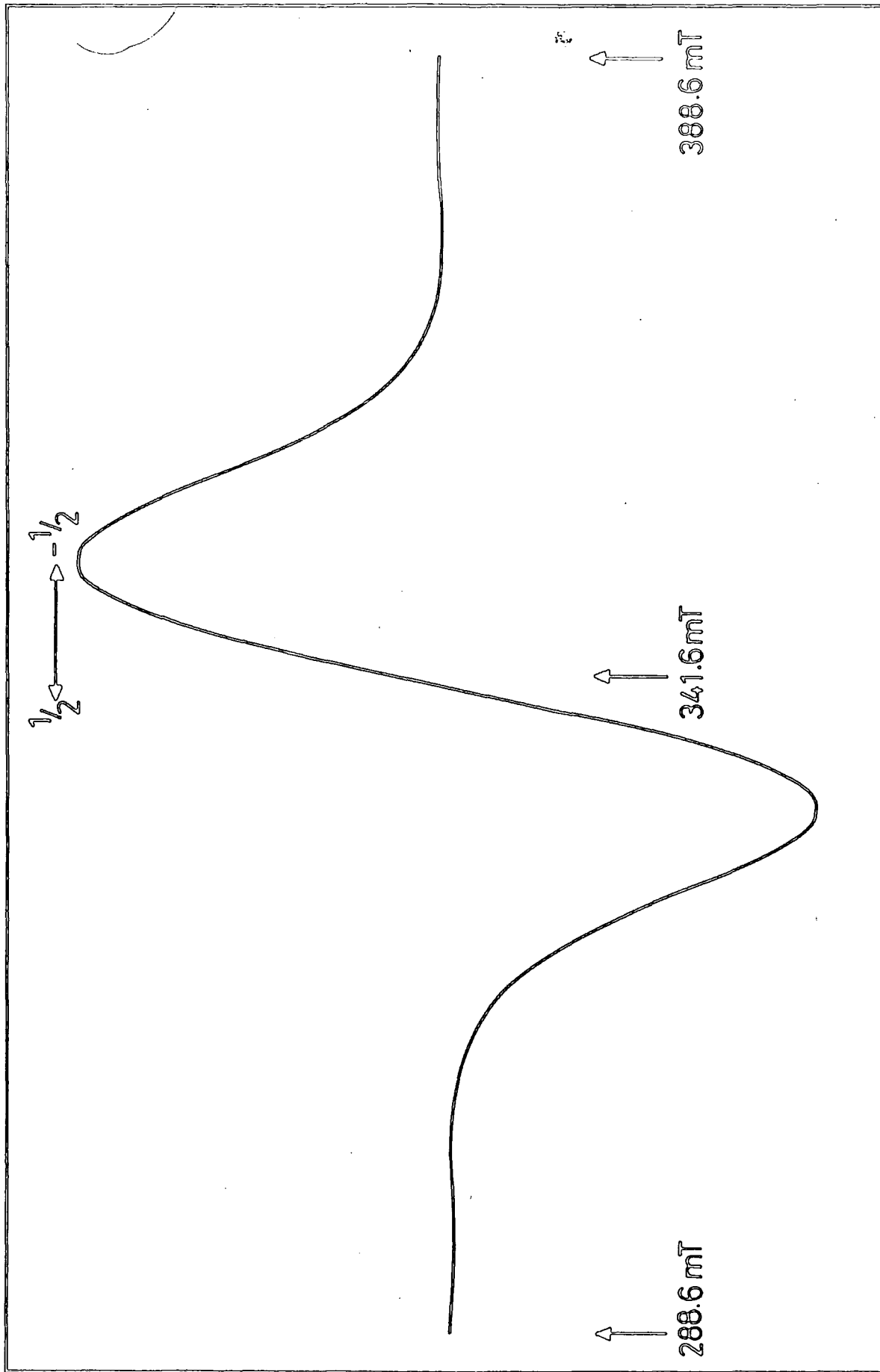


Fig. (4.2a) E.P.R. Spectrum of single crystal  $\text{Cr}^{3+}/\text{Al}_2\text{O}_3$ : 530 p.p.m., Cr 293K,  $\theta_H = 0$ , 9.502 GHz

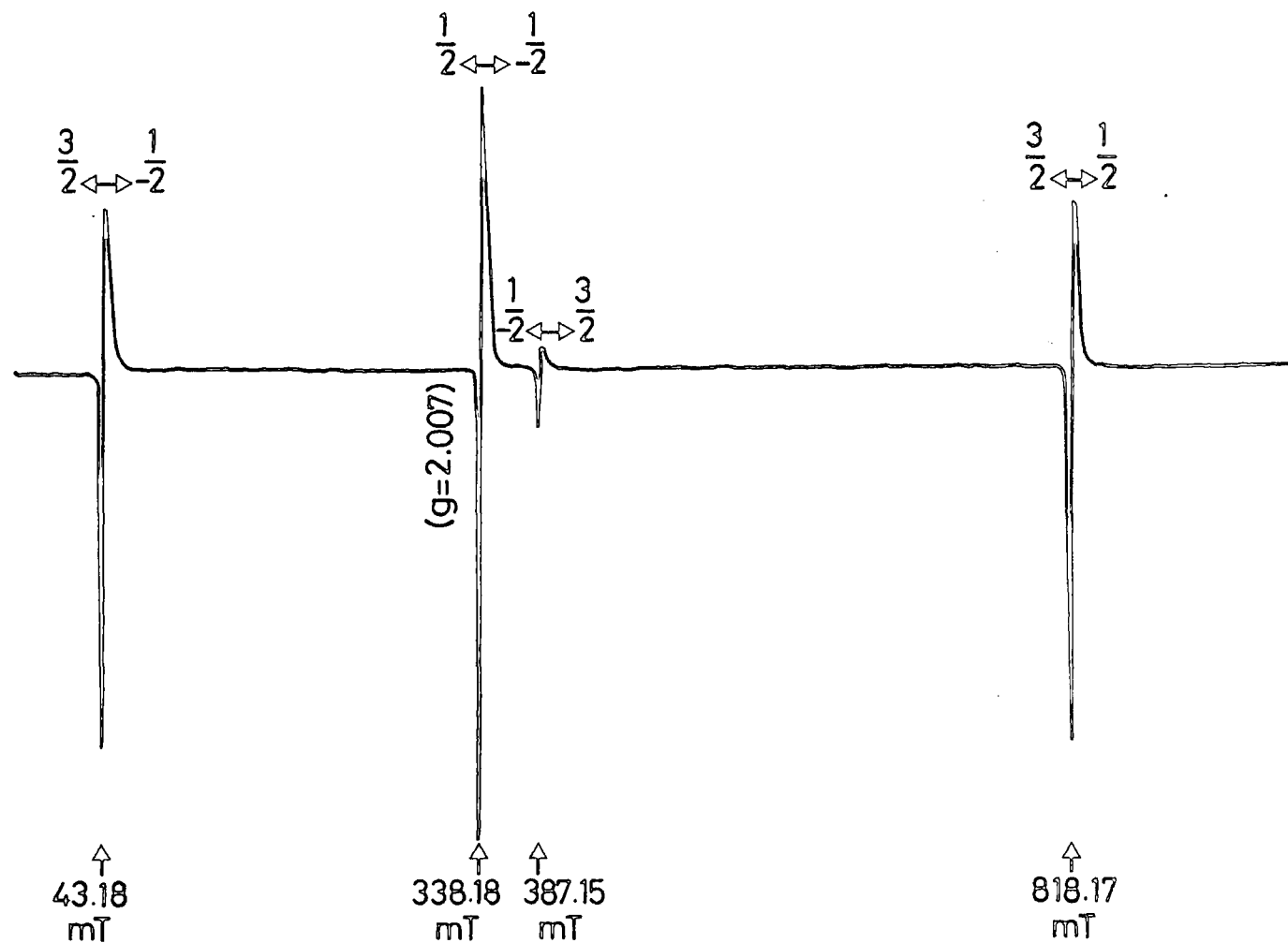


Fig. (4.2b) Extended E.P.R. spectrum of single crystal  $\text{Cr}^{3+}/\text{Al}_2\text{O}_3$ ; 530 p.p.m. Cr; 293K, 9.486 GHz

The angular variation of the  $(1/2 \leftrightarrow -1/2)$  transition was investigated for the sample containing 530 ppm of chromium. Our measurements were restricted to one dopant concentration because it was assumed that the general characteristics displayed by the angular variation of the spectrum at one particular dopant concentration would be common to all the samples, whatever the dopant concentration. This is a reasonable assumption to make since the  $Cr^{3+}$  centre responsible for the spectrum should have identical properties in each of the five chromium doped aluminium oxide samples examined. The spectra were recorded at  $10^\circ$  intervals between  $\theta = 0^\circ$  and  $\theta = 90^\circ$  as the crystals doped with 530 ppm of chromium were rotated in C-axis. The variations of all the transitions are depicted in Fig. (4.3). The  $(1/2 \leftrightarrow -1/2)$  transition and the other transitions such as  $(3/2 \leftrightarrow -1/2)$ ,  $(-1/2 \leftrightarrow 3/2)$  and  $(+3/2 \leftrightarrow -3/2)$  were markedly anisotropic. The field values at which the transitions occurred were compared with the values expected from the energy level diagram [4.7] and close agreement was found. At the same time there were similarities between the transitions of the feature of Fig. (4.2) and the plot for the same transitions in Fig. (4.1).

The g factor and peak-to-peak linewidth of the  $(1/2 \leftrightarrow -1/2)$  central transition ( $\Delta H_{ms}$ ) were determined for each of the spectra recorded at  $10^\circ$  intervals from the sample doped with 530 ppm of chromium and listed in Table (4.1). Fig (4.4) shows a plot of the average width of the  $(1/2 \leftrightarrow -1/2)$  transition against the

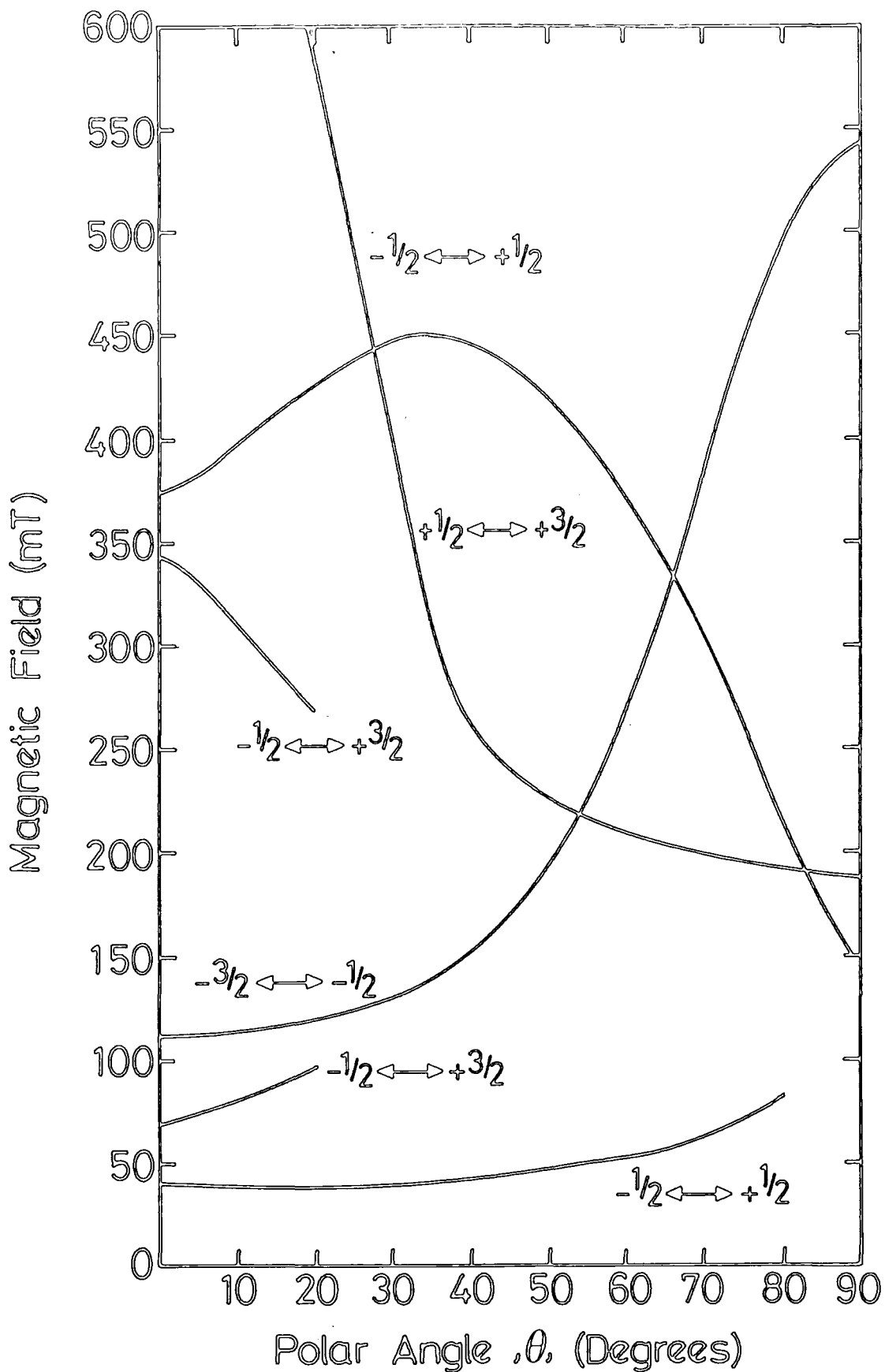


Fig. (4.3) Variation of Resonance field with polar angle, single crystal  $\text{Cr}^{3+}/\text{Al}_2\text{O}_3$ , 530 p.p.m Cr, 293K, 9.496 GHz

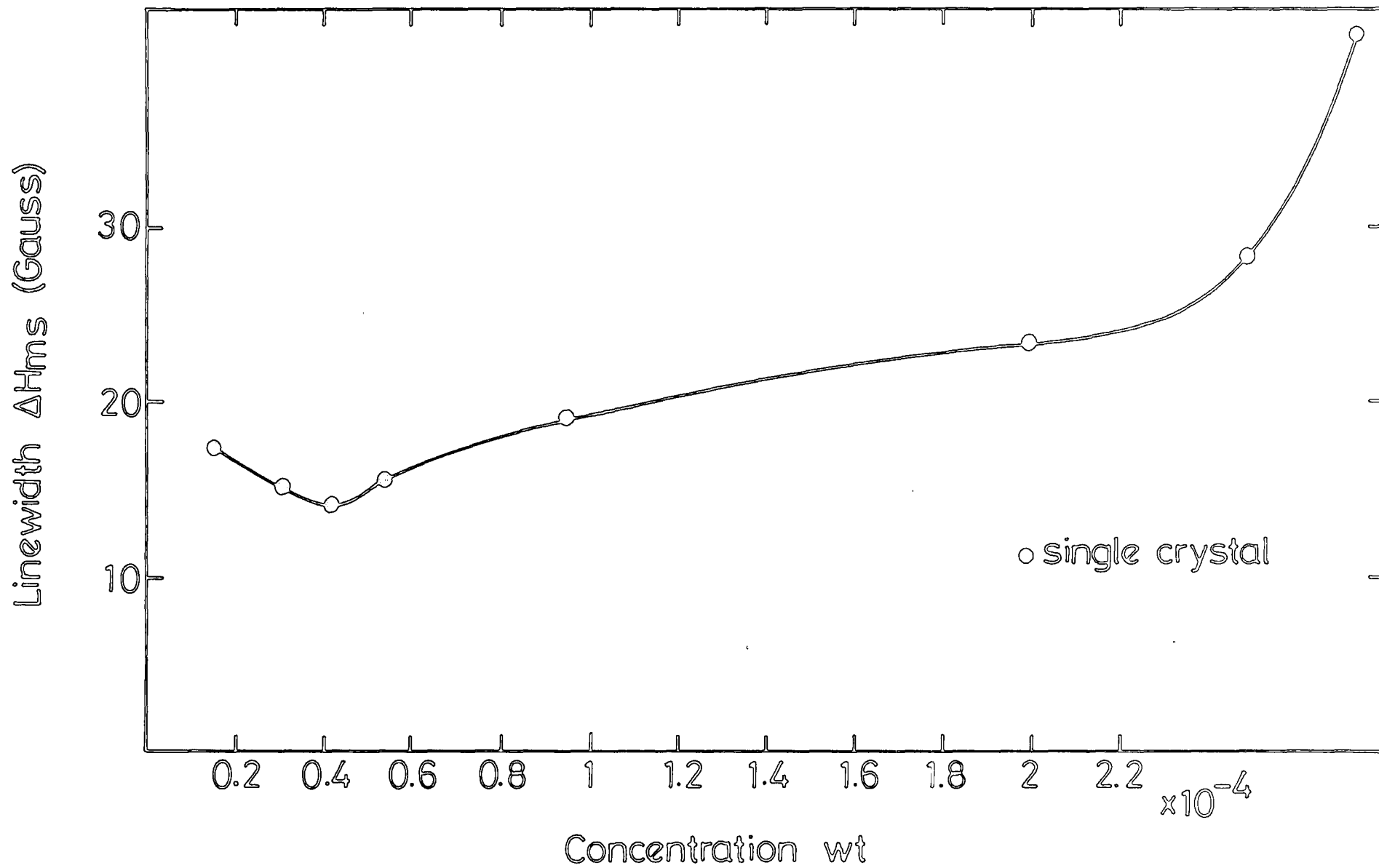


Fig. (4.4) Variation of experimental linewidth with concentration;  $\theta_H = 0^\circ$ , 293K. 9.486 GHz

Chromium concentration ppm	g Factor	Experimental Linewidth $\Delta H_{ms}(mT)$	Calculated Van Vleck Linewidth $\Delta H_{ms}(mT)$
150	1.986	1.75	6.72
310	1.987	1.50	9.621
420	1.986	1.48	11.23
530	1.987	1.56	12.26
870	1.986	1.87	16.13
2000	1.986	2.32	24.52

Table 4.1 E.P.R. parameters for single crystal  $Cr^{3+}/Al_2O_3$  samples; 293k and 9.50 GHz

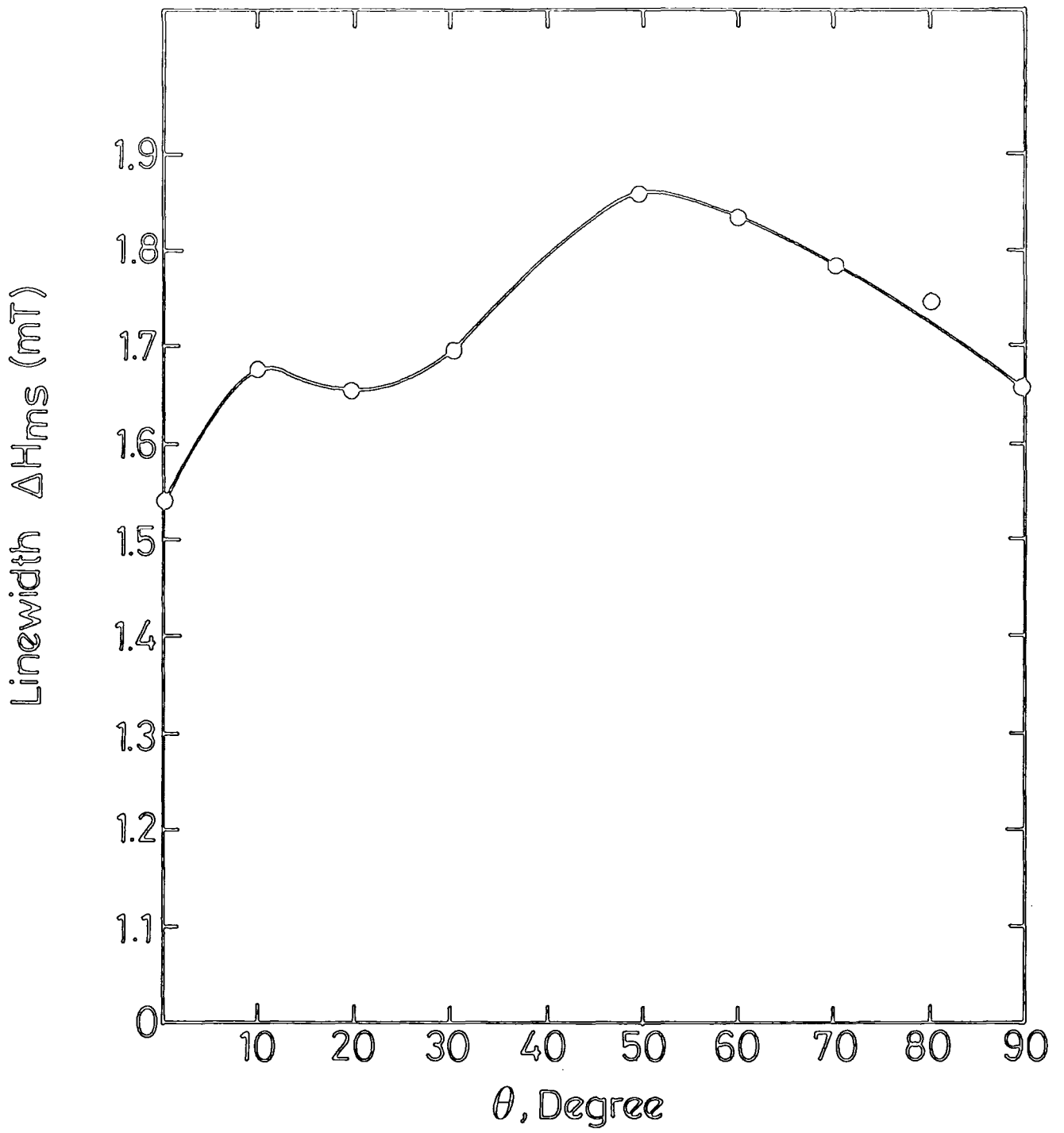


Fig (4.5) Experimental angular variation of Linewidth

chromium concentrations. The linewidth variation for the  $(1/2 \rightarrow -1/2)$  transition as a function of  $\theta$  are depicted in Figure (4.5).

### 4.3 Theoretical calculation for single crystal

#### 4.3.1. Van Vleck dipolar broadening theory

The complete Van Vleck Theory [4.15] has been described in Chapter 2, section 2.3.1. For  $Cr^{3+}/Al_2O_3$  the general expression for the second moment is given by:-

a) for like atoms

$$\begin{aligned} \langle \Delta\nu^2 \rangle = & \frac{3}{4}S(S+1)\left(\frac{gg'\beta^2}{\hbar}\right)^2.n \times 10^{45} [12.847 \\ & +0.185Y_{2,0}^*(\theta_H, \phi_H) + 4.878Y_{4,0}^*(\theta_H, \phi_H) \\ & -4.025Y_{4,3}^*(\theta_H, \phi_H) + 4.025Y_{4,-3}^*(\theta_H, \phi_H)] \quad 4.2a \end{aligned}$$

b) for unlike atoms

$$\begin{aligned} \langle \Delta\nu^2 \rangle = & \frac{1}{3}S(S+1)\left(\frac{gg'\beta^2}{\hbar}\right)^2.n \times 10^{45} [12.847 \\ & +0.185Y_{2,0}^*(\theta_H, \phi_H) + 4.878Y_{4,0}^*(\theta_H, \phi_H) \\ & -4.025Y_{4,3}^*(\theta_H, \phi_H) + 4.025Y_{4,-3}^*(\theta_H, \phi_H)] \quad 4.2b \end{aligned}$$

For like atoms the first term (i.e. the atomic part) becomes:-

$$\frac{3}{4}S(S+1)(g^2\beta^2/\hbar)^2.n = 2.989 \times 10^{-25}.n(\text{rad.}\text{sec}^{-1})^2\text{cm}^6$$

and for unlike atoms it is

$$\frac{1}{3}S(S+1)(gg'\beta^2/\hbar)^2.n = 0.266 \times 10^{-25}.n(\text{rad.}\text{sec}^{-1})^2\text{cm}^6$$

Converting from  $\Delta\nu$  to  $\Delta H_{ms}$  via the expression

$$\Delta_{ms} = \frac{\sqrt{\langle \Delta\nu^2 \rangle}}{\pi} \frac{\partial H}{\partial \nu} \times 10^3 \text{mT} \quad 4.3$$

gives the theoretical linewidths shown in the last column of Table (4.1) and in Fig (4.6). It is seen from this that the linewidth is near 12 mT over the whole of the angular range.

#### 4.3.2 Kittel and Abrahams' model

The calculation of the dipolar linewidths based on Kittel and Abrahams' model [4.16] follows the procedure described in Chapter 3. Here of course there is a difference in the atomic part and the effect of these changes is that

LINE WIDTH, Δrms (nm)

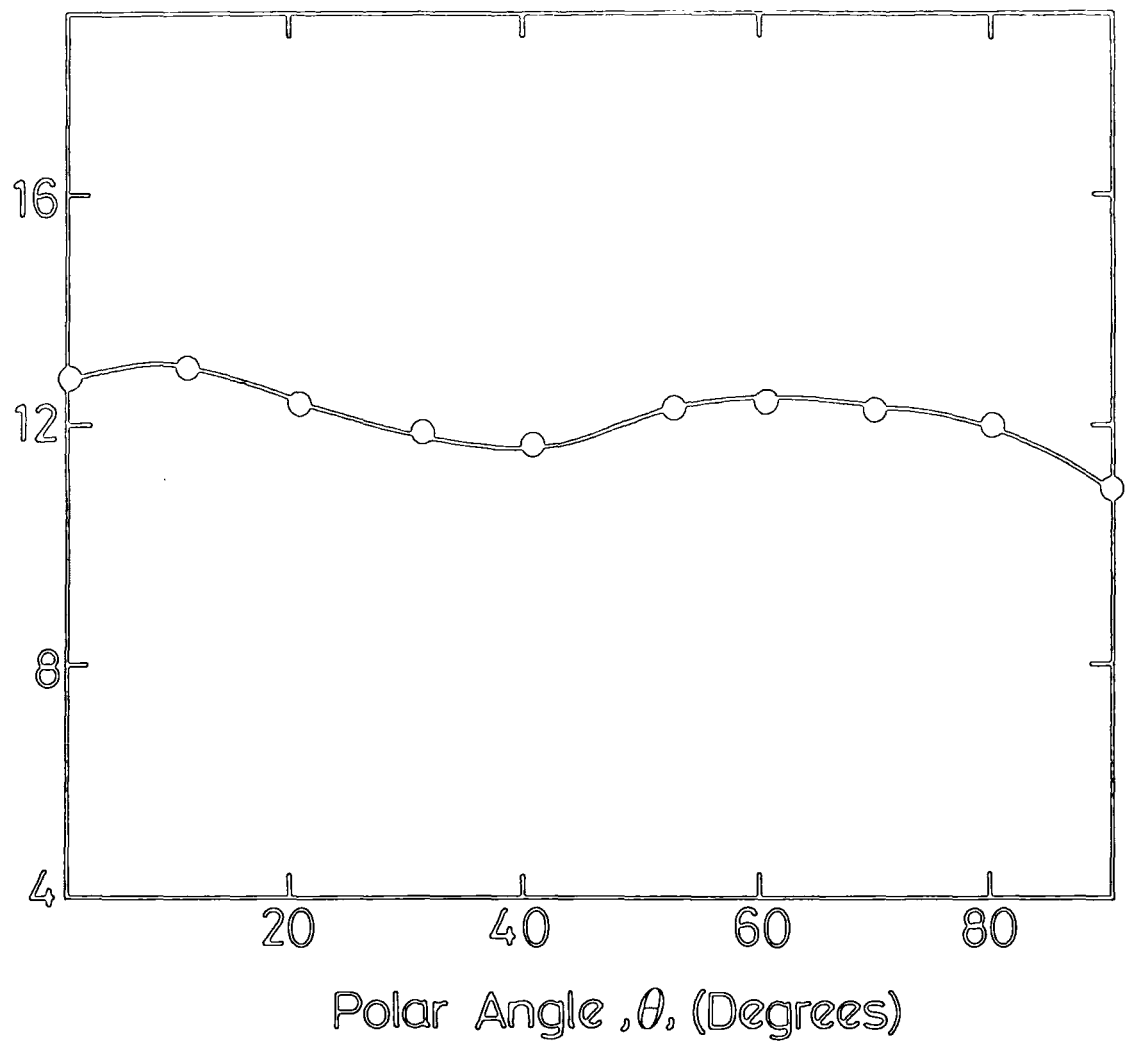


Fig. (4.6) Theoretical angular variation of linewidth

$$\Delta H_{ms} = 0.965 \times 10^{-4} \times f \text{ mT}$$

For the concentrations of 530 ppm and 2000 ppm, the linewidths are 4.827 mT and 19.30 mT respectively. (on the Kittel and Abrahams' model, the linewidth varies directly as f.)

### 4.3.3 de Biasi and Fernandes' model

The theoretical peak-to-peak linewidths predicted by de Biasi and Fernandes' dipolar broadening theory [4.17] for six different ranges of the exchange interaction have been derived. The parameter A(s) was determined from equation (2.35a) with  $g=1.98, a=4.758$  and  $S = 3/2$ . This was repeated for each value of n, using equation (2.34) and the appropriate values of  $S_1(\theta)$ , and  $S_2(\theta)$  given in Table (2.2). The experimental linewidths of the  $(1/2 \leftrightarrow -1/2)$  line for a chromium concentration of 530 ppm do not agree with any of the theoretical values predicted by de Biasi and Fernandes' model which ranged from  $4.006 \times 10^{-4} mT$  for  $n = 1$  to  $1.47 \times 10^{-9} mT$  for  $n = 4$ . However, it is likely that this discrepancy is due to the fact the de Biasi and Fernandes' theory only applies to powdered samples.

The experimental linewidth for  $Cr^{3+}/Al_2O_3$  powder samples will be compared with the theoretical linewidth in order to assess properly whether the application of de Biasi and Fernandes' model to the  $Cr^{3+}/Al_2O_3$  system is valid.

#### 4.4 Discussion of the single crystal results

We first summarise the most important feature of the experimental results. The experimental linewidth appears to be almost concentration independent below 1000 ppm and dependent above that. Furthermore, the observed linewidth appears dependent on polar angle which shows a maximum when  $\theta$  lies between  $45^\circ$  and  $55^\circ$ . Comparing these observations with the Van Vleck theory, it can be seen that the linewidths predicted from this theory are six times larger than the observed linewidths. On the other hand the theoretical linewidths predicted by Kittel and Abrahams' model were found to be concentration dependent and produced a close agreement with the experimental linewidth.

The Cr-Al interaction, as noted in Chapter 3 for Gd-Al, produces a smaller effect than the other Cr-Cr interaction. The actual value of  $\Delta H_{ms}$  for this interaction was found to vary between 0.2 and 0.5mT in the Gd-Al interaction. There is a close proximity in the magnitude with the experimental linewidths, only a small part of the total width is due to the Cr-Al broadening. Also, the theoretical Cr-Cr linewidth is much greater than the Cr-Al interaction. There is an agreement with work done by Manenkov and Prokhorov [4.18], Grant and Strandberg [4.8] and Thorp [4.19]. Grant and Strandberg [4.8] discussed the lineshape results of ruby from the continuous distribution of dipoles cutting off at an inner radius  $r$ . At low concentrations ( $< 0.5\%$ ) for the transition the line was Lorentzian in shape having a

concentration independent width given by  $\Delta H = 12.6 Gauss$ . Interactions between the chromium ions themselves are independent of interaction between the ions and the lattice. In these circumstances the overall lineshape is obtained by convolution of the various components, and, at low concentrations, the experimental lineshape is Gaussian with independence of concentration up to about 0.1%. As concentration increases the Lorentzian dipolar component takes over, but this trend is reversed as the dipolar line becomes Gaussian. The interactions at high concentrations result in a greater Lorentzian dipolar contribution to the overall line, causing departures from the Gaussian shape. Such departures have been observed [4.8] and are shown in Fig. (4.7)

#### 4.5 Characterisation of the EPR spectra of the $Cr^{3+}/Al_2O_3$ powdered samples

Powders were prepared by grinding a small amount of single crystal using a Glen Creaston tungsten carbide ball mill. Spectra were recorded from all five powder samples on the Varian V4205-15 EPR spectrometer at room temperature. The traces obtained were very similar and a typical example is shown in Fig(4.8). This particular spectrum was recorded from the powder with the Cr concentration of 530 ppm. The field values of the features at  $H = 212mT$  (with strong, narrow positive peak),  $H = 532.01 mT$  (with medium, wide, positive and negative peak) and  $H = 640.0 mT$  (medium, narrow, negative peak) were noted.

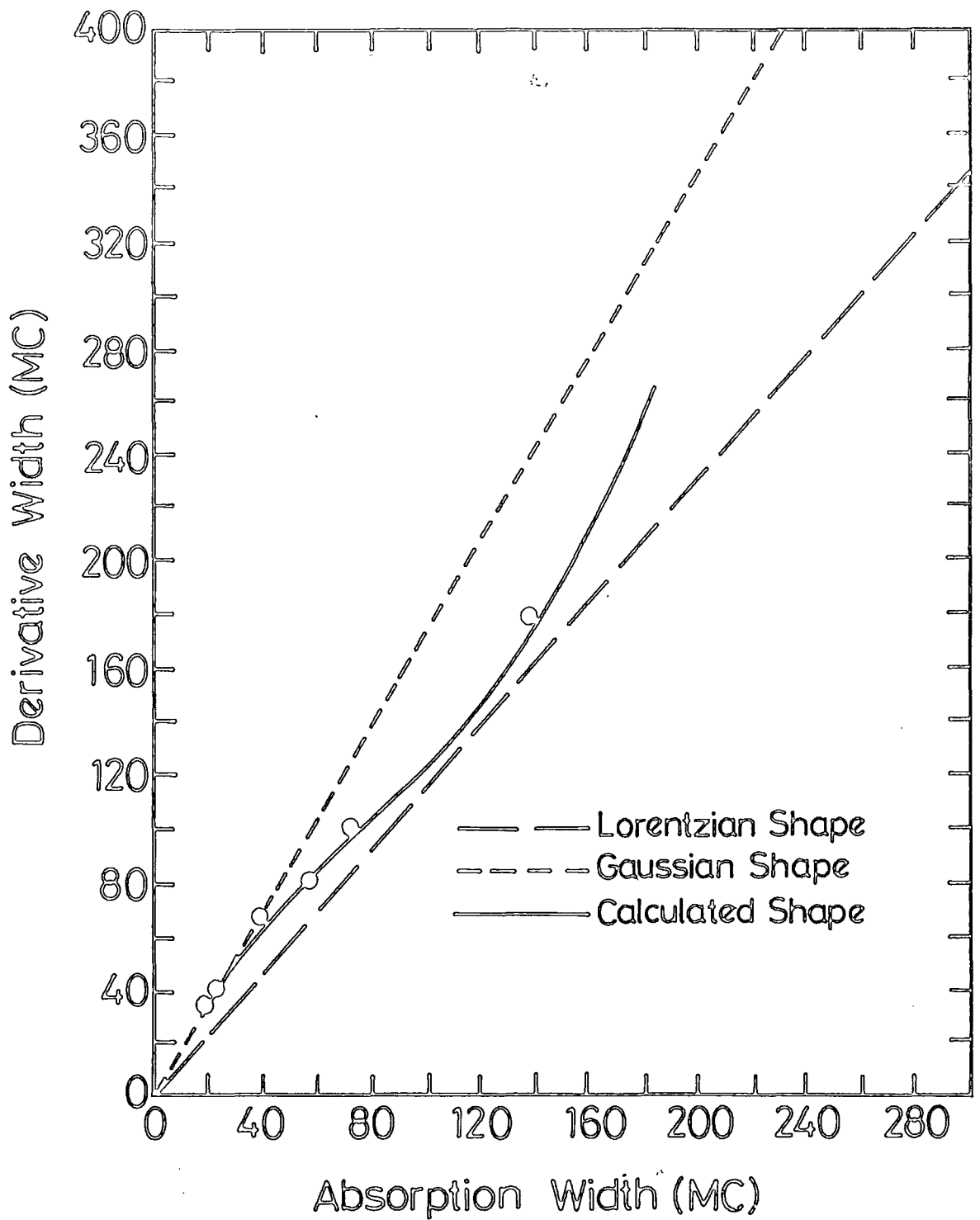


Fig. (4.7) Half-Linewidth and derivative width ( $\frac{1}{2} \leftrightarrow -\frac{1}{2}$ ) transition,  $\theta = 0^\circ$

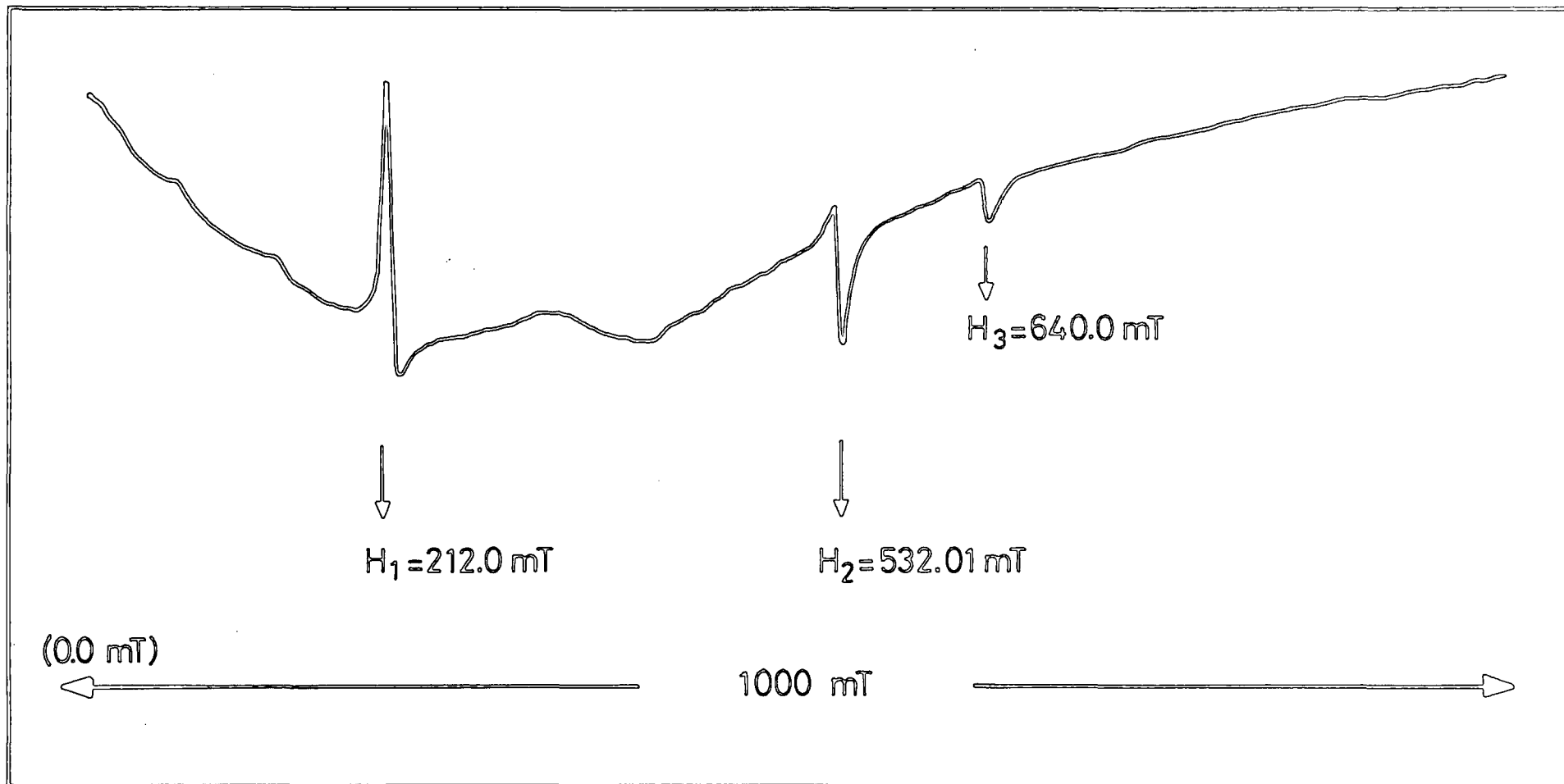


Fig. (4.8) Experimental E.P.R. spectrum of powdered  $\text{Cr}^{3+}/\text{Al}_2\text{O}_3$ ; 530 p.p.m. Cr, 9.486 GHz, 293K.

The  $Cr^{3+}$  spectra obtained from the powder samples were analysed using exactly the same procedures as for the single crystals samples (see Section 4.2). For the 530 ppm Cr concentration the values for  $g$  and the linewidth are 3.17 and 3.41mT respectively. The powder contains crystallites orientated at random. The number of ions for which the magnetic field makes an angle between  $\theta$  and  $(\theta + d\theta)$  is proportional to  $Sin\theta d\theta$  and, since the spectrum is not affected by several of the magnetic fields, we may consider the range of angles to lie between 0 and  $\frac{\pi}{2}$ , then, the factor of proportionality will be unity. The spectrum of any ion that is anisotropic will naturally be spread out and the information for the spectrum reduced. Because all the lines in the single crystal are anisotropic, there is no direct correspondence between the field values of the powder feature and those of the single crystal.

The paramagnetic property of the powder form is a result of  $Cr^{3+}$  displacing  $Al^{3+}$  in the lattice of corundum. There are  $5.7 \times 0.5\% = 2.85$  atoms of chromium per unit cell where 5.7 is the number of Al atoms per unit cell, and 0.05 unit cells can be found from the volume, and using some calculation, we found the number of chromium atoms is  $18.35 \times 10^3$  for the weight of 0.0752 gms of powdered single crystal.

#### 4.6 Computer simulation of powder spectrum

Computer simulations of the powder spectra of  $Cr^{3+}$  in Al sites in  $Al_2O_3$  were

tonian and the simulation of it from the observed single crystal data has been written, and the results were computed.

The idea of the simulation is that in the powder the crystallites are randomly orientated and selecting the  $\theta$  and  $d\theta$  in this way would give a true simulation. The  $g$  values corresponding to  $\phi$  and  $\text{Sin}\theta$  were calculated and the related values of the resonant field were found. An array was set up for each element covering the whole field range, and the array element incremented each time that the resonant field occurred. This was performed for both constants, and by adding a different amount to the array for each transition, the effect of differing transitions could be simulated. The line was broadened and differentiated for comparison with the experiment. At any given dopant concentration the spectra predicted by the various methods were identical and typical examples of the simulation obtained for the powders containing 530 ppm chromium are shown in Fig (4.9). The variables in the simulation procedure are the crystal field parameters ( $A$  and  $g$ ), the microwave frequency, the lineshape function and the linewidth. At any given dopant concentration, the powder spectrum was simulated using Lorentzian and Gaussian lineshape functions whose peak-to-peak linewidth corresponded to that of the central transition in the single crystal spectrum of the sample doped at the same level ( $\Delta H_{ms}$  in Table 4.1). A Gaussian lineshape function was chosen for the purpose of the simulation because the experimental central transition in the single crystal spectrum at 530 ppm showed

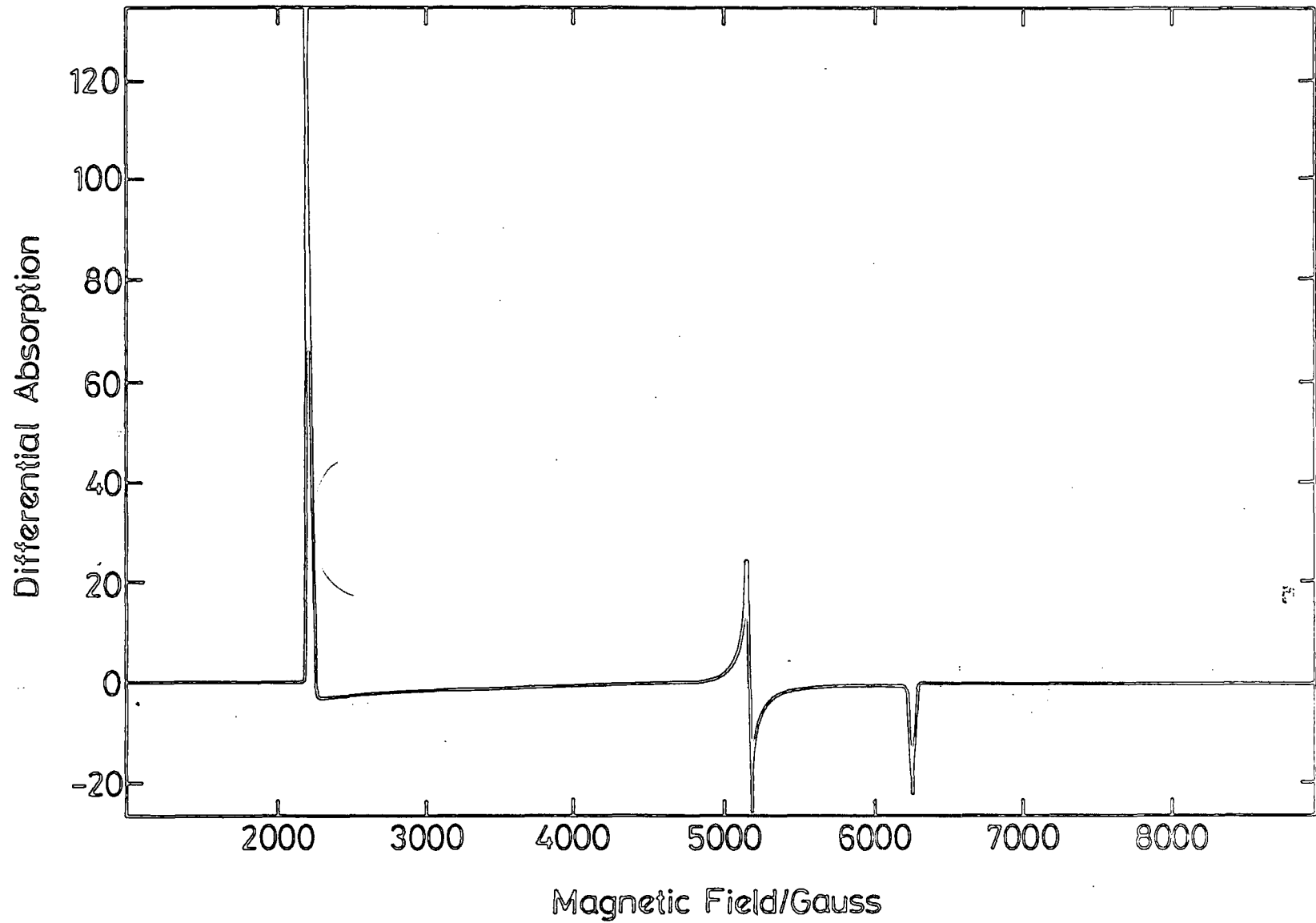


Fig. (4.9) Computer Simulation powder spectrum for  $\text{Cr}^{3+}/\text{Al}_2\text{O}_3$  using single crystal data

that it has this shape. The values of A and g determined experimentally from the single crystal spectrum at a particular dopant concentration were used to simulate the powder spectrum at the same dopant concentration. At any given doping level, the powder spectrum was simulated at the microwave frequency used to record the experimental powder spectrum so that the field positions of spectral lines in the simulated and experimental powder spectra could be directly compared. Thus, the powder spectra of the five specimens examined were simulated at the microwave frequency 9.502 GHz.

Since the single crystal parameters were used in the simulation procedure and the  $Cr^{3+}$  spectrum is anisotropic, the computed powder spectrum will not be identical to the experimental single crystal spectrum. It should be identical to the experimental powder spectrum at the same dopant concentration (except that the magnetic field values at which the transition occur will be shifted a little to those appropriate for the microwave frequency). The g values and the linewidth between points of maximum slope were determined from the computed spectrum and it was found that they agreed well with corresponding values at all dopant concentrations.

## 4.7 Theory and discussion of the powder linewidth

### 4.7.1 Van Vleck Linewidth

The dipolar linewidth for the powder has been given by Van Vleck [4.15] and his description takes the form

$$\langle \Delta\nu^2 \rangle = \frac{3}{5} \frac{g^4 \beta^4}{\hbar} S(S+1)n \sum_k r_{jk}^{-6}$$

where the powers of the direction cosines in equation (2.17) are replaced by their averages over a sphere. The linewidth for the feature at  $H = 212 \text{ mT}$  has been calculated for the concentration of 530 ppm using the  $g$  value obtained from the powder spectrum and has the value

$$\Delta H_{ms} = 14.93 \text{ mT}$$

which is some five times greater than the experimentally observed width of 3.14mT.

### 4.7.2 Kittel and Abrahams' Linewidth

The Kittel and Abraham linewidth for the powder form has been shown in Chapter 2 (Section 2.3.2). For the concentration of 530 ppm, the calculated linewidth again

for the same feature at  $H = 212 \text{ mT}$  using equation (2.33) gives

$$\Delta H_{ms} = 6.29 \text{ mT}$$

This result gives reasonable agreement with the observed linewidth and is less than that predicted by the Van Vleck model.

#### 4.7.3 de Baisi and Fernandes' Model

The term  $C_1$  in equation (2.39) (the function of the total concentration of the paramagnetic ion, the range of the exchange interaction and the lattice geometry) was calculated using the same values of the constants  $g$ ,  $a$  and  $S$  and the same methods as those which were employed to determine the linewidth for  $n = 1$  to  $n = 4$  in the single crystal (see Section 4.3). These theoretical linewidths were  $9.13 \times 10^{-2} \text{ mT}$  for  $n = 1$  and  $2.62 \times 10^{-5} \text{ mT}$  for  $n=4$ . The experimental values of linewidth do not agree with any of the theoretical values. This discrepancy between theory and experimental is not due to broadening of the lines nor is it likely to be due to strain. The disagreement between the linewidths predicted by de Biasi and Fernandes' model and those observed experimentally for  $(1/2 \leftrightarrow -1/2)$  transitions of the powders is probably due to the fact that the model only holds in the absence of fine structure of the spin energy level . Therefore it can only be

directly applied to ions with  $s < 2$

in cubic symmetry and the ions with  $S = 1/2$  in any other symmetry. Hence, in the  $Cr^{3+}/Al_2O_3$  powders examined, de Biasi and Fernandes' theoretical results are not, strictly speaking applicable to this system, as  $Cr^{3+}$  has a spin,  $S$ , of  $3/2$  in tetragonal symmetry.

## REFERENCES

- 4.1 T. Maiman, *Nature*, 187, 493 (1960).
- 4.2 R.W. Wyckoff, 1931, *The Structure of Crystals* (Interscience, New York, 1957).
- 4.3 S. Sugano and Y. Tanabe, *J. Phys. Soc.*, Japan, 13, 880 (1958).
- 4.4 S. Sugano and I. Tsujikawa, *J. Phys. Soc.*, Japan, 13, 899 (1958).
- 4.5 D.J. Howarth, *R.R.E. Memorandum*, No 1498 ( Oct 1958).
- 4.6 D.J. Howarth, *R.R.E. Memorandum*, No 1767 (April 1960).
- 4.7 W. Low, *Paramagnetic Resonance* (Volume I, page 156) Academic Press, New York, London. (1963).
- 4.8 J.E. Geusic, *Phys. Rev.* 102, 1252 (1956).
- 4.9 W.J. Grant and M.W. P. Strandberg, *Phys. Rev.* 135 A, 727 (1964).
- 4.10 C.F. Davis and M.W.P. Strandberg *Phys. Rev.* 105, 447, (1957).
- 4.11 E.O. Schulz-Dubois, *Bell Syst. Tech. Journal.* 38, 271 (1959).
- 4.12 A.A. Manenkov and A.M. Prokhorov, *Soviet Physics, JETP.* 4, 228 (1957).

- 4.13 H. Low, *Phys. Rev.* 105, 801 (1957).
- 4.14 C.P. Poole, "*A Comprehensive Treatise on E.S.R. Experimental Technique*". Inter Science, N.Y.(1967)
- 4.15 J.H. Van Vleck, *Phys. Rev.* 74 1168 (1948).
- 4.16 C. Kittel and E. Abrahams, *Phys. Rev.* 90, 238 (1953).
- 4.17 R.S. de Biasi and A.A.R. Fernandes, *J. Phys. C.* 16. 5841 (1983).
- 4.18 A.A. Manenkov and V.B. Prokhorov *J.E.T.P.* 11, 527 (1960).
- 4.19 J.S. Thorp, H.P. Buckley, *J. Mater. Sci.*, 9, 1499. (197 ).

## CHAPTER FIVE

### E.P.R. STUDIES OF IRON IN ALUMINIUM OXIDE SINGLE

#### CRYSTAL AND POWDER

##### 5.1. Introduction

The crystal structure of aluminium oxide has been described previously in this thesis. In  $Al_2O_3$  doped with ferric ions the ferric ions replace the aluminium ion isomorphously in the crystalline lattice of corundum. There are two nonequivalent sites, differing in the direction of the cubic axis of the crystalline field, which exhibit trigonal symmetry about the c-axis, Howarth and Hensman [5.1]. The electronic configuration of the unfilled shell is 3d with an  $s^6$  ground state. The crystal field in  $Al_2O_3$  at the Fe site is trigonal ( $C_{3v}$ ). The splitting of the  $s^6$  ground state has been studied by Kornienko and Prokhorov [5.2] and Bogle and Symmons [5.3]. The splitting of the ground state levels as a function of magnetic field together with the observable transitions are shown in Fig(5.1). The paramagnetic resonance for  $Fe^{3+}/Al_2O_3$  as a single crystal has been reported fairly extensively in the literature, [5.1 - 5.6]. and can be interpreted by a Spin Hamiltonian which takes the form [5.1].

$$\mathcal{H} = g\beta H.S + D(S_z^2 - \frac{35}{12}) + \frac{1}{6}a(S^4 + S + S^4 - \frac{707}{16}) + \frac{7}{36}F[S_z^4 - \frac{95}{14}S_z^2 + \frac{18}{16}] \quad 5.1$$

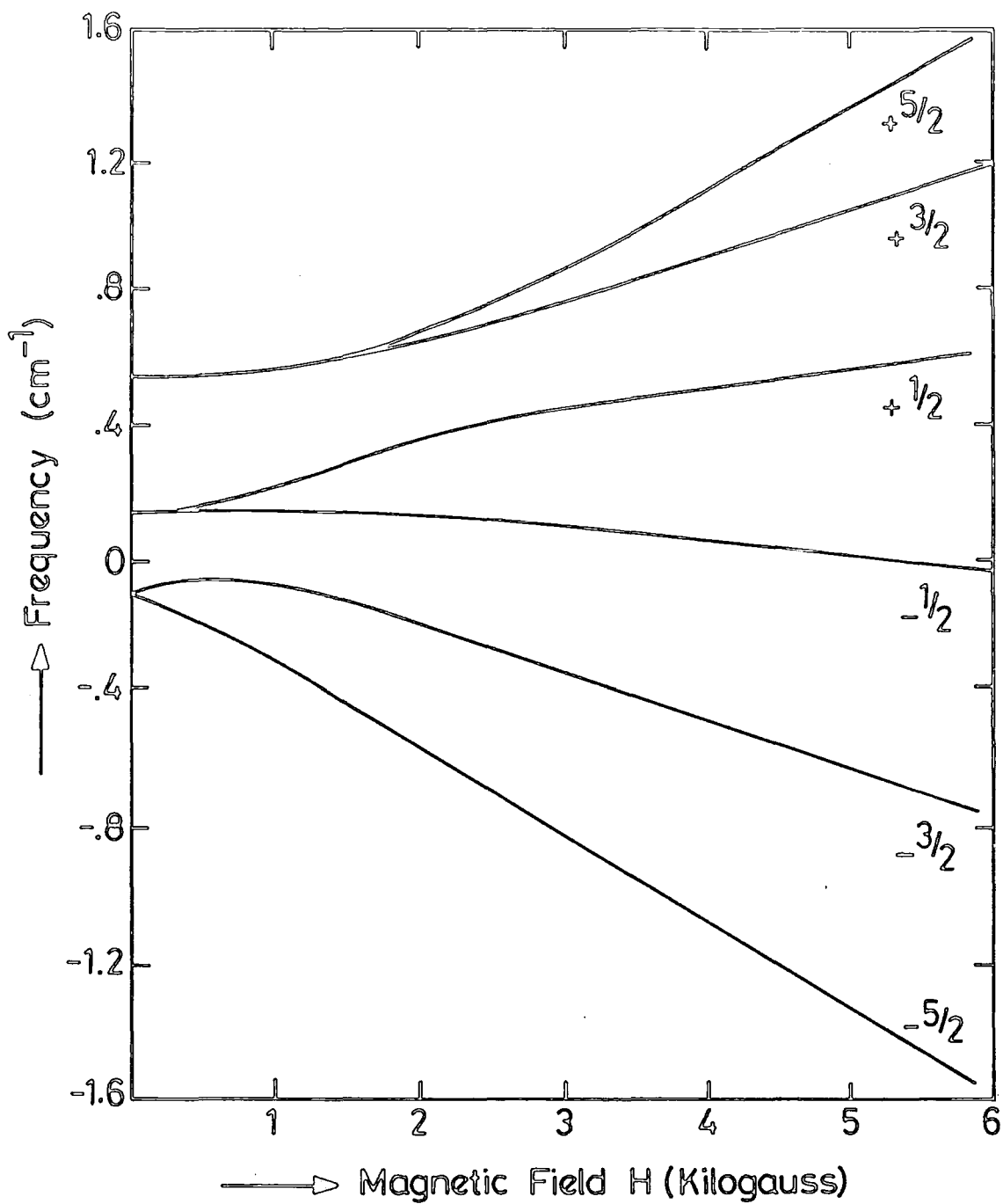


Fig. (5.1) Energy level diagram of Fe<sup>3+</sup> in Al<sub>2</sub>O<sub>3</sub>, with the magnetic field perpendicular to the C-axis

Kornienko and Prokhorov reported the  $g$  value equal to  $(2.003 \pm 0.001)$  and Howarth reported a similar  $g$  value (2.003). The Spin Hamiltonian coefficient  $D$  has the value  $(1684 \pm 3 \times 10^{-4} \text{cm}^{-1})$  and the cubic lattice constant has the value  $|a| = (262 \pm 2 \times 10^{-4} \text{cm}^{-1})$  [5.3] The crystal field splitting of the ground state is caused by the trigonal field along the  $C$ -axis There are also cubic field components whose axes with respect to the  $C$ -axis lies in the  $[\bar{1}11]$  direction; these cubic fields lie in the a-c crystallographic plane.

In this Chapter, a description is given of the experimental and theoretical examination of the 9.5GHz electron paramagnetic resonance spectra which have been studied for  $Fe^{3+}/Al_2O_3$  on both the single crystal and powder forms with 1000 ppm Fe concentration. All the data was obtained at room temperature.

## 5.2 Experimental results of $Fe^{3+}/Al_2O_3$ single crystals

The E.P.R. spectrum of  $Fe^{3+}/Al_2O_3$  was recorded on the Varian V4205-12 spectrometer at room temperature, with the magnetic field perpendicular to the  $C$ -axis. More details of the technique can be found in several E.S.R. text books, an example of which is "A Comprehensive Treatise on E.S.R. Experimental Technique" by Poole [5.7] The sample was examined using the X-ray fluorescence technique, which confirmed that the concentration of the iron dopant was 1000 ppm.

The E.P.R. spectrum illustrated in Fig (5.2) was obtained from the sample at  $\theta = 0$ . The  $g$  value of the line is about 2.004 which is the same as the reported value for the  $(1/2 \leftrightarrow -1/2)$  transition in [5.2] Measurements of the magnetic field values at resonance and linewidth determinations were made as functions of the polar angle. There is no change in the resonance field with the polar angle. The linewidth defined as the width between point of maximum slope,  $\Delta H_{ms}$ , was obtained directly from the E.P.R. spectrum. The measured linewidth was about 1.35 mT which was independent of the polar angle as shown in Fig (5.3).

### 5.3. Theoretical calculation for $Fe^{3+}/Al_2O_3$ single crystal

#### 5.3.1 Van Vleck dipolar broadening theory [5.8]

One needs the equation for dipolar broadening between like atoms, in order to calculate the linewidth caused by dipolar interaction between the  $Fe^{3+}$  ions in the aluminium oxide lattice. For  $Fe^{3+}$ ,  $S = 5/2$  and in the  $Al_2O_3$  lattice the  $g$  value is 1.987. The atomic part of equation (2.22 Chapter2) , can be evaluated as

$$\frac{3}{4}S(S+1)(g^2\beta^2/\hbar)^2.n = 1.256.n \times 10^{-24}(rad.sec^{-1})cm^{-6} \quad 5.2$$

Using Table II of reference [5.9], the geometrical part of equation (2.22) can be partially simplified leading to the final equation for the second moment for like

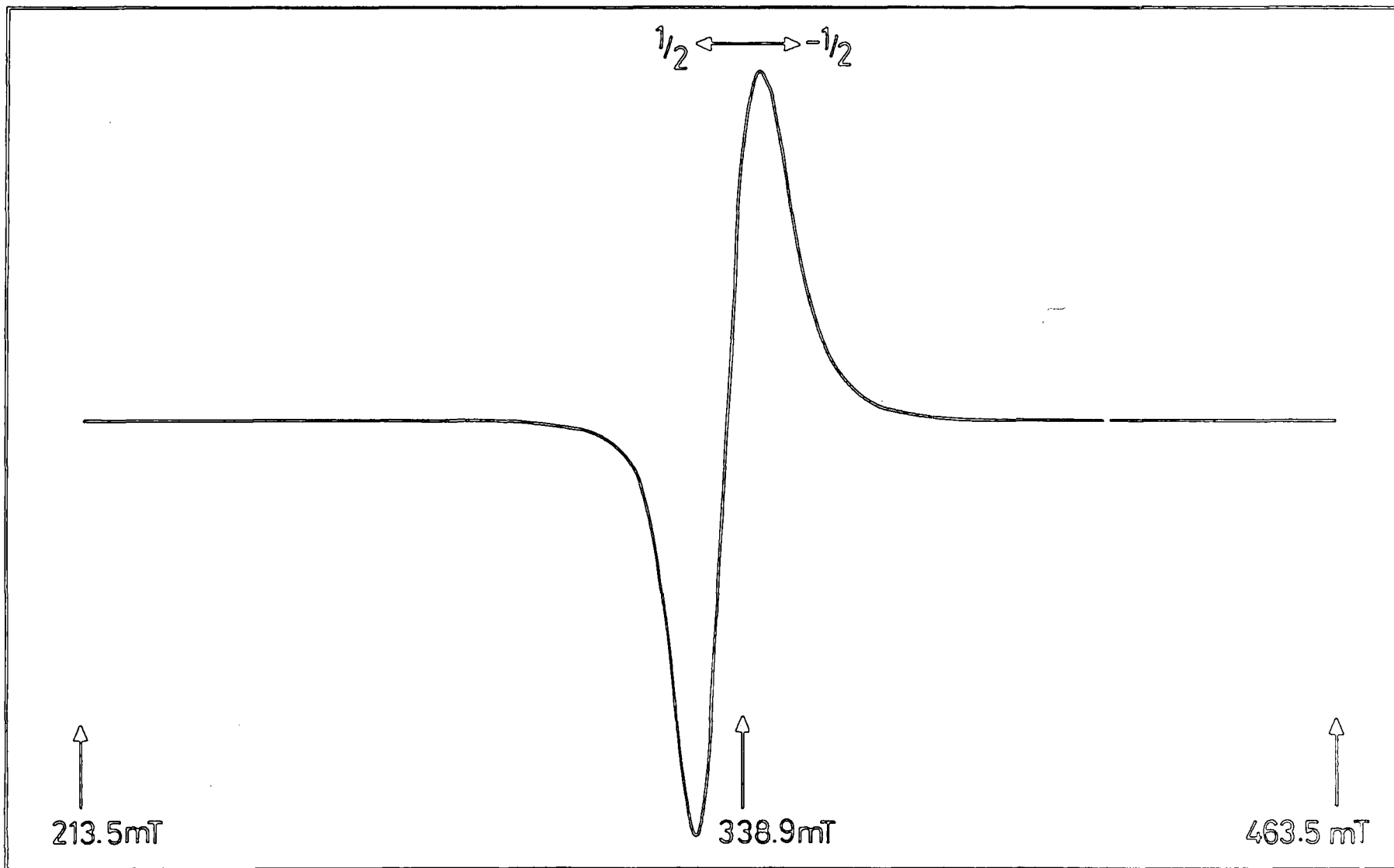


Fig. (5.2) E.P.R. spectrum of single crystal  $\text{Fe}^{3+}/\text{Al}_2\text{O}_3$ ; 1000 p.p.m. Fe,  $293\text{K} = \theta_{\text{H}} = 0$ , 9.502 GHz

atoms. For  $Fe^{3+}/Al_2O_3$ , this becomes

$$\begin{aligned} \langle \Delta\nu^2 \rangle = & 1.256 \times 10^{-24} \cdot n \times 10^{45} [12.847 \\ & + 0.185Y_{2,0}^*(\theta_H, \phi_H) + 4.878Y_{4,0}^*(\theta_H, \phi_H) \\ & - 4.025Y_{4,3}^*(\theta_H, \phi_H) + 4.025Y_{4,-3}^*(\theta_H, \phi_H)] \quad 5.3 \end{aligned}$$

Using the transformation equation (2.25), and considering the peak to peak derivative, the linewidths have been calculated. The theoretical curves for the variation of the linewidth with the polar angle are given in Fig.(5.3); this theoretical curve applies for a concentration of 1000 ppm Fe, so that the theoretical and experimental plots are directly comparable.

A similar calculation was made in order to assess the magnitude of contributions to the linewidth due to dipolar interaction between unlike atoms. In this instance the Fe-Al interaction must be considered. As previously explained in the earlier Chapters for both the Gd-Al and the Cr-Al interactions, the effect is very small. The magnitude of the Fe-Al interaction is comparable and therefore, its contribution can also be neglected.

### 5.3.2 Kittel and Abrahams' Model [5.10]

The calculation of the dipolar linewidth on Kittel and Abrahams' model follows the

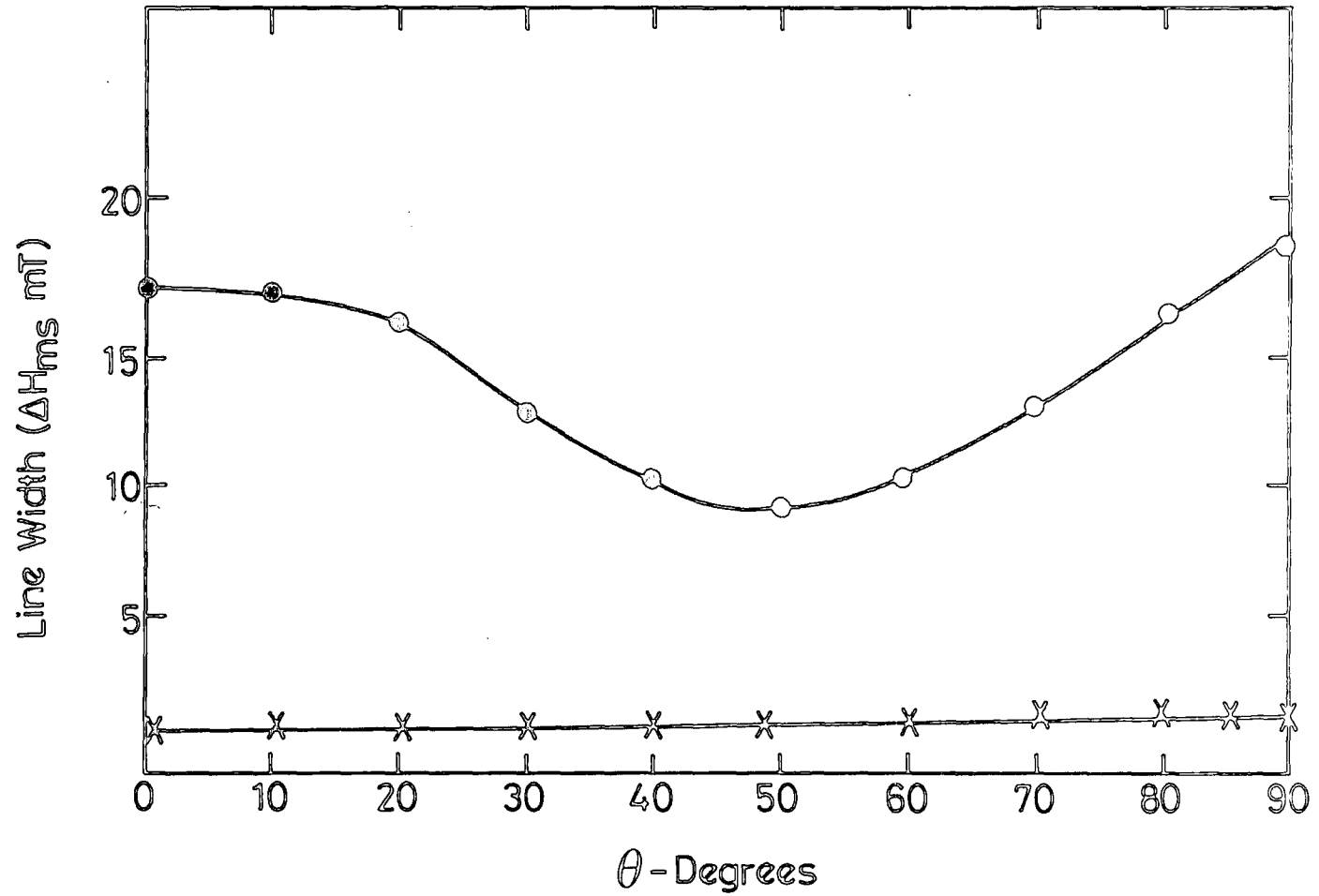


Fig. (5.3) Experimental and Theoretical angular Variation of Linewidth  
 X Experimental  
 o Theoretical

procedure described in Chapter 3. There is a difference in the atomic part and in the spins and the effect of these changes is to give a linewidth of

$$\Delta H_{ms} = 2.17mT$$

for the concentration of 1000ppm.

#### 5.4 Discussion of single crystal results

The analysis of the linewidth data showed that the values predicted on the basis of Van Vleck dipolar theory for 1000ppm Fe concentration are about nine times larger than the observed linewidth. On the other hand, the calculation of the linewidth using the Kittel and Abrahams' model agreed reasonably well with the observed linewidth for the known concentration. It is important to note that there is close agreement between our linewidth result based on Kittel and Abrahams' theory and the similar work done by Bogle [5.3], for the same concentration of iron.

The evidence indicated that any contribution from exchange interaction is extremely small. The comparison of the experimental data with theory showed that dipolar broadening mechanisms were present and were indeed the dominating factors affecting the linewidth. This result is remarkably similar to that encountered with both  $Gd^{3+}/Al_2O_3$  and  $Cr^{3+}/Al_2O_3$ . Thus in all these systems, i.e.

$Gd^{3+}/Al_2O_3$ ,  $Cr^{3+}/Al_2O_3$  and  $Fe^{3+}/Al_2O_3$  it is found that the Kittel and Abrahams' dipolar broadening theory is quite adequate to explain the experimental linewidth observations. The earlier Van Vleck dipolar broadening model does give an order of magnitude fit for the experimental linewidths in these three materials, but the agreement is not so close as with Kittel and Abrahams' more refined model.

### 5.5 Characterisation of the E.P.R. spectrum of the $Fe^{3+}/Al_2O_3$ Powder Sample

The powder was prepared from single crystal and was obtained by grinding a small amount of single crystal using a Glen Creaston tungsten carbide ball mill. The spectrum was recorded from the powder sample on the Varian V4205-15 E.S.R. Spectrometer at room temperature and is shown in Fig. (5.4). The field value for the feature is  $H = 339\text{mT}$  (with positive and negative peak). The  $Fe^{3+}$  spectrum obtained from the powder sample was analysed using similar procedures to those previously employed for the single crystal sample (see section 5.2). The values obtained for  $g$  and the linewidth  $\Delta H$  were 2.002 and 2.17 mT respectively.

Since the E.P.R. line ( $1/2 \leftrightarrow -1/2$ ) in the single crystal is isotropic, there is direct correspondence between the field value of the powder feature and of the single crystal. The resulting spectrum found experimentally for the powder shows only one line which has the same field value as the ( $1/2 \leftrightarrow -1/2$ ) single crystal line; therefore,

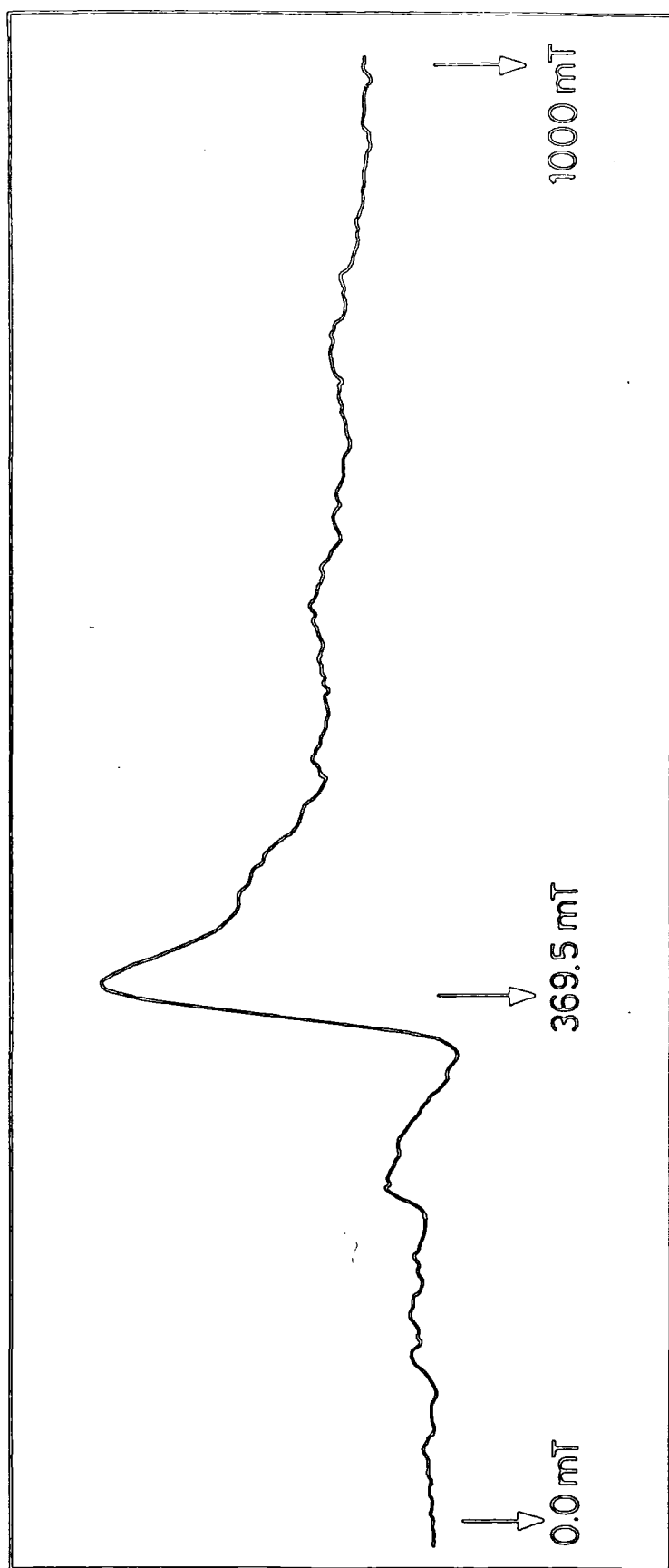


Fig. (5.4) Experimental E.P.R. spectrum of powdered  $\text{Fe}^{3+}/\text{Al}_2\text{O}_3$   
; 1000 p.p.m  $\text{Fe}^{3+}$ , 9.502GHz, 293K.

the observed powder line may be identified with the line observed in the single crystal, which corresponds to the  $(1/2 \leftrightarrow -1/2)$  transition. Computer simulation of the powder spectrum of  $Fe^{3+}$  in  $Al_2O_3$  was undertaken. The features which are present in the experimental results are not seen in the simulated powder spectrum which only displays the  $(1/2 \leftrightarrow -1/2)$  line and only this transition was indicated in the simulation procedure undertaken. The calculation of the powder spectrum from the Spin Hamiltonian has been completed, using the observed single crystal data. The simulated spectrum was derived using similar procedures and ideas as for  $Cr^{3+}/Al_2O_3$  (see Chapter 4). Computer methods for the simulation of powder spectra have also been reported for a number of different materials. Most methods used in predicting such spectra have a common starting point. A selection of these methods is given in the references [5.11 - 5.16].

The spectrum predicted is shown in Fig(5.5). The variables in the simulation are the crystal field parameters ( $A$  and  $g$ ), the microwave frequency, the lineshape functions and the linewidth. At 1000ppm dopant concentration, the powder spectrum was simulated using both Lorentzian and Gaussian lineshape functions whose peak-to-peak linewidth corresponded to that of the central transition in the single crystal spectrum. Of the two, the Gaussian lineshape function is likely to be more suitable for the purpose of the simulation because analysis of the central transition in the experimental single crystal  $Fe^{3+}$  spectrum showed that it has this lineshape. Since

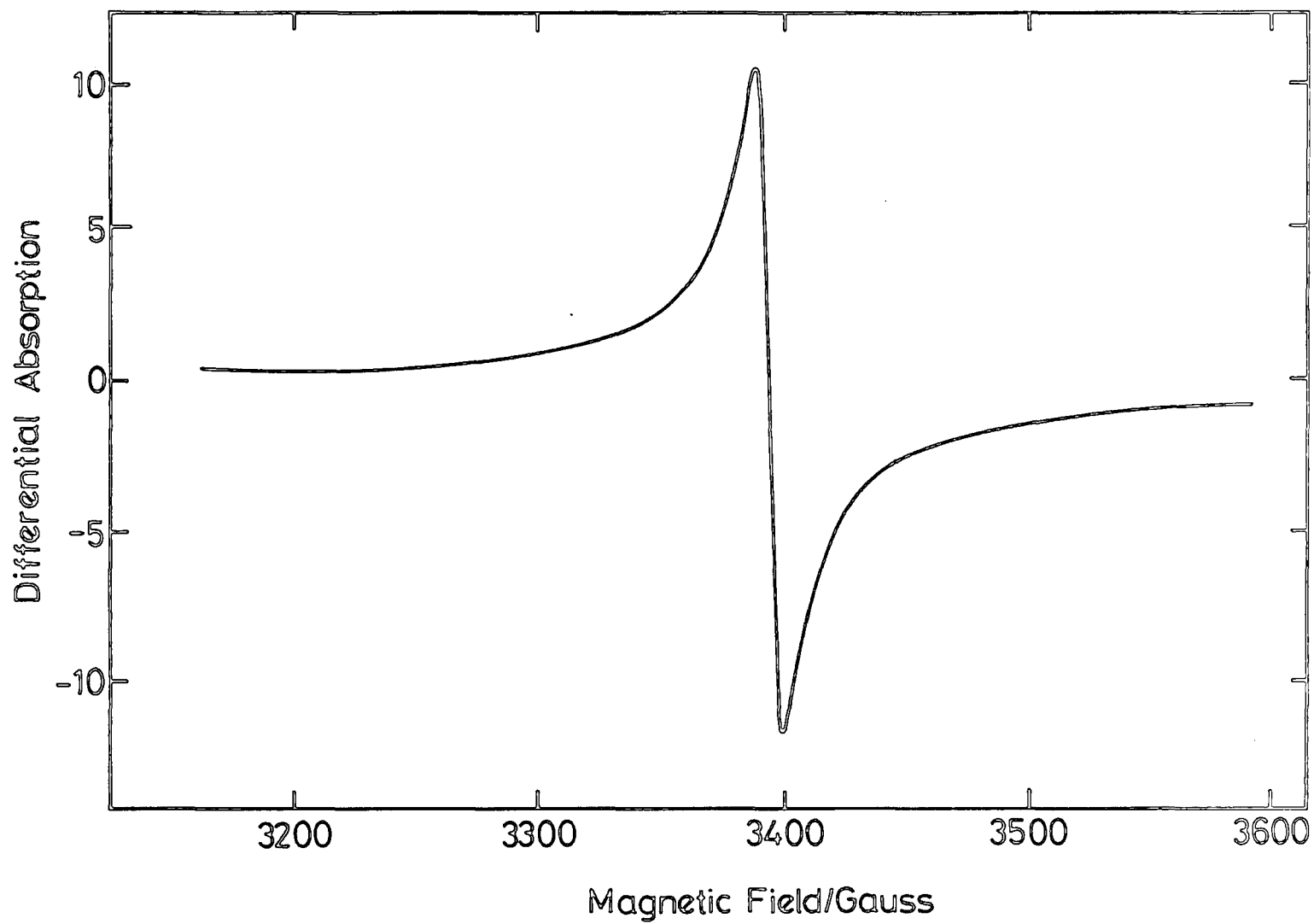


Fig. (5.5) Computer simulation powder spectrum for  $\text{Fe}^{3+}/\text{Al}_2\text{O}_3$  using single crystal data

the single crystal parameters were used in the simulation procedure and because the  $Fe^{3+}$  spectrum is isotropic, the computed powder spectrum will be identical to the experimental single crystal spectrum. The  $g$  value and the linewidth were determined from the computed spectrum and have the values 1.996 and 1.67mT respectively.

The agreement between the experimental powder spectra and that simulated for  $Fe^{3+}$  ion in  $Al_2O_3$  provides and confirms evidence that the experimental powder spectrum is due to the  $Fe^{3+}$  ion in the  $Al_2O_3$  lattice symmetry.

The theoretical linewidths were calculated for both Van Vleck's dipolar theory and Kittel and Abrahams' model, following the same methods described in Chapter 4. The difference here is that  $Fe^{3+}$  has the spin  $S = 5/2$  and the  $g$  value was taken from the experimental powder spectrum of  $Fe^{3+}$  in  $Al_2O_3$ . As has been explained before and from our result, Kittel and Abrahams' model produces a very satisfactory value of  $\Delta H_{ms} = 8.193mT$  for the concentration of 1000ppm, whereas the Van Vleck model predicts 22.79 mT.

## REFERENCES

- 5.1 D.J. Howarth and R. Hensman, *R.R.E. Memorandum*, No 1707, April (1960).
- 5.2 L.S. Kornienko and A.M. Prokhorov, *Soviet Physics. JETP*, 6,620 (1959).
- 5.3 G.S. Bogle and H.F. Symmons, *Proc. Phys. So*, 73, 531, (1959).
- 5.4 L.S. Kornienko and A.M. Prokhorov, *Soviet Physics. JETP*, 40, 1594, (1961).
- 5.5 H.F. Symmons and G.S. Bogle, *Proc. Phys. Soc.* 79, 468 (1961).
- 5.6 B. Bleaney and R.S. Trenan, *Proc. Roy. Soc.* A223, 1 (1954).
- 5.7 C.P. Poole "A Comprehensive Treatise on E.S.R. Experimental Technique". Inter Science, N.Y.(1967)
- 5.8 J.H. Van Vleck, *Phys. Rev.* 74, 1168 (1948).
- 5.9 J.S. Thorp, H.P. Buckley, *J. Mater, Sci.*, 9, 1499 (1976).
- 5.10 C. Kittel and E. Abrahams, *Phys. Rev.*90, 238 (1953).
- 5.11 R.H. Sands. *Phys. Rev.* 99, 1222 (1955).
- 5.12 P.C. Taylor and P.J. Bray, *J. Mag. Res.* 2,305 (1970).

- 5.13 W. Hutton "*The Role of Titania in The Formation of Mg - Al<sub>2</sub>O<sub>3</sub> - SiO<sub>2</sub> glass ceramics*". Ph.D. Thesis, Durham University (1980).
- 5.14 V. Beltran-Lopez and J. Castro-Tello. *J. Mag. Res.*, 39, 437 (1980).
- 5.15 F.K. Kneuhubl. *J. Chem. Phys.*, 23, 1074 (1960).
- 5.16 A.R. Skinner, "*Electron Paramagnetic Resonance in Some 3d Ions in MgO*". Ph.D. Thesis, Durham University (1986).

PART II

Electron Spin Resonance and Related Studies

on

Aluminium Nitride

## CHAPTER SIX

### EXPERIMENTAL TECHNIQUES

#### 6.1 X-Ray Techniques

The first stage of the investigation of the structure and composition of the four different samples of aluminium nitride, (AlN), was by X-ray powder photographs. Copper  $K\alpha$  radiation was used. From these powder spectra the  $d$  values and the unit cell parameters were derived for all the samples and were compared with the A.S.T.M. index cards.

For the second stage a X-ray diffractometer (a PW 1130 Philips 3 kilowatt equipment) was used. Copper  $K\alpha$  radiation was used with a nickel filter; the counter was a sealed proportional type and was moved at the rate of between  $1^{\circ}$  to  $20^{\circ}$  per minute. The result for each as sample, which was obtained as a chart recording, was labelled using the index cards so as to identify the lines due to AlN and hence establish whether impurity lines were also present.

The X-ray fluorescence technique was employed in order to make an elemental analysis of the impurity contents. A PW 1400 Philips X-ray spectrometer with a rhodium X-ray tube was available. This used a LiF analysis crystal, (220) planes, and had both scintillation and flow counter detectors .

## 6.2 S.E.M. and E.D.A.X. Technique

The Cambridge Stereoscan 600 Scanning Electron Microscope (S.E.M) was used to obtain microstructural information. The processed data was presented as a plot of the variation of X-ray intensity with X-ray energy; this plot is the E.D.A.X. (Energy Dispersive Analysis by X-ray) trace, which can be taken from small, selected areas of the sample. The spectra of the AlN samples were obtained at different positions on each sample.

The AlN samples were prepared by placing some of the powder on an adhesive tape on a metal mount. It was found that charging effects caused by the electron beam hitting the insulating particles caused the image to be distorted, so that a layer of gold was sputtered onto the samples to conduct this charge away.

## 6.3 Electron Spin Resonance

The E.S.R. spectra of the AlN samples were recorded on the Varian 4205-12 Spectrometer at room temperature, liquid nitrogen and liquid helium temperatures. The temperature controller V-4540 was used which maintained the nitrogen at a preselected temperature. For temperatures in the range 90K - ambient the dry nitrogen was first cooled by passing it through a heat exchanger comprising a coiled copper tube, immersed in liquid nitrogen, from which it emerged at a temperature of about 80K. Control of the gas flow-rate and the heater current enabled control of

the sample temperature, which was monitored with a copper constantan thermocouple placed in the cavity adjacent to the sample. As the quartz insert did not provide very efficient insulation it was necessary when operating at temperatures below ambient to continuously flush the cavity with a stream of dry nitrogen gas, to prevent water condensing in the cavity.

Temperatures in the range 20K - 90K were obtained with an Oxford Instruments ESR9 Continuous Flow Cryostat, in conjunction with a DTC-2 Temperature Controller. Liquid helium was continuously supplied from a storage dewar, via a flexible transfer tube comprising two concentric stainless steel tubes, surrounded by a vacuum jacket. It then passed through a stainless steel capillary tube in the cryostat, emerging just below the cavity as a stream directed onto the sample. The capillary, sample holder and sample were all located within a dewar which was sealed at the top. After cooling the sample the helium (gas) returned up an outer layer of the transfer tube, thus assisting in cooling the incoming liquid. Coarse temperature control was achieved by regulating the flow of helium. For fine adjustment and automatic control a copper heat exchanger surrounding the tip of the stainless steel capillary was heated, via the temperature control unit. The detailed procedure has been described in the Varian literature [6.1].

#### 6.4 Gouy Balance Technique

In the Gouy balance technique Fig.(6.1) the furnace is placed between the poles of the magnet with its centre at the pole axis, Crangle [6.2] and Williams et al [6.3]. The substance in powder form is placed in a glass tube suspended in the furnace from a sensitive balance in such a way that the base of the tube is at the centre of the furnace. When the electromagnet is switched on, the sample becomes magnetized and creates a force in the regions of the field gradient moving towards the centre of the field. The maximum field used here was 360 mT which corresponded to a current of 7 amperes. A water-cooling system is provided on the magnet to permit operation at high currents. The range of the furnace used goes up to  $1000^{\circ}C$ . For accurate measurements, a wooden shield was made to surround the magnet and the furnace to reduce the ambient draughts; this proved to be helpful in reducing stray fluctuation in effective weight. A digital monitor is used for accurate reading of the temperature. The length of the powder column should be such that it does not exceed the limits of the furnace's uniform region. This was found to be 5 cm. The forces measured are small ( a few milligrams)and therefore a high sensitivity is required in the force measurement. A special balance is necessary for the measurement of such low forces. The order of accuracy also depends upon the uniformity of packing in the glass tube, so a very finely ground powder is necessary. Besides that, a thin specimen is needed to make negligible all

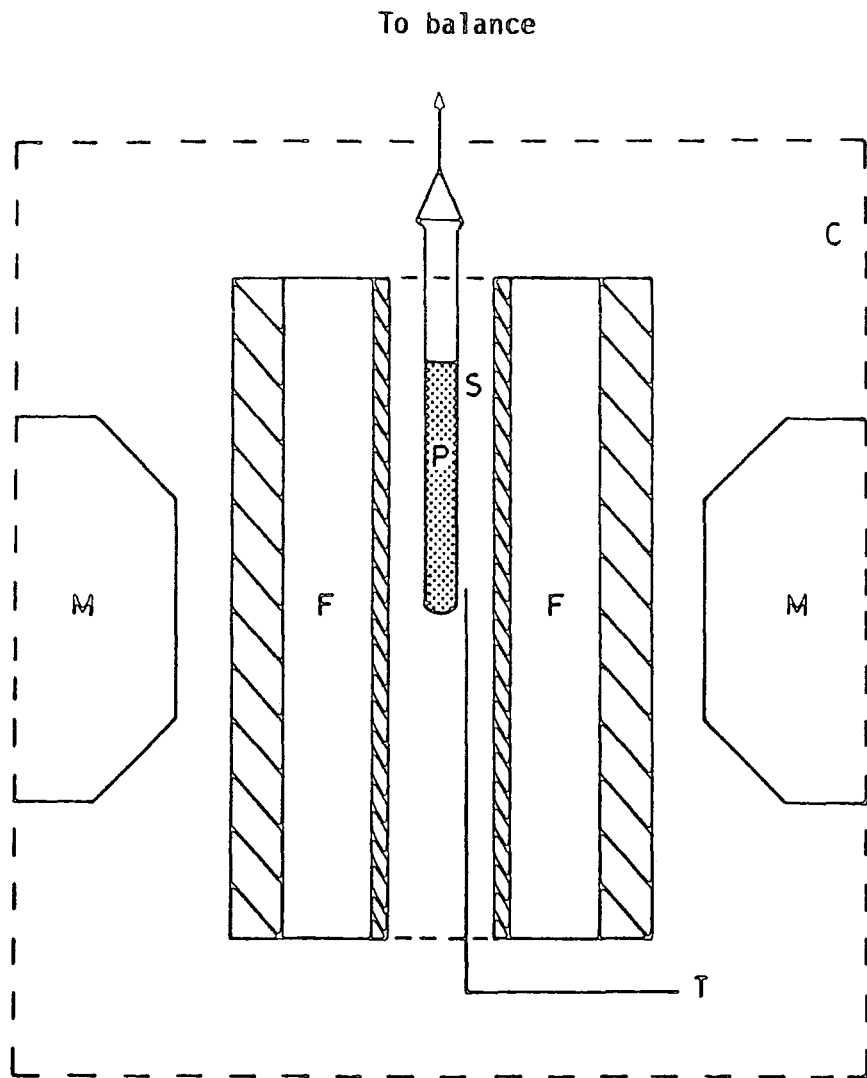


Fig. (6.1) Schematic arrangement of modified Gouy balance. (M, electromagnet; F, furnace; T, thermocouple and temperature controller; S, silica specimen tube; P, specimen; C, cover.

the force components other than the vertical force. Measuring the force before and after the magnet is switched on, and making allowances in the calculation for the force experienced by glass, the net force due to magnetization can be determined. This force (F) exerted on a sample having a volume susceptibility( $\chi$ ) was derived from the relation ,Thorp.at.el [6.4].

$$F = \frac{1}{2}\alpha\chi(B_1^2 - B_2^2)\frac{\rho_1}{\rho_2}$$

where  $B_1$  and  $B_2$  refer to the field values at the ends of the sample,  $\alpha$  is the cross-sectional area of the specimen and  $\rho_1$  and  $\rho_2$  represent the packing density of the powder and the density of AlN respectively. This measurement procedure was continued at different temperatures, one of which will indicate the Curie temperature point when the force due to the magnetisation approaches zero.

### 6.5 Dielectric Measurement Techniques

The choice of the method depends principally on the range required and because the whole field of dielectric spectroscopy covers a wide range of frequency, from about 0.0001Hz to about 1000GHz, a large number of techniques are available. Measurement can either be made in the frequency or time domain. [6.5 - 6.8].

In frequency domain techniques, measurements are made at one frequency at a

time and a particular set of apparatus will only cover a certain frequency range. At low frequencies up to 40KHz bridge techniques are most appropriate; they can give precise measurements of both the real component of dielectric constant and the conductivity.

In the frequency range of 50Hz to 40KHz, the dielectric properties of materials are usually determined by measuring the capacitance and the conductance of a sample held between a pair of micrometer electrodes. The design of these bridges depends not only on the type and precision of measurement required, but also on the frequency range needed; for example, the Schering bridge is capable of measuring in the frequency range of 40KHz to about 1MHz.

The electrode systems are made so that the effect due to fringing fields at the edge of the specimen are reduced and the entire system is contained in a metal shielding box to eliminate undesirable effects of stray fields. Electrodes must be evaporated on the opposite polished surfaces of the specimens to ensure a good electrical contact over a well defined area between the specimen and the electrodes of the dielectric test jig; with many materials gold is used for this purpose. The usual arrangement for solids comprises flat, parallel plates of known area and separation between which is inserted the sample, in the form of a parallel sided disc of diameter slightly less than that of the electrodes. If the diameter of the sample extends beyond the electrodes then corrections for edge effects are necessary.

With the Universal Bridge used [6.8] the dielectric constant( $\epsilon$ ), and the loss tangent, ( $\tan\delta$ ), can be calculated from the following equations, Terman [6.9]

$$\epsilon' = \frac{C}{\epsilon_0} \quad 6.2$$

$$\tan\delta = \frac{G}{C\omega} = \frac{\epsilon''}{\epsilon'} \quad 6.3$$

where

$$\epsilon_0 = \frac{dA}{C_0}$$

and

C=Capacitance of the sample.

$C_0$  = Capacitance between electrodes (air)

G = Conductance of samples

$\omega$ = Angular frequency

d = thickness of samples

A = cross-sectional area of electrodes

and

$\epsilon_0 =$  permittivity of free space =  $8.85(Fm^{-1})$

## 6.6 The Samples Examined

The samples of aluminium nitride are listed below:-

a) AlN (B1)

This sample had been provided in powder form. It is dark grey in colour.

b) AlN (B2)

It is dark grey in colour and is a polycrystalline solid.

c) AlN (B3)

It is dark grey in colour and is a polycrystalline, sintered solid.

d) AlN (W1)

It is white in colour and is a polycrystalline, sintered solid.

For convenience in later sections specimen AlN (B1), AlN (B2) and AlN (B3) are referred to as "black" (having all come from the same manufacturer and having been

made by the same process) and AlN (W1) is referred to as "white" since it was white in colour and came from a different manufacturer.

## REFERENCES

- 6.1 *Varian V 4502 E.P.R. Spectrometer Manual.*
- 6.2 J. Crangle, "*The Magnetic Properties of Solids*". Edward Arnold, London (1977)
- 6.3 C.D. William, S.R. Hoon and J.S. Thorp *J. Mat. Sci. Lett.* 5,221 (1985).
- 6.4 J.S. Thorp, A.P. Johnson and C. Savage, *J. Material Sci.*, 4, 221 (1985).
- 6.5 J. Chamberlain and G.W. Chantry, "*High Frequency Dielectric Measurement*",
- 6.6 "*Dielectric Materials, Measurements and Application*", Science and Technology Press, London (1972).
- 6.7 "*Dielectric Material, Measurements and Application*". TEE Conference publication No.177 (1979).
- 6.8 "*Universal Bridge-Operating Instructions*", Wayne Kerr (B224) publication TP43.
- 6.10 F.E. Terman, "*Radio Engineers Handbook*". McGraw-Hill Company Limited, London, (1950).

## CHAPTER SEVEN

### EXPERIMENTAL RESULTS

#### 7.1 Structural Characterisation

##### 7.1.1 Diffraction, X-ray fluorescent Analysis and E.D.A.X.

The photographic X-ray diffraction patterns and diffractometer recording studies of AlN (W1) showed all the expected lines. These have been labelled with the corresponding Miller indices. In AlN (B1), AlN (B2) and AlN (B3), the same techniques were used and showed all the expected lines with extra lines which are not related to the pure AlN. The d-values have been tabulated and compared with the A.S.T.M. data in Table (7.1) (AlN is hexagonal with the parameters  $a = 3.220\text{\AA}$  and  $c = 4.980\text{\AA}$ , Ott [7.1].) This indicated that the AlN (B1), AlN (B2) and AlN (B3) samples have impurities. The X-ray fluorescent analysis confirmed that the samples AlN (B1, B2, B3) have appreciable iron contents with the concentrations of 2000 ppm, 2600 ppm and ppm 1400 ppm respectively with other impurities as listed in Table (7.2), whereas AlN (W1) proved to be almost pure.

In the S.E.M. and E.D.A.X. spectra, in all the samples, a large signal corresponding to Al was obtained as would be expected since it is a major constituent; the detector could not respond to low atomic number elements such as nitrogen. The SEM was

A.S.T.M. data*		AlN(W1)		AlN(B1)	
$dA^{\circ}$	hkl	$dA^{\circ}$	hkl	$dA^{\circ}$	hkl
2.70	100	2.693	100	2.685	100
2.49	002	2.483	002	2.475	100
2.372	101	2.366	101	2.354	101
1.829	102	1.827	102	1.826	102
1.557	110	1.552	110	1.553	110
1.414	103	1.413	103	1.411	103
1.348	200	1.342	200	1.343	200
1.320	112	1.319	112	1.318	112
1.301	201	1.301	201	1.298	201
-	-	-	-	1.2410	impurity
1.186	202	1.183	202	1.181	202
1.047	203	1.044	203	1.046	203
1.019	210	1.018	210	1.016	210
0.997	211	0.997	211	0.997	211
-	-	-	-	0.970	impurity
0.941	212	0.9414	212	0.9414	212
0.934	105	0.932	105	0.930	105
-	-	-	-	0.9128	impurity
-	-	-	-	0.8969	impurity
0.868	213	0.888	213	0.887	213

Table 7.1 X-ray diffractometer analysis of AlN samples

\*American Society for Testing Material

Impurity	AlN(W1)	AlN(B2)	AlN(B3)	AlN(B1)
Fe	30	2600	1400	2000
Si	-	210	40	600
Cr	200	79	107	-
Zn	-	600	-	140
Ti	600	330	200	-
Ca	300	-	-	-

**Table 7.2 X-ray fluorescent analysis of AlN samples (in ppm)**

operated in the stationary spot mode and so by moving the spot from one region to another, different parts of the sample could be examined. The spot size used was  $10\mu\text{m}$ . On one occasion, it was possible to detect the presence of iron in the specimen AlN (B2). The E.D.A.X. spectrum of the AlN (B2) is shown in Fig. (7.1) which consists of two distinct parts: a continuous background, which is due to the rapid deceleration of the electrons in the S.E.M. beam on striking the sample, and a number of sharp peaks superimposed on the continuous background. These peaks occur when an incident electron knocks an electron out of one of the inner shells of an atom in the samples. That leaves the atom in an excited high energy state and one of the outer electrons of the atom immediately fills the vacancy created in the inner shell. As it falls the outer electron emits energy of specific wavelength, in the X-ray region, and this highly monochromatic radiation gives rise to an E.D.A.X. peak. Since the energy of an emitted X-ray depends upon the spacings between the energy levels of the atom producing it, it will be the characteristic of that atom.

The E.D.A.X. spectrum obtained from the AlN (B2) sample displayed the  $AlK\alpha$ ,  $AuL\alpha$ ,  $AgL\alpha$ ,  $FeK\alpha$  and  $ZnK\alpha$  peaks. The  $AlK\alpha$  peak is obviously due to the aluminium atoms of the host lattice. No E.D.A.X. peak due to the nitrogen atoms was observed, because its peak has an energy outside the range covered by the X-ray energy analyser. The  $FeK\alpha$  peak is due to different X-ray transitions within the iron atoms. A  $ZnK\alpha$  peak, which shows the presence of Zn, is observed, and

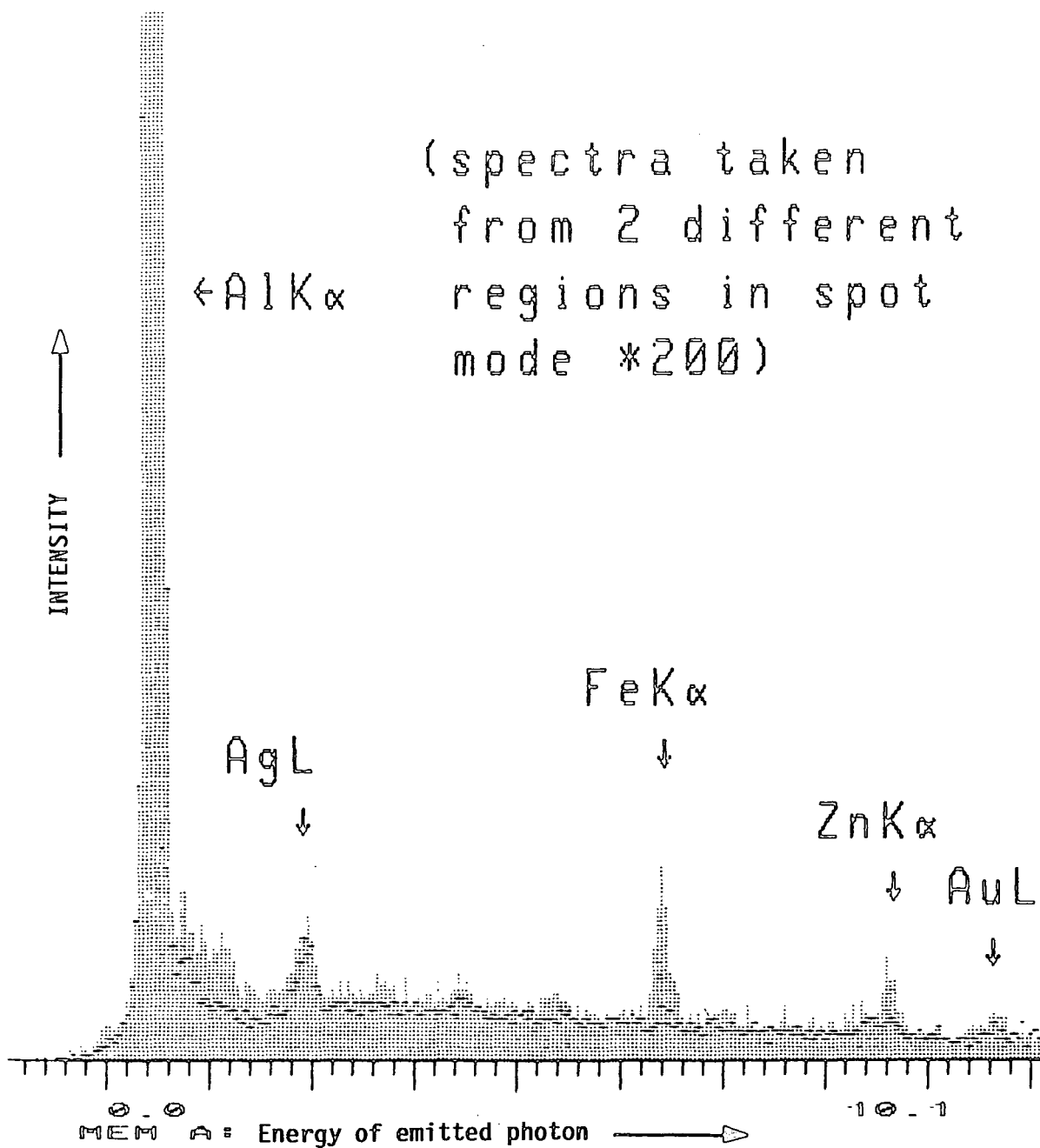


Fig. (7.1) E.D.A.X. spectrum of ALN (B2)

it is likely to be one of the sample impurities. It is also clear from Fig. (7.1) that, as expected, the  $AuL\alpha$  and  $AgL\alpha$  peaks are due to different X-ray transitions within the gold and silver atoms of the thin film put down to prevent charging of the samples during electron bombardment. Thus the E.D.A.X. spectra confirmed independently that two of the impurity elements observed by XRF, i.e. iron and zinc, were present.

The scanning experiments also gave clear evidence that the impurity is not uniformly distributed in the AlN matrix. That is to say the iron tends to be found in clusters rather than going into the lattice substitutionally. This implies that the effective impurity level in individual AlN grains is less than the level indicated by either the X-ray fluorescent or E.D.A.X. analysis.

### 7.1.2 Electron Spin Resonance Results

At room temperature, the ESR spectra for most of the AlN samples produced features; the notable exception was that the AlN (W1) sample gave nothing. An example is shown in Fig (7.2), which refers to AlN (B1). The g values and the linewidths for the AlN (B1, B2, and B3) samples are 1.989, 2.011 and 2.033 and 203.2mT, 296.87 mT and 210.9mT respectively. Because the features are very broad it is difficult to measure the centres and widths with the same high precision usually obtained in measurements on (narrow) paramagnetic lines. This led to an error in

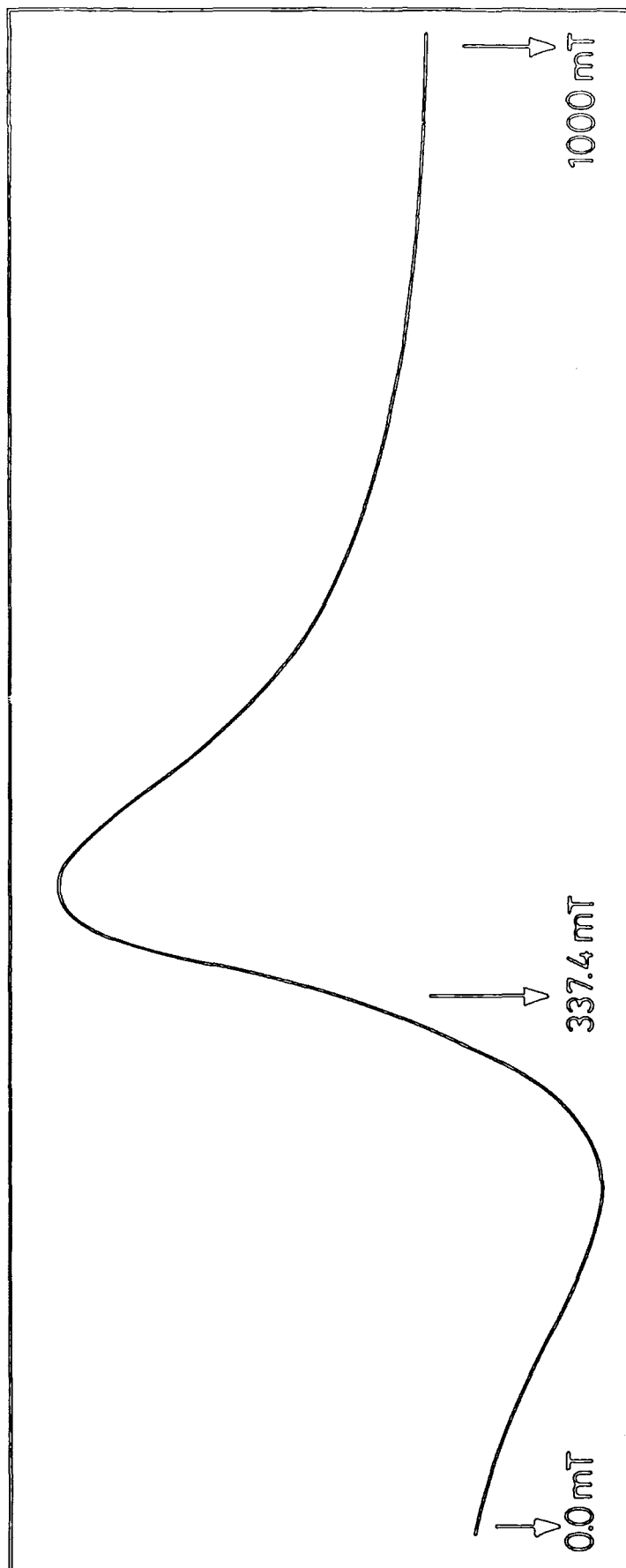


Fig. 7.2 E.S.R. spectra of AlN (B2), 9.50 GHz, 273K

g value of about  $\pm 0.025$ . Hence the three g values quoted are to be regarded as the same, the mean g value being  $g = 2.011$ . The E.S.R. spectra of AlN (B1, B2, and B3) samples were also recorded at temperatures between 20K and 273K, so as to evaluate the temperature dependence and the variation of peak to peak linewidth. The results show that for AlN (B1), the value of  $\Delta H_{pp}$  is approximately constant at 198mT between about 200 — 113K, but that it increases above 220K and below 114K. For AlN (B2), the value of  $\Delta H_{PP}$  is approximately constant between 230K — 150K with the value 285.15mT, but that it increases above 230K and below 150K. In AlN (B3), between 273K — 200K the value of  $\Delta H_{PP}$  is approximately 203.1mT and it increases below 200K. The linewidth-temperature variations for the AlN samples are shown in Fig.(7.3).

### 7.1.3 Curie Temperature Determination

As a test of the Gouy balance technique, the Curie temperature of nickel powder was measured. This experiment produced the value ( $366 \pm 10^0C$ ) which was obtained from a graph of magnetic force against temperature, Fig (7.4). This result agreed well with the value ( $355^0C$ ) quoted from the literature [7.2] and showed that the technique was valid. For AlN (B1), the Curie temperature was found in a similar manner and was estimated as ( $780 \pm 10^0C$ ); the data is shown in Fig (7.5). This measured Curie temperature is the same as the value for Fe which has been reported in the literature to be ( $770^0C$ ) [7.3].

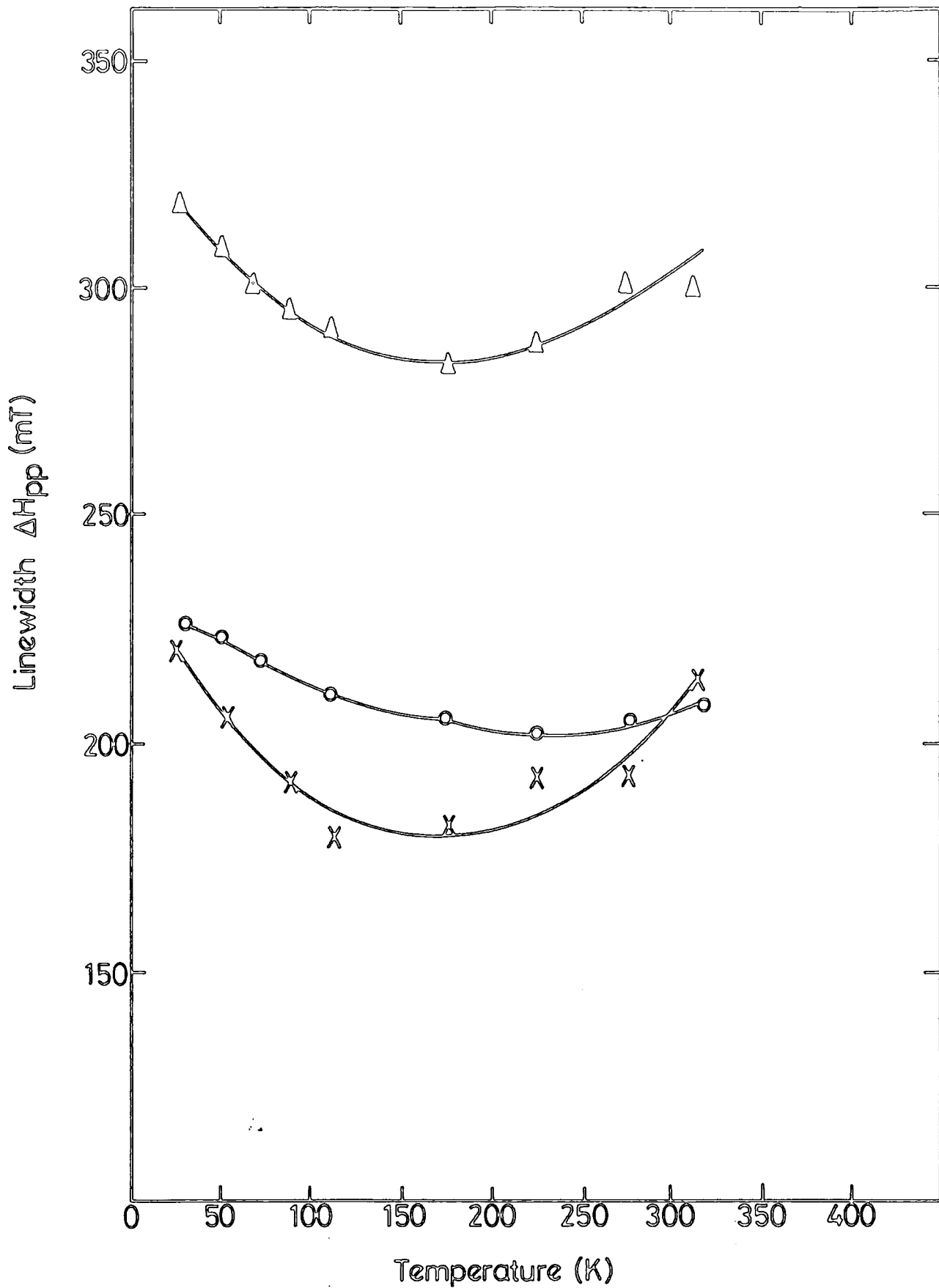


Fig. (7.3) Linewidth - Temperature variation for ALN samples

- $\Delta$  ALN (B2)
- $\circ$  ALN (B3)
- $\times$  ALN (B1)

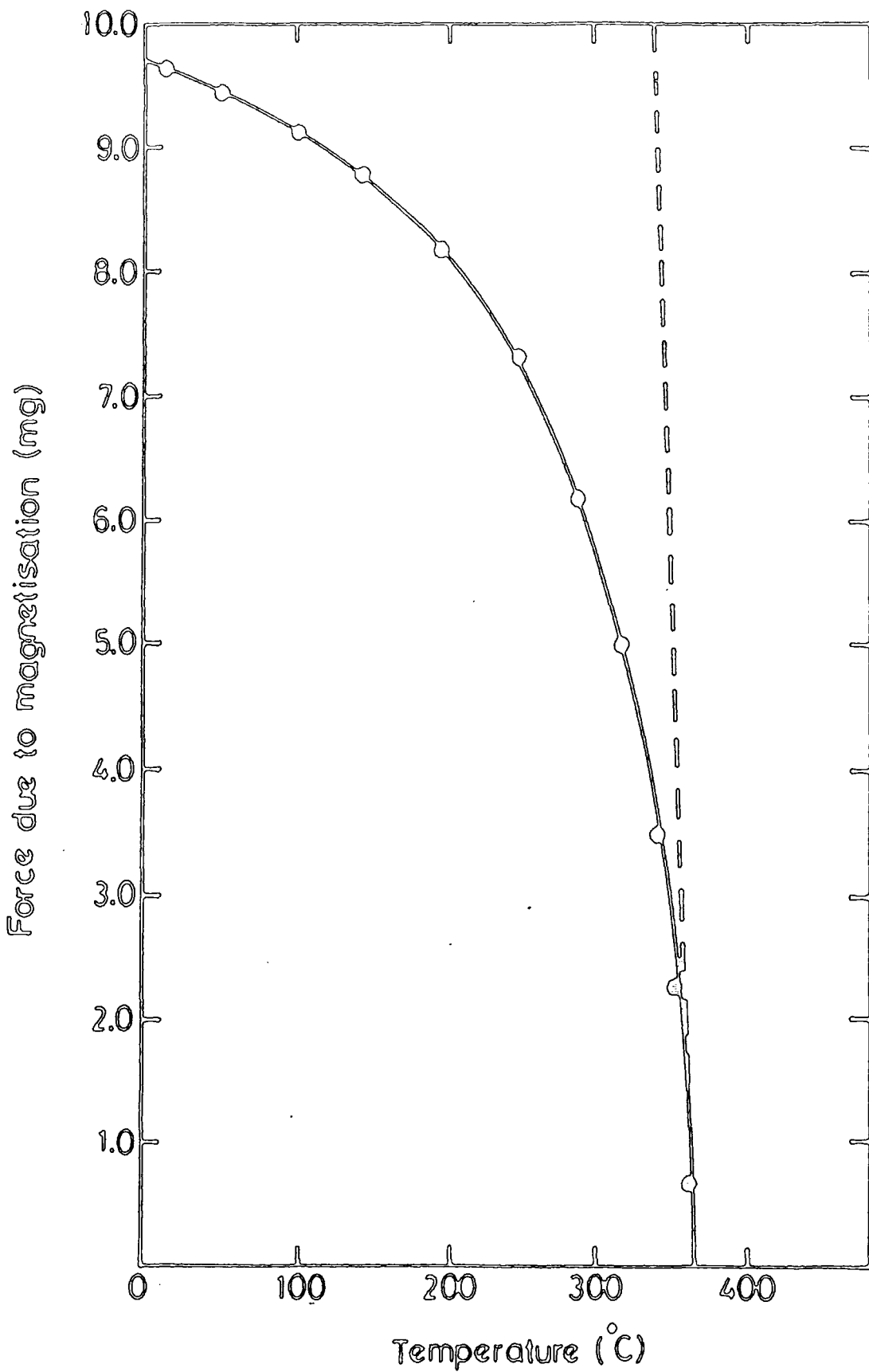


Fig. (7.4) Force-temperature variation for nickel powder

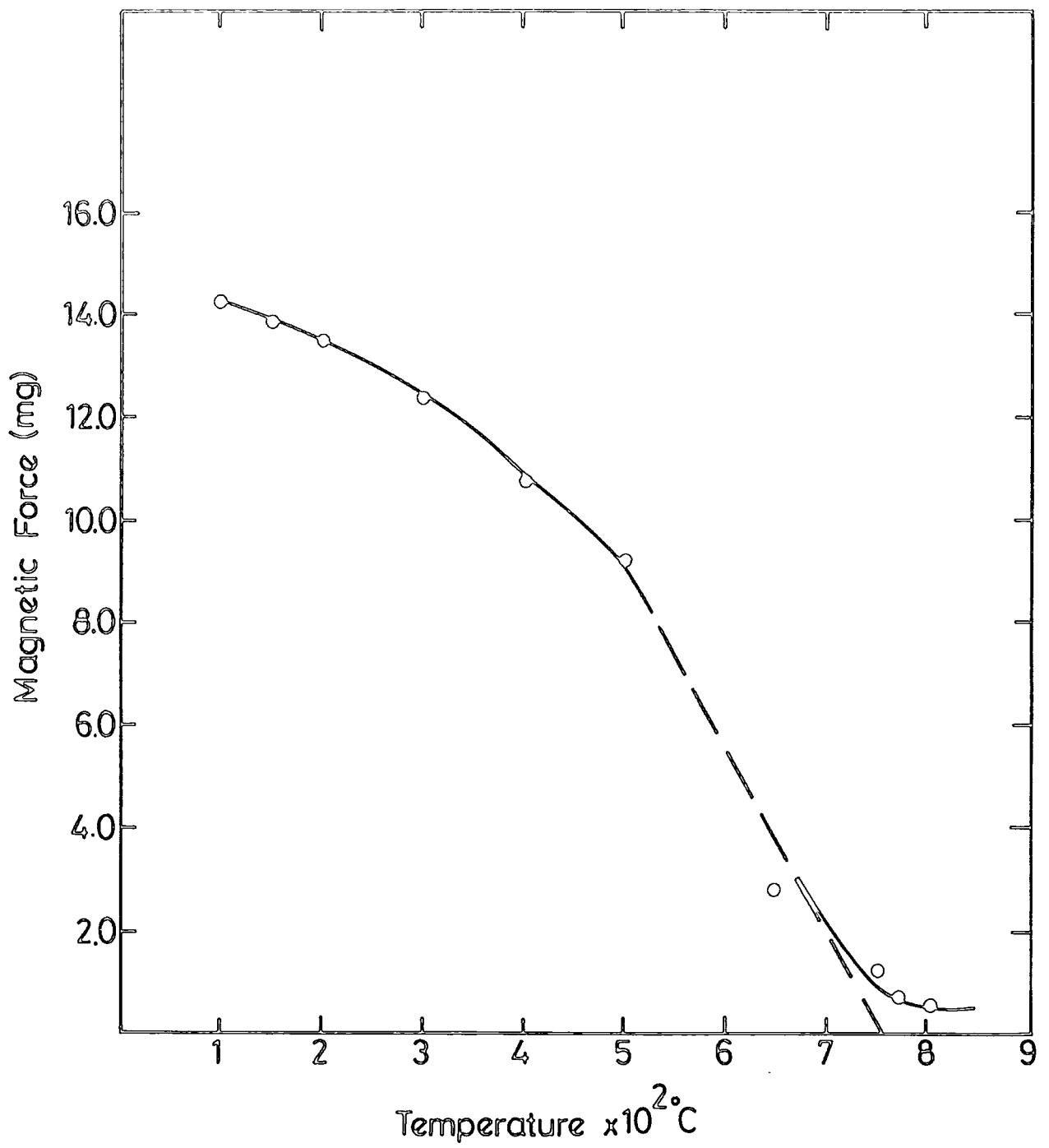


Fig. (7.5) Force-temperature variation for AlN (B1) Sample.

Susceptibility measurements were only possible on one sample because insufficient supplies of the others were available. In addition to the measurement of Curie temperature, which, in order to obtain maximum sensitivity, was made using a fixed (maximum) magnetic field, the dependence of the room temperature magnetisation on field was also examined. The data for AlN (B1) is given in Fig (7.6) which shows the variation of magnetic force with the square of the magnetic field. It can be seen that the plot is distinctly non-linear. However, assuming paramagnetic behaviour in the low field region ( $10^4 B_1^2 < 4$ ), the susceptibility would be  $\chi = 21.58JT^{-2}$ . It is certainly the case that the sample is not diamagnetic; on the contrary the sample has quite a large positive susceptibility.

## 7.2 Dielectric Properties

The capacitance and the conductance of AlN (B2) and AlN (W1), which were both available in thin solid disc form, were measured directly and therefore the permittivities of both samples were calculated using equation (6.2). In these results, the least reading error of the conductance due to the instrument was  $\pm 0.01$  nmhos arising from both the inaccuracies in the standard arms, and the parasitic components of the bridge circuit and stray capacitance. The errors were estimated to be about 5%. Fig (7.7) shows the dielectric properties ( $\epsilon'$ ) of both AlN (B2) and AlN (W1) samples as a function of frequency from 500Hz to 20Hz. The values of ( $\epsilon'$ ) for AlN (B2) and AlN (W1) are 9.3 and 7.2 respectively.

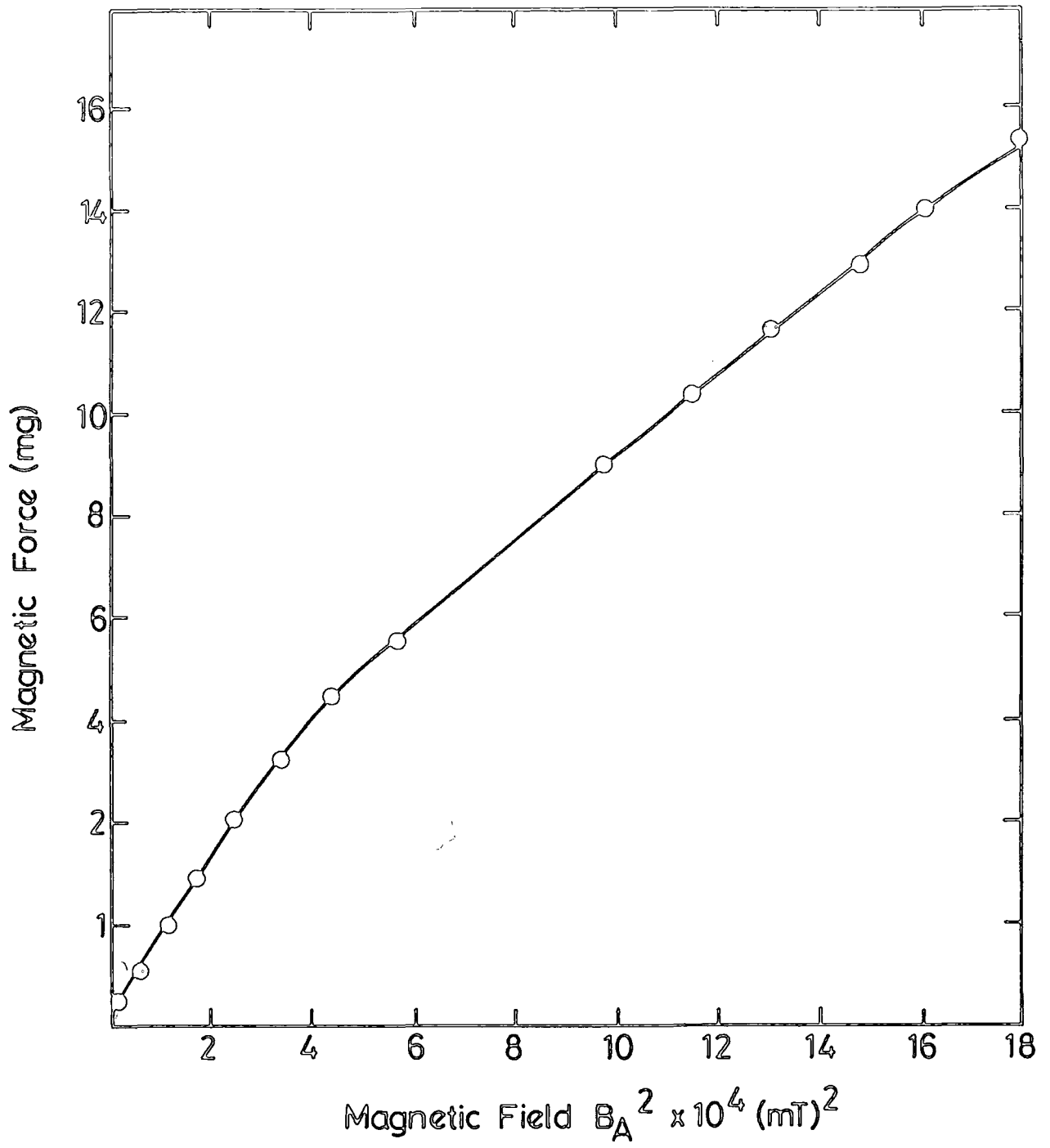


Fig. (7.6) Force-(Magnetic Field)<sup>2</sup> variation for AlW (B1)

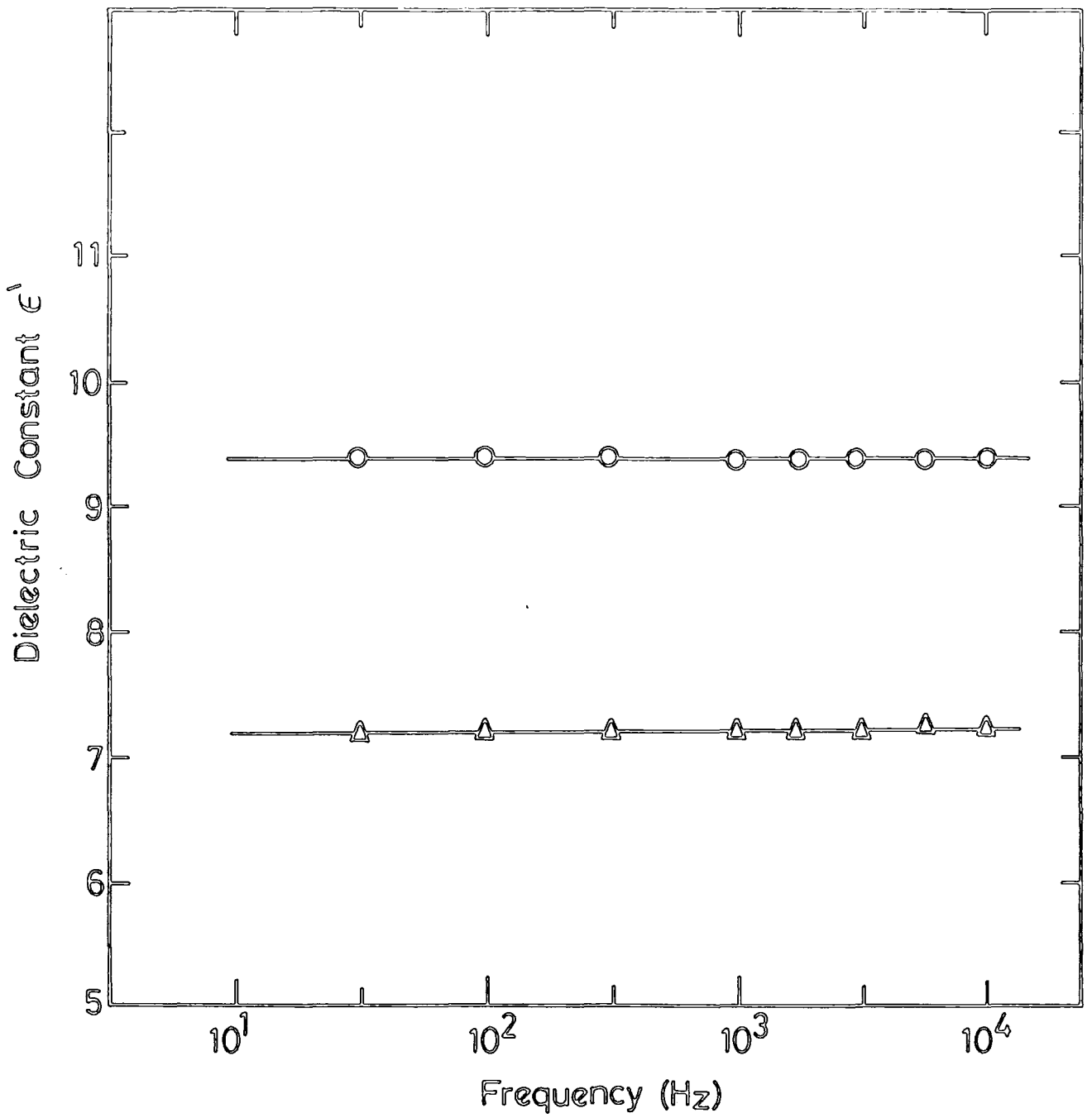


Fig (7.7) Frequency Dependence Dielectric Constant  $\epsilon'$ , 293K

$\triangle$  - ATN (W1) - White

$\circ$  - ATN (B2) - Black

## REFERENCES

- 7.1 R.M.Bozorth, "*Ferromagnetism*" D.Van Nostrand Co.Inc,
- 7.1 Ott, *Z. Physik*.22, 201 (1924)
- 7.2 R.C.Weast, "*Handbook of Chemistry and physics*" CRS Press 57th .Inc,7.2 R.C.  
Weast, "*Handbook of Chemistry and Physics*"CRC Press 57th edition, E120 (1976-  
1977).
- 7.3 R.M.Bozorth, "*Ferromagnetism*" D.Van Nostrand Co.Inc, London(1951)

## CHAPTER EIGHT

### DISCUSSION AND CONCLUSIONS

#### 8.1 Features Revealed by X-Ray and E.D.A.X. Studies.

The photographic X-ray diffraction patterns and the spectra obtained with the X-ray diffractometer both show that at least one impurity is present as a separate phase whose exact composition is uncertain because of the small number of impurity lines observed. The X-ray fluorescent (XRF) spectra showed the definite presence of additional elements, namely iron (Fe), titanium (Ti), silicon (Si) and cobalt (Co). It gave quantitative estimates of the impurity levels which ranged from as much as 2200 ppm Fe to around 15 ppm Co. It confirmed that the specimen AlN (W1) had a much lower overall impurity content than the other samples. It should be noted that XRF does not indicate the structure of a phase, but only the elemental composition of the material examined. With the XRF equipment available, detection at Al was possible (this was seen as the predominant peak) but not of nitrogen or oxygen.

The main result from the E.D.A.X. experiment on AlN (B2) (a black sample) is that the majority of the impurities are concentrated in localised regions and not uniformly distributed throughout the matrix. On the other hand, examination of the white variety AlN (W1) showed no evidence of impurities and this confirmed the XRF analysis results. Nitrogen is of course a major constituent and the E.D.A.X.

results do not exclude the possibility that some oxygen remains in the nitride; the presence of some residual oxygen would not be surprising in view of the method of preparation used. Because of the limitation of the detector, the E.D.A.X. equipment can not detect either nitrogen or oxygen.

## 8.2 Features Revealed by Magnetic Measurements.

The room temperature E.S.R. studies of all the black[AlN (B1), AlN (B2) and AlN (B3)]samples gave a single feature having a broad linewidth between 200 mT to 300 mT. From general experience of paramagnetic spectra, it is unlikely to be due to a substitutional paramagnetic dopant in the AlN. It is more likely to be of ferromagnetic or ferrimagnetic origin, because the  $g$  values of these three samples were close to  $g = 2.0$  and because the linewidth values  $\Delta H$  were very large. One possibility is that the E.S.R. spectra are due to elemental iron i.e. This could give a room temperature FMR signal near  $g=2.0$  and would be compatible with the X-ray analysis. A second possibility is that there is Fe present not as an element but as a compound, in particular a ferrimagnetic oxide of iron, possibly  $Fe_3O_4$ . This would also be compatible with both the XRF and E.D.A.X. data, (since neither is able to detect oxygen). In order to provide direct information the E.S.R. spectrum of iron oxide,  $Fe_3O_4$  was also recorded under conditions closely similar to those which had been used for aluminium nitride and the  $g$  value and linewidths were measured (see Table 8.1). There is also a third possibility namely that both Fe and  $Fe_3O_4$  are

Elements and Compounds	Linewidth (mT)	g Factor	Reference
Fe	16.0	2.004	8.1
			8.2
Ni	13.0	2.22	8.3
			8.4
Co	15.5	2.021	8.3
$Fe_3O_4$	250.0	2.016	This work (Part II)
<i>Black AlN(B<sub>2</sub>)</i>	296	2.011	This work (Part II)
Iron doped alumina, $Fe^{3+}/Al_2O_3$ powder (1000ppm)	2.17	2.002	This work (Part I)

Table 8.1 Room temperature ferromagnetic resonance data for some elements and oxides compared with observed data for black AlN and for substitutional (paramagnetic) iron

present together. In reviewing the remaining analytical data all three possibilities must be considered in order to see, if possible, which is the more probable.

The data for F.M.R. resonance given in Table (8.1) suggests that none of the listed elements has a linewidth at all comparable with that observed. Of the elements only Fe has a  $g$  value ( $g = 2.09$ ) fairly close to that observed for black AlN ( $g = 2.00$ ). For iron oxide however, the linewidth, (250 mT) is quite comparable with that found in the black AlN and its  $g$  value is also close to 2.011. For substitutional iron, i.e.  $Fe^{3+}/AlN$ , the ESR linewidth would be expected to be of the same order as those found in iron doped alumina ( $Fe^{3+}/Al_2O_3$ ) which are only about 3 mT for an iron concentration of about 1000 ppm, which represents the maximum level of iron which could be accommodated in the lattice.

The temperature variation of linewidth for the three black AlN samples showed a maximum near 20K. The linewidth increases at lower temperatures giving a ratio of  $\Delta H_{20}/\Delta H_{300}$  of about 1:3. This is comparable though rather smaller than the changes reported by Bhagat [8.5] who gave a ratio of about 1:8 times for iron. However, the general form of the linewidth versus temperature behaviour for the AlN (black) samples is very similar to that for Fe. At this stage the species responsible for the observed impurity line cannot definitely be ascribed to Fe, although some of the data would fit this interpretation.

As regards the susceptibility measurements, it should be noted that the pure AlN should be diamagnetic, Weast [8.6]. The results of the AlN (B1) sample proved conclusively that the susceptibility is positive rather than negative and when the magnetic force (F) was measured as a function of  $B^2$ , the variation was not linear. This shows that the black AlN (B1) must contain some ferromagnetic or ferrimagnetic impurity or impurities. A true paramagnetic would give a linear plot of magnetic force (F) against  $B^2$ , Williams et al [8.7]. This non-linearity of the magnetic force (F) and  $B^2$  plot would be expected for a ferrite, i.e. for  $Fe_3O_4$  as well as for elemental iron Fe. The Curie temperature measurement gave  $\theta_c = 780 \pm 5^\circ C$ . Some collected Curie temperature data for elements and compounds is given in Table (8.2). The value for iron, for which the Curie temperature is  $770^\circ C$  is in very close agreement with the observed value. However, for the ferrite  $Fe_3O_4$ , the Curie temperature is  $575^\circ C$  which is much lower than the observed value. There is no evidence in the Curie plot for a discontinuity at  $575^\circ C$ ; rather the monotonic variation of the susceptibility with temperature over the intermediate temperature range suggested that a single magnetic phase was involved. It is however, interesting to point out that above  $650^\circ C$  the slope of the magnetic force-temperature plot does not continue to increase as rapidly as did the corresponding plot for pure nickel near its Curie temperature. This feature can be coupled with the fact that the magnetisation did not fall completely to zero at  $770^\circ C$ . Although there is insufficient data for precise conclusions to be drawn it is perhaps indicative that there are several

Elements and Compounds	Curie Points	Compounds	Curie Points
Elements			
Fe	770	MnBi	350
Co	1130	$Mn_4B$	470
Ni	358	MnP	25
Gd	16	MnSb	320
Dy	-168	$Mn_2Sb$	275
		$Mn_3Sb_2$	315
Compounds			
	-	$Mn_2Sn$	0
$Fe_3Al$	500	$Mn_4Sn$	150
$FeBe_2$	520	$AgF_2$	-110
$FeBe_5$	$< 0$	$CrS_x$	30;100
$Fe_2B$	739	CrTe	100
$Fe_3C$	215	$Fe_3O_2S$	580
$Fe_2Ce$	116	$AlFe_2O_4$	339
$Fe_4N$	488	$BaFe_2O_4$	445
$Fe_3P$	420	$BeFe_2O_4$	190
FeS	320	$CdFe_2O_4$	250
$FeS_2$	$> 0$	$CoFe_2O_4$	520
$Fe_3O_4$	575	$CuFe_2O_4$	490
$Fe_2O_4$	620	$MgFe_2O_4$	315
$Fe_2P$	420	$MnFe_2O_4$	510
$Fe_4N$	485	$NiFe_2O_4$	590
$Fe_3Si_2$	90	$PbFe_2O_4$	435
$Co_2B$	510	$SnFe_2O_4$	325
$CoS_2$	-180	$SrFe_2O_4$	450
CoZn	125	$La_2O_3Fe_2O_2$	465
$Co_4Zn$	490	$Pr_2O_3Fe_2O_3$	425
$Ni_2Mg$	235	$Nd_2O_3Fe_2O_3$	300
$Ni_3Mn$	470	$Sm_2O_3Fe_2O_3$	300
MnAs	45	$Er_2O_3Fe_2O_3$	255
MnB	260	$Y_2O_3Fe_2O_3$	275

Table 8.2: Curie points, in  $^{\circ}C$ , of elements and compounds (or ordered structures) was reported from various sources [8.8 - 8.11]

high  $\theta_c$  phases involved which have Curie temperatures higher than that of iron.

### 8.3 Features Revealed by Dielectric Measurements.

The data shown in Fig.(7.6) reveals two important features. Firstly, in both the white and black varieties of aluminium nitride the permittivity was virtually independent of frequency. Secondly, the permittivity of the black material was substantially higher ( $\epsilon' = 9.3$ ) than that of the white form, ( $\epsilon' = 7.2$ ) . Considering first the white specimen, it is known, from the results of all the analytical and appraisal techniques described above, that there are no impurities present (above trace level). Consequently the behaviour of Fig. (7.6) for AlN (W1) can be taken as typical for pure aluminium nitride. It suggests that the material is a hopping conductor, Jon-scher [8.12]. If this were the case, and to prove this corresponding measurements of dielectric loss versus frequency would need to be made, the following relations would apply

$$\epsilon' \propto \omega^{n-1} \quad 8.1$$

$$\epsilon'' \propto \omega^{n-1} \quad 8.2$$

in which the exponent  $n$  is a number whose value is usually just less than unity and  $\omega$  is the angular frequency. Fitting the data from Fig. (7.6) to equation (8.1) gives the value  $n = 0.9$ . The frequency independent permittivity coupled with the near unity value of the exponent  $n$  is very similar to results which have been reported for aluminium oxide,  $Al_2O_3$ , [8.13] and [8.14], magnesium oxide MgO [8.15], a variety of oxy-nitride glasses [8.16], and silicon nitride, [8.17]. The comparison is made in more detail in Table(8.3). In this situation one is dealing with a composite dielectric. In the simplest case it can be assumed that there are only two phases present, the pure aluminium nitride and the impurity phase. (The possibility of the impurity simply acting as a dopant in the AlN lattice has been excluded by the direct X.R.D. evidence for separate phases.) There are many "mixing rule" formulae which give expressions for the resultant permittivity of a composite dielectric, Van Beek [8.18], and Hale [8.19]. In order, however, to obtain increase in resultant permittivity due to the addition of a relatively small volume fraction of a second phase, the permittivity of the second phase must be much larger than that of the matrix. It is suggested here from the combination of X-ray and magnetic studies that the impurity (or impurities) are iron and/or iron oxide. The permittivity of elemental iron (Fe) is about  $10^5$ , so a small amount could easily give the observed rise in overall permittivity.

From the point of view of its possible use as a V.L.S.I. substrate material it seems

Material	Permittivity	Value	Reference
Aluminium nitride, AlN			
Polycrystalline, white	7.2	0.9	Present Work
Polycrystalline, black	9.3	0.9	Part II
Aluminium Oxide, $Al_2O_3$			
Single crystal, (11c)	9.4	frequency independent	8.14
Polycrystalline ceramic substrate	8.0	0.98	8.14
Magnesium oxide, MgO			
Pure and doped single crystals		0.98	8.15
Oxy-nitride glasses (Zero nitrogen content)			
Mg - Al - Si - O - N	6.9	0.99	8.16
Y - Al - Si - O - N	8.3	0.99	8.16
Ca - Al - Si - O - N	8.3	0.99	8.16
Nd - Al - Si - O - N	10.2	0.99	8.16
Silicon nitride, $Si_3N_4$	6.0	0.98	8.17
Reaction bonded, polycrystalline			

Table 8.3 Comparative dielectric data for some hopping type conductivity ceramics and glasses

that the pure grade (white) AlN would be very competitive with the more generally used  $Al_2O_3$  while retaining its advantage as a higher thermal conductivity material. It has been shown also that the presence of iron-based impurities degrade the electrical performance. The techniques employed could be used for quality control during manufacture to monitor both the raw materials and the inclusion of impurities during processing and fabrication; in this sense the combination of X-ray, magnetic and microscopic techniques represents a powerful appraisal facility which could be of wide importance to other materials.

## REFERENCES

- 8.1 S. Bhagat, L.L. Hirst and J.R. Anderson, *J. Appl. Phys.* 37, 1 (1966).
- 8.2 B. Bleaney and K.W.H. Stevens, *Repts. progr. in Phys.* 18, 304 (1955).
- 8.3 S.M. Bhagat and P. Lublitz, *Phys. Rev. B.* 10, 1, 179 (1974).
- 8.4 E.W. Pugh and B.E. Argyle. *J. Appl. Phys. Suppl.* 33, 1178 (1962).
- 8.5 S.M. Bhagat, J.R. Anderson and Ning Wu, *Phys. Rev.* 155, 2, 510 (1967).
- 8.6 R.C. Weast "*Handbook of Chemistry and Physics*", CRC Press 57th edition, E120 (1976-1977).
- 8.7 C.D.H. Williams, S.R. Hoon and J.S. Thorp, *J. Mater. Sci. lett.*, 5, 832 (1986).
- 8.38 R.M. Bozorth, "*Ferromagnetism*", D. Van Nostrand Co. Inc., London (1951).
- 8.9 R. Forrer, *J. Phys. radium*, 4, 427 (1933).
- 8.10 M. Fallot, *Ann. Physique*, 6, 305 (1936).
- 8.11 V. Marian, *Ann. Physique*, 7, 459 (1937).
- 8.12 A.K. Jonscher, *Nature*, 267, 673 (1977).

- 8.13 S. Govinda and K.Y. Rao, *Phys. Stat. Sol. A* 27,(1975), 639.
- 8.14 M. Akhtaruzzaman, Univeristy of Durham, private communication.
- 8.15 J.S. Thorp and E.N. Rad, *Jour. Mater. Sci.* 16, (1981), 255.
- 8.16 S.V.J. Kenmuir, J.S. Thorp and B.L.J. Kalesza, *Jour. Mater. Sci.* 18, (1983),  
1725.
- 8.17 T.G. Bushell, Ph.D 82, Thesis, University of Durham, 1983.
- 8.18 L.K.H. Van Beek, *Progress in Dielectics*, 7, 71, (1967).
- 8.19 D.K. Hale, *J. Mater. Sci.* 11, 2105 (1976).

